Extreme convective precipitation events in a changing climate

Lochbihler, K.U.

Important note
To cite this publication, please use the final published version (if applicable).
Please check the document version above.

EXTREME CONVECTIVE PRECIPITATION EVENTS IN A CHANGING CLIMATE

KAI LOCHBIHLER

EXTREME CONVECTIVE PRECIPITATION EVENTS IN A CHANGING CLIMATE

Kai Uwe LOCHBIHLER

EXTREME CONVECTIVE PRECIPITATION EVENTS IN A CHANGING CLIMATE

Dissertation

for the purpose of obtaining the degree of doctor
at Delft University of Technology
by the authority of the Rector Magnificus, prof. dr. ir. T.H.J.J. van der Hagen,
chair of the Board for Doctorates
to be defended publicly on
Monday 8, November 2021 at 15:00 o'clock

by

Kai Uwe LOCHBIHLER

Master of Science in Climate and Environment Sciences,
University of Augsburg, Germany,
born in Kempten im Allgäu, Germany.

This dissertation has been approved by the promotors.

Composition of the doctoral committee:

Rector Magnificus,	chairperson
Prof. dr. A.P. Siebesma,	Delft University of Technology, promotor
Dr. G. Lenderink,	Royal Netherlands Meteorological Institute (KNMI), copromotor

Independent members:

Prof. dr. ir. R. Uijlenhoet,	Delft University of Technology
Prof. dr. C. Schär,	ETH Zürich, Switzerland
Prof. dr. ir. H.W.J. Russchenberg,	Delft University of Technology
Dr. J.O.M. Härter,	University of Copenhagen, Denmark

Other members:

Dr. S. Böing,	University of Leeds, UK

There should be sunshine after rain
These things have always been the same
So why worry now?

Dire Straits - Why worry

CONTENTS

SUMMARY

As I am writing this, parts of Central Europe are plagued by a series of intense rainfall events that, in less than two days, turn rivers into powerful streams, cause flooding, damage infrastructure and property, and harm people. The number of such extreme events, which are associated with high economic losses and casualties, has been increasing for decades. How is this happening? And, what is the relation between extreme convective precipitation events and increasing temperatures, such as which we are currently experiencing due to climate change?

To tackle these questions, consider the following simplified version of a convective rain event. We imagine a column of air, a part of the atmosphere with a cloud inside of it. Near the surface, air streams into the column where it starts rising vertically. While gaining height, the air cools, until at a certain level the contained water vapor will condensate in the form of small cloud droplets. From this level, the cloud base, the air mass continues ascending while the amount of condensed water keeps increasing, so that the cloud droplets grow in size. Finally, when they grow sufficiently large, precipitation will set in, and, in the most extreme case, all the cloud water will reach the ground as rain. Following this conceptual model, one way to increase the amount of precipitation is to increase the moisture content of the air that enters the cloud.

In this case, the Clausius-Clapeyron (CC) relation plays an important role. It describes the water holding capacity of air with respect to its temperature. If relative humidity remains climatologically unchanged with global warming the amount of moisture contained in the atmosphere will increase at a rate of about 7 % per degree warming. Indeed, it was found that, globally, extremes of daily precipitation amounts are bound by this rate of change. However, local precipitation extremes on hourly and subhourly time scales were found to exhibit higher rates than dictated by the Clausius-Clapeyron relation. This phenomenon is commonly called super CC-scaling. To explain this behavior, a common theory suggests that if the amount of moisture increases the amount of energy released through condensation in a convective updraft will intensify. This will lead to stronger updrafts and ultimately to a stronger moisture convergence into the cloud column.

Despite the fact that station observations of short-term precipitation extremes can display super CC-scaling, the exact process behind the phenomenon is still unknown. Moreover, it remains unclear how the characteristics of individual convective events, such as the size and precipitation intensity, will respond to a warmer and moister atmosphere. In this thesis we use rain radar data with a full coverage of the Netherlands and isolate individual convective events with a tracking algorithm. We then investigate the statistics of size and intensity of rain events at the time of their peak intensity. The results from this analysis show that the spatial extent and the intensity of extreme convective events are tightly coupled. Both characteristics jointly increase, meaning that stronger rain events are generally larger in size. Under warmer and moister conditions, the size

of events rapidly increases at dew point temperatures above approximately 15 °C. Super CC-scaling is found when including all events in the analysis. However, the largest events are crucial to sustain super CC-scaling at higher temperatures. Enhanced precipitation rates appear over the whole area of the event.

To further study the dynamics of convective precipitation extremes in a controlled setting, we make use of a large eddy simulation (LES) model. A LES model can run at a high enough resolution to resolve processes which are necessary for the formation of small-scale thunderstorms. It is further possible to take time-dependent influences on the simulation domain into account, such as a large-scale wind profile and convergence. Here, we apply an idealized yet realistically forced case setup that is representative for heavy summertime precipitation in the Netherlands. We simulate the base case, as well as a number of experiments with changed temperature and moisture following the assumption of constant relative humidity. To study the characteristics of rain events we cluster continuous areas with precipitation to rain cells. Based on that, we can confirm the relationship between size and intensity of rain cells. In warmer and moister simulations, rain cells grow larger and become more intense over their whole area. The number of large events increases at the cost of smaller events. These results draw a consistent picture together with the previously mentioned observation-based study.

So far, we have considered precipitation events as rather isolated entities from each other. However, another factor that can influence the magnitude of rain events is the process of convective organization. For instance, compare an isolated convective cell to a mesoscale convective system that can be seen as a cluster of multiple thunderstorms. The latter is a more organized form of a convective precipitation event. In this case, the horizontal extent of the two types differs by around a factor of ten. Local dynamics induced by cold pools play a key role in the formation of more organized events. Cold pools originate from evaporation of rain drops in the atmosphere. This causes a cooling of air masses which intensifies the downdraft strength due to their relatively higher density. At the surface, the downdraft will spread out horizontally over a distance of tens of kilometers. This effect is tangible, for instance, when observing a nearby thunderstorm. The relatively dense moving air mass vertically dislocates the surrounding air and can trigger the formation of new convective clouds. The effect is even stronger when two or more cold pools collide. Also, cold pools transport and accumulate moisture into confined regions that are preferred locations of new convective events.

Besides the clear effect of cold pools on the formation and organization of convective rainfall events, little is is know about how these processes change in a warmer climate. Also, how cold pool dynamics respond under these conditions and how this relates to precipitation characteristics is an open question. To study this, we use a similar LES setup as in the above mentioned case. We also repeat the experiments with a warmer and moister setting. Similar to the previously mentioned method of rain cell clustering, we apply the same technique to low-level temperature and moisture fields to identify cold pools and relatively moist areas, so-called moist patches.

We see that increased size and intensity of rain cells under warmer and moister conditions have a strong correlation with the size and spreading speed of cold pools. This, in turn, relates well to the size and amount of moisture contained in moist patches. These correlations suggest a feedback loop in which cold pools that originate from initially

rather randomly distributed and weak rain events, cause a higher variability in the low-level moisture field, and trigger events that are more organized and have higher intensities. Thus, cold pool dynamics can enhance the local moisture availability and supply to newly forming rain events without additional large-scale convergence. From a separate group of experiments we deduct that enhanced large-scale convergence alone only affects the rain cell area but not the intensity.

But, do these findings hold in a more realistic scenario of climatic warming? For instance, it is known that relative humidity will decrease with warming in many regions over land. Furthermore, it is expected that the atmosphere will not get warmer uniformly with height. Due to convection, the temperature profile will follow a change close to a moist adiabatic lapse rate, leading to a more stable atmosphere. Our experiment design applies these principles and separate simulation groups are created for both situations. We find that a reduced relative humidity with warming generally further amplifies precipitation events, cold pool dynamics and moist patches. This highlights relative humidity, besides precipitation intensity, as another factor that controls the evaporation rate of rain drops and ultimately the strength of cold pools. Despite of a dampening effect, more stable conditions with warming still lead to more intense and larger rainfall events that are associated with stronger cold pool dynamics and moist patches.

Finally, the results presented in this thesis show that extreme convective precipitation events exhibit a strong response to climatic warming and highlight the importance of small-scale dynamics in this context. This must be taken into account for better predictions of future extremes.

SAMENVATTING

Terwijl ik dit schrijf, worden delen van Centraal-Europa geteisterd door een reeks hevige regenbuien die in minder dan twee dagen rivieren in krachtige stromen hebben veranderd, overstromingen veroorzaakt, vele dodelijke slachtoffers geëist en infrastructuur en eigendommen beschadigd. De frequentie van extreme buien, die gepaard gaan met veel economische schade en slachtoffers, is de afgelopen decennia sterk toegenomen. Hoe kan dit en wat is de mogelijke relatie tussen de toename van deze extreme convectieve buien en opwarming ten gevolge van klimaatverandering?

Om deze vragen te beantwoorden, beschouw de volgende vereenvoudigde versie van een convectieve bui. Stel je een verticale luchtkolom voor met een deel van de atmosfeer en een wolk erin. Dicht bij het landoppervlak stroomt lucht in de kolom waarna het verticaal begint te stijgen. Tijdens het stijgen koelt de lucht af, en raakt de waterdamp uiteindelijk oververzadigd zodat er kleine wolkdruppeltjes worden gevormd door condensatie. Vanaf deze hoogte, de wolkenbasis, blijft de luchtmassa stijgen terwijl de hoeveelheid gecondenseerd water blijft toenemen, zodat de wolkendruppels groter worden. Ten slotte, wanneer ze groot genoeg zijn, zal er neerslag vallen, maar slechts in het meest extreme geval zal al het wolkenwater de grond bereiken als regen. Volgens dit conceptuele model is het verhogen van het vochtgehalte van de lucht die de wolk binnenkomt een manier om de hoeveelheid neerslag te vergroten.

Hierbij speelt de Clausius-Clapeyron (CC) vergelijking een belangrijke rol. Deze laat zien dat het waterdamp houdend vermogen van lucht exponentieel toeneemt met de temperatuur. Dit heeft als gevolg dat voor een gelijkblijvende relatieve vochtigheid, de hoeveelheid vocht in de vorm van waterdamp in de atmosfeer toeneemt met ongeveer 7 % per graad opwarming. Op globale schaal is inderdaad aangetoond dat extremen in dagelijkse neerslaghoeveelheden gebonden zijn aan deze veranderingssnelheid. Lokale uurlijkse en 10 minuten neerslagextremen bleken echter grotere toenames te vertonen dan de verwachte 7 % per graad opwarming volgens de CC vergelijking. Dit fenomeen wordt ook wel "super CC-gedrag" genoemd. De gangbare theoretische verklaring hiervoor is dat er niet alleen 7 % meer water condenseert maar dat er hierdoor ook meer energie vrijkomt door condensatie waardoor de convectieve opwaartse luchtstroom in wolken ook toeneemt. Dit zal tot sterkere opwaartse stromingen en uiteindelijk tot een sterkere vochtconvergentie in de wolkenkolom leiden.

Ondanks dat stationswaarnemingen inderdaad het super CC-gedrag bevestigen, blijft de precieze reden voor dit gedrag nog steeds onbekend. Daarnaast is het onbekend hoe individuele convectieve buien in grootte en neerslagintensiteit zullen reageren op een warmere en vochtigere atmosfeer. In dit proefschrift gebruiken we regenradargegevens voor heel Nederland en analyseren we individuele buien met een volgalgoritme. Vervolgens onderzoeken we de statistieken van de grootte en intensiteit van buien op het moment van hun piekintensiteit. De resultaten hiervan laten zien dat de ruimtelijke omvang en de intensiteit van extreme convectieve buien nauw met elkaar verbonden

zijn. Beide kenmerken nemen gezamenlijk toe, waardoor intensievere regenbuien over het algemeen ook groter zijn. Onder warmere en vochtigere omstandigheden neemt de omvang van de regenbuien snel toe bij dauwpunttemperaturen boven ongeveer 15 °C. Super CC-gedrag wordt gevonden voor alle buien in de analyse. De grootste buien zijn echter cruciaal om super CC-gedrag bij hogere temperaturen in stand te houden. Toenames van de neerslag intensiteit bij opwarming vinden plaats over het hele neerslaggebied.

Om de dynamiek van convectieve neerslagextremen in een gecontroleerde omgeving verder te bestuderen, maken we gebruik van een large eddy simulatie (LES) model. Een LES model wordt gebruikt met een ruimtelijke resolutie die fijn genoeg is om processen numeriek op te lossen die nodig zijn voor de vorming van kleinschalige onweersbuien. Verder is het mogelijk om rekening te houden met tijdsafhankelijke invloeden op het simulatiedomein, zoals een grootschalig windprofiel en grootschalige convergentie van luchtmassa's. Hiertoe gebruiken we geïdealiseerde simulaties die representatief zijn voor de geobserveerde hevige zomerse neerslag in Nederland. We simuleren een basisscenario, evenals een aantal experimenten met veranderde temperatuur en vochtigheid maar houden daarbij de relatieve vochtigheid constant. Om de kenmerken van regenbuien te bestuderen, markeren we aaneengesloten gebieden met neerslag als individuele regencellen. Op basis daarvan kunnen we de relatie tussen grootte en intensiteit van regencellen bepalen. Uit de analyses blijkt duideleijk dat in de warmere en vochtigere simulaties de regencellen groter en intenser worden terwijl het aantal kleinere regencellen juist afneemt. Deze resultaten geven een consistent beeld samen met het eerdergenoemde empirische onderzoek op basis van de neerslagradar.

Tot nu toe hebben we buien beschouwd als geïsoleerde entiteiten. Een andere factor die de omvang van regenbuien kan beïnvloeden, is het proces van convectieve organisatie. Vergelijk bijvoorbeeld een geïsoleerde convectieve regencel met een convectief systeem op de mesoschaal dat kan worden gezien als een cluster van meerdere regencellen. Deze laatste is een meer georganiseerde vorm van een convectieve regenbui. In dit geval verschilt de horizontale omvang van beide typen met ongeveer een factor tien. Lokale dynamische processen veroorzaakt door zogenaamde koude poelen ("cold pools") spelen een belangrijke rol bij de vorming van meer georganiseerde convectieve systemen. Koude poelen ontstaan door verdamping van regendruppels in de atmosfeer. Dit leidt tot een afkoeling van luchtmassa's, die sterke neerwaartse luchtstromingen veroorzaken vanwege de hogere dichtheid van koude lucht. Aan de oppervlakte spreidt de neerwaartse stroming zich horizontaal uit over een afstand van tientallen kilometers. Dit effect is voelbaar, bijvoorbeeld bij het observeren van een nabijgelegen onweersbui. De relatief dichte, bewegende luchtmassa verplaatst de omringende lucht verticaal en kan aan de rand van een dergelijke koude poel de vorming van nieuwe convectieve wolken veroorzaken. Het effect is nog sterker wanneer twee of meer koude poelen op elkaar botsen. Bovendien transporteren en brengen koude poelen vocht bijeen in geconcentreerde gebieden die geschikte locaties zijn voor nieuwe convectieve buien.

Naast het duidelijke effect van koude poelen op de vorming en organisatie van convectieve regenval is er weinig bekend over hoe deze processen veranderen in een warmer klimaat. Ook is het nog niet duidelijk hoe de dynamiek van koude poelen onder deze omstandigheden reageert en hoe dit zich verhoudt tot neerslagkenmerken. Om

dit te bestuderen gebruiken we vergelijkbare large eddy simulaties als in de voorgaande studies We herhalen de experimenten ook onder warmere en vochtiger condities. Vergelijkbaar met de eerdergenoemde methode van clustering van regencellen, passen we dezelfde techniek toe op lage temperatuur- en vochtvelden om koude poelen en relatief vochtige gebieden, zogenaamde vochtige plekken ("moist patches"), vast te stellen.

We zien dat de grotere omvang en intensiteit van regencellen onder warmere en vochtigere omstandigheden een sterke correlatie hebben met de grootte en verspreidingssnelheid van koude poelen. Dit houdt op hun beurt goed verband met de grootte en hoeveelheid vocht in vochtige plekken. Deze correlaties suggereren een positieve terugkoppeling, waarin koude poelen, die afkomstig zijn van aanvankelijk nogal willekeurig verdeelde en zwakke buien, een hogere variabiliteit in het lage vochtveld veroorzaken en buien veroorzaken die meer georganiseerd zijn en een hogere intensiteit hebben. De dynamiek van koude poelen kan dus de lokale vochtbeschikbaarheid en -toevoer naar nieuw vormende buien vergroten bij gelijkblijvende grootschalige convergentie van vocht. Uit een aparte groep experimenten leiden we af dat deze laatste grootschalige convergentie het regenceloppervlak beïnvloedt, maar niet de intensiteit.

Maar passen deze bevindingen in een realistisch scenario van klimaatopwarming? Het is bijvoorbeeld bekend dat de relatieve vochtigheid in veel regio's boven het land zal afnemen bij opwarming. Verder wordt verwacht dat de atmosfeer niet gelijkmatig met de hoogte warmer zal worden. Als gevolg van convectie zal de atmosfeer op hoogte sterker opwarmen waardoor de atmosfeer stabieler wordt ten opzichte van een gelijkmatige opwarming met de hoogte.

Ons experimentontwerp past deze principes toe en voor beide situaties worden simulatiegroepen gemaakt. We vinden dat een verminderde relatieve vochtigheid bij opwarming over het algemeen de regenbuien, de dynamiek van koude poelen en vochtige plekken verder versterkt. Dit benadrukt dat de relatieve vochtigheid, naast de neerslagintensiteit, een andere factor is die de verdampingssnelheid van regendruppels regelt en uiteindelijk de sterkte van koude poelen. Ondanks een dempend effect leiden stabielere omstandigheden met opwarming nog steeds tot intensere en grotere regenval die gepaard gaat met een sterkere koude poeldynamiek en vochtige plekken.

Ten slotte laten de resultaten gepresenteerd in dit proefschrift zien dat extreme convectieve buien een sterke reactie vertonen op klimaatopwarming en benadrukken ze het belang van kleinschalige dynamiek in deze context. Hier moet rekening mee worden gehouden voor accuratere voorspellingen van toekomstige neerslagextremen.

ZUSAMMENFASSUNG

Während ich dies hier schreibe, werden weite Teile Mitteleuropas von einer Reihe heftiger Regenfälle heimgesucht, die viele Flüsse in weniger als zwei Tagen in reißende Ströme verwandeln, Überschwemmungen verursachen, Infrastruktur und Eigentum beschädigen, und Menschen verletzen. Die Häufigkeit solcher Extremereignisse, die mit hohen wirtschaftlichen Schäden und menschlichen Opfern verbunden sind, nimmt seit Jahrzehnten zu. Wie ist das möglich? Und worin besteht der Zusammenhang zwischen extremen konvektiven Niederschlagsereignissen und steigenden Temperaturen, wie jenen, die wir derzeit aufgrund des Klimawandels erleben?

Um diesen Fragen auf den Grund zu gehen, betrachten wir die folgende vereinfachte Version eines konvektiven Regenereignisses. Wir stellen uns eine Luftsäule vor, einen Teil der Atmosphäre mit einer Wolke darin. Nahe der Oberfläche strömt Luft in die Säule, wo sie dann vertikal aufsteigt. Mit zunehmender Höhe kühlt die Luft ab, bis ab einem bestimmten Punkt der enthaltene Wasserdampf in Form kleiner Tröpfchen kondensiert. Ab dieser Höhe, der sogenannten Wolkenuntergrenze, steigt die Luftmasse weiter auf, während die Menge kondensierten Wassers immer weiter zunimmt, sodass die Wolkentröpfchen an Größe wachsen. Letztendlich setzt Niederschlag ein – im Extremfall erreicht sogar das gesamte Wolkenwasser als Regen den Boden. Diesem konzeptionellen Modell folgend, besteht eine Möglichkeit zur Erhöhung der Niederschlagsmenge darin, den Feuchtigkeitsgehalt der in die Wolke strömenden Luft zu erhöhen.

In diesem Zusammenhang spielt die sogenannte Clausius-Clapeyron-Gleichung (CC-Gleichung) eine wichtige Rolle. Sie beschreibt das Wasserhaltevermögen der Luft in Abhängigkeit von ihrer Temperatur. Erwärmt sich die Atmosphäre in Folge des Klimawandels bei gleichbleibender relativer Luftfeuchtigkeit, nimmt die in der Atmosphäre enthaltene Feuchtigkeitsmenge um etwa 7 % pro Grad Erwärmung zu. Tatsächlich wurde festgestellt, dass diese Änderungsrate eine Grenze für weltweite extreme Tagesniederschlagsmengen darstellt. Es wurde jedoch auch ermittelt, dass lokale Niederschlagsextreme auf stündlicher Veränderung und noch kürzeren Zeitskalen höhere Raten aufweisen, als es von der Clausius-Clapeyron-Beziehung erwartet wird. Dieses Phänomen wird allgemein als "Super CC-scaling" bezeichnet. Eine gängige Theorie versucht dies dadurch zu erklären, dass sich die Energiemenge, die durch Kondensation in einer konvektiven Wolke freigesetzt wird, erhöht, wenn die Feuchtigkeitsmenge zunimmt. Dies führt zu stärkeren Aufwinden und schließlich zu einem stärkeren Feuchtigkeitsstrom in die Wolkensäule.

Trotz der Tatsache, dass Stationsbeobachtungen kurzfristiger Niederschlagsextreme Super CC-scaling aufweisen können, ist der genaue Prozess hinter diesem Phänomen noch unbekannt. Darüber hinaus bleibt unklar, wie sich die Eigenschaften einzelner konvektiver Ereignisse, wie Größe und Niederschlagsintensität, in einer wärmeren und feuchteren Atmosphäre verhalten. In dieser Arbeit verwenden wir Regenradardaten mit einer vollständigen Abdeckung der Niederlande und isolieren einzelne konvektive Er-

eignisse mit einem Tracking-Algorithmus. Anschließend untersuchen wir die Statistik der Größe und Intensität von Regenereignissen zum Zeitpunkt ihrer höchsten Niederschlagsintensität. Die Ergebnisse dieser Analyse zeigen, dass die räumliche Ausdehnung und die Intensität extremer Niederschlagsereignisse eng aneinandergekoppelt sind. Beide Eigenschaften nehmen gemeinsam zu, sodass stärkere Regenereignisse in der Regel größer sind. Unter wärmeren und feuchteren Bedingungen nimmt die Größe der Ereignisse bei Taupunkttemperaturen über ungefähr 15 °C verstärkt zu. Super CC-scaling kann festgestellt werden, wenn alle Ereignisse in die Analyse einbezogen werden. Die größten Ereignisse sind jedoch entscheidend, um Super CC-scaling bei höheren Temperaturen aufrechtzuerhalten. Erhöhte Niederschlagsraten finden sich über die gesamte Fläche der Ereignisse.

Um die Dynamik konvektiver Niederschlagsextreme in einer kontrollierten Umgebung weiter zu untersuchen, verwenden wir ein sogenanntes «Large Eddy Simulation»-Modell (LES-Modell). Ein LES-Modell kann mit einer ausreichend hohen Auflösung betrieben werden, um Prozesse darzustellen, die für die Bildung von kleinräumigen Gewittern notwendig sind. Weiterhin ist es möglich, zeitabhängige externe Einflüsse auf den Simulationsbereich zu berücksichtigen, wie beispielsweise ein großräumiges Windprofil und Konvergenz. Hier verwenden wir einen idealisierten, aber realistischen Fallaufbau, der für starke Sommerniederschläge in den Niederlanden repräsentativ ist. Unter der Annahme einer konstanten relativen Luftfeuchtigkeit simulieren wir den Basisfall sowie eine Reihe von Experimenten mit veränderter Temperatur und Feuchtigkeit. Um die Eigenschaften von Regenereignissen zu untersuchen, gruppieren wir kontinuierliche Bereiche mit Niederschlag zu Regenzellen (Clustering). Auf dieser Grundlage können wir den Zusammenhang zwischen Größe und Intensität von Regenzellen nachweisen und bestätigen. In wärmeren und feuchteren Simulationen werden Regenzellen größer und über ihre gesamte Fläche intensiver. Die Zahl großer Ereignisse steigt auf Kosten der kleineren. Diese Ergebnisse zeichnen zusammen mit der bereits erwähnten beobachtungsbasierten Studie ein konsistentes Bild.

Bisher haben wir Niederschlagsereignisse als isolierte Einheiten betrachtet. Ein weiterer Faktor, der das Ausmaß von Regenereignissen beeinflussen kann, ist jedoch der Prozess der konvektiven Organisation. Diesen Prozess kann man nachvollziehen, wenn man etwa eine isolierte Konvektionszelle mit einem mesoskaligen Konvektionssystem vergleicht, das als Ansammlung mehrerer Gewitter betrachtet werden kann. Letzteres kann als eine stärker organisierte Form eines konvektiven Niederschlagsereignisses angesehen werden. Dabei unterscheidet sich die horizontale Ausdehnung der beiden Typen um etwa den Faktor zehn. Lokale Dynamiken, die durch sogenannte "Cold Pools" verursacht werden, spielen dabei eine Schlüsselrolle, insbesondere bei der Bildung stärker organisierter Ereignisse. Cold Pools entstehen durch die Verdunstung von Regentropfen in der Atmosphäre. Dies bewirkt eine Abkühlung von Luftmassen, die dann aufgrund ihrer relativ höheren Dichte wiederum die Abwindgeschwindigkeit verstärken. An der Oberfläche breiten sich die Abwinde dann horizontal über eine Entfernung von mehreren zehn Kilometern aus. Dieser Effekt ist zum Beispiel bei der Beobachtung eines nahen Gewitters spürbar. Die relativ dichte Luftmasse, die sich dabei ausbreitet, verlagert die umgebende Luft vertikal und kann die Bildung neuer Konvektionszellen auslösen. Der Effekt ist noch stärker, wenn zwei oder mehrere Cold Pools kollidieren. Außerdem

transportieren Cold Pools Feuchtigkeit, was zur Akkumulation an anderen Orten führt, die wiederum bevorzugte Stellen für neue konvektive Ereignisse sind.

Abgesehen von der deutlichen Wirkung von Cold Pools auf die Entstehung und Organisation konvektiver Niederschlagsereignisse ist wenig darüber bekannt, wie sich diese Prozesse in einem wärmeren Klima verändern. Unklar bleibt auch, wie sich die Dynamik von Cold Pools unter diesen Bedingungen verhält und wie dies mit der Größe und Intensität von Niederschlagsereignissen zusammenhängt. Um dies zu untersuchen, verwenden wir eine ähnliche Konfiguration des LES-Modells wie im bereits genannten Fall. Wir wiederholen zunächst auch denselben Versuchsaufbau wie zuvor, nämlich mit einer wärmeren und feuchteren Einstellung. Ähnlich wie bei der zuvor erwähnten Methode des Regenzellen-Clusterings wenden wir die gleiche Technik auf Temperatur- und Feuchtigkeitsfelder an, um Cold Pools und relativ feuchte Bereiche, sogenannte "Moist Patches", zu identifizieren.

Es ergibt sich, dass eine erhöhte Größe und Intensität von Regenzellen unter wärmeren und feuchteren Bedingungen eine starke Korrelation mit der Größe und Ausbreitungsgeschwindigkeit von Cold Pools hat. Dies wiederum hängt stark mit der Größe und Menge jener Feuchtigkeit zusammen, die in Moist Patches enthalten ist. Diese Korrelationen legen eine Rückkopplungsschleife nahe, in der Cold Pools, die von anfänglich eher zufällig verteilten und schwachen Regenereignissen stammen, eine höhere Variabilität im bodennahen Feuchtigkeitsfeld verursachen und stärker organisierte Ereignisse mit höherer Intensität auslösen. Somit kann die Dynamik von Cold Pools die lokale Feuchtigkeitsverfügbarkeit für neu entstehende Regenereignisse ohne zusätzliche großräumige Konvergenz erhöhen. Aus einer separaten Gruppe von Experimenten können wir außerdem schlussfolgern, dass verstärkte großräumige Konvergenz allein die Ausdehnung von Regenzellen, nicht aber deren Intensität beeinflusst.

Aber halten die bisherigen Ergebnisse in einem realistischeren Szenario der Klimaerwärmung Stand? Es ist beispielsweise bekannt, dass in vielen Regionen über Land die relative Luftfeuchtigkeit mit der Erwärmung abnimmt. Außerdem wird erwartet, dass sich die verschiedenen Schichten der Atmosphäre nicht in gleichem Maße erwärmen. Aufgrund von Konvektion folgt das Temperaturprofil eher einer Änderung nach dem feucht-adiabatischen Gradienten, was zu einer stabileren Atmosphäre führt. Unser Versuchsdesign wendet diese Prinzipien an und für beide Situationen werden separate Simulationsgruppen erstellt. Wir stellen fest, dass eine Erwärmung, einhergehend mit einer reduzierten relative Luftfeuchtigkeit, im Allgemeinen Niederschlagsereignisse, Cold-Pool-Dynamiken und Moist Patches weiter verstärkt. Dies hebt die relative Luftfeuchtigkeit, neben der Niederschlagsintensität, als weiteren Faktor hervor, der die Verdunstungsrate von Regentropfen und letztendlich die Stärke von Cold Pools steuert. Selbst wenn sich die Atmosphäre bei Erwärmung stabilisiert, führt dies, trotz dämpfender Wirkung, immer noch zu intensiveren und größeren Niederschlagsereignissen, die mit einer stärkeren Cold-Pool-Dynamik und Moist Patches verbunden sind.

Schließlich zeigen die in dieser Dissertation präsentierten Ergebnisse, dass extreme konvektive Niederschlagsereignisse stark auf eine Klimaerwärmung reagieren und unterstreichen in diesem Zusammenhang die Bedeutung kleinräumiger Dynamiken. Dies muss für bessere Vorhersagen zukünftiger Extreme berücksichtigt werden.

Resumen

Mientras escribo estas líneas, parte de Europa Central se encuentra sumida en una serie de intensas lluvias que, en menos de dos días, han provocado el desbordamiento de los ríos, causando inundaciones y dañando infraestructuras, propiedades y ocasionando numerosas víctimas. El número de estos eventos extremos, además de suponer un gran impacto en pérdidas económicas y humanas han venido incrementándose desde hace décadas, ¿Cómo está sucediendo esto? y ¿Cuál es la relación que guardan estas precipitaciones extremas y el incremento de las temperaturas como consecuencia del cambio climático?

Para abordar estas preguntas, considere la siguiente versión simplificada de un evento de lluvia convectiva. Imaginemos una columna de aire, parte de la atmósfera, con una nube en su interior; Cerca de la superficie, el aire fluye hacia la columna y comienza a ascender verticalmente. Mientras gana altura, el aire se enfría, hasta que, a cierto nivel el vapor de agua contenido se condensa en forma de pequeñas gotas de agua. A partir de este nivel, la base de la nube, la masa de aire continua ascendiendo mientras la cantidad de agua condensada sigue aumentando, de modo que las pequeñas gotas de agua van aumentando de tamaño. Finalmente, cuando crezcan lo suficiente, se producirán precipitaciones y, en el caso más extremo, el agua acumulada en la nube alcanzará la superficie en forma de lluvia. Siguiendo este modelo conceptual, una forma de aumentar la cantidad de precipitación sería aumentando el contenido de humedad del aire que entra en la nube.

En este caso, la relación Clausius-Clapeyron (CC) juega un papel importante, debido a que, describe la capacidad de retención del agua en el aire con respecto a su temperatura. Si la humedad relativa se mantiene climatológicamente estable con el calentamiento global, entonces la cantidad de humedad contenida en la atmósfera aumentará a una tasa de alrededor el 7% por cada grado que incremente la temperatura. En efecto, se encontró que, a nivel global, las cantidades extremas de precipitación diaria están limitadas por esta tasa de cambio. Sin embargo, a nivel local estas precipitaciones extremas, basadas en escalas de tiempo por hora y sub-hora, parecen mostrar tasas más altas que las dictadas por la relación Clausius-Clapeyron. Este fenómeno es denominado comúnmente como "super CC-scaling". Para explicar este comportamiento, una teoría común sugiere que si la cantidad de humedad aumenta, la cantidad de energía liberada a través de la condensación en una corriente ascendente convectiva se intensificará. Esto dará lugar a corrientes ascendentes más fuertes y, en última instancia, a una convergencia de humedad más fuerte en la columna de la nube.

A pesar de que las estaciones de observación de precipitaciones extremas, en intervalos breves de tiempo, pueden mostrar el fenómeno super CC-scaling, el proceso exacto detrás de este fenómeno aún se desconoce. Además de esto, no está del todo claro cómo las características de los eventos convectivos individuales, como el tamaño y la intensidad de la precipitación, responderán a una atmósfera más cálida y húmeda. En

esta tesis hemos utilizado los datos del radar de lluvia abarcando los Países Bajos a completo y aislando los eventos convectivos individuales con un algoritmo de seguimiento. Posteriormente, investigamos las estadísticas en tamaño e intensidad de los eventos de lluvia en el momento que alcanzan su intensidad máxima. Los resultados de este análisis muestran que la extensión espacial y la intensidad de los eventos convectivos extremos están estrechamente relacionadas. Ambas características aumentan conjuntamente, lo que significa que los eventos de lluvia más fuertes son generalmente más grandes. En condiciones más cálidas y húmedas, el tamaño de los eventos aumenta rápidamente a temperaturas del punto de rocío por encima de los 15 grados centígrados; El fenómeno super CC-scaling se encuentra al incluir todos los eventos en el análisis. Sin embargo, los eventos más grandes son cruciales para mantener este fenómeno a temperaturas más altas. De esta forma, aparecen tasas de precipitación mejoradas en toda el área del evento.

Para estudiar más a fondo la dinámica de los extremos de precipitación convectiva en un entorno controlado, hemos utilizado el modelo LES (large eddy simulation). Este modelo puede ejecutarse a una resolución lo suficientemente alta para resolver los procesos que son necesarios para desarrollar la formación de tormentas eléctricas a pequeña escala. Además, es posible tener en cuenta las influencias que dependen del tiempo en el dominio de la simulación, como un perfil de viento a gran escala y la convergencia. Aquí, aplicamos una configuración de caso idealizada, pero realista, que es representativa de las fuertes lluvias torrenciales que suceden en los Países Bajos; Simulamos el caso base, así como una serie de experimentos con cambios de temperatura y humedad siguiendo el supuesto de humedad relativa constante. Para estudiar las características de los eventos de lluvia, agrupamos áreas continuas con precipitación en células de lluvia. En base a lo anterior, podemos confirmar la relación entre el tamaño y la intensidad de las células de lluvia. En simulaciones más cálidas y húmedas, las células de lluvia crecen, volviéndose más intensas en toda su área; El número de grandes eventos aumenta a costa de eventos más pequeños; Estos resultados dibujan una imagen consistente, junto con el estudio basado en las observaciones mencionadas anteriormente.

Hasta ahora, hemos considerado los eventos de precipitación como entidades bastante aisladas entre sí. Sin embargo, otro factor que puede influir en la magnitud de estos eventos, sería el proceso de organización convectiva. Por ejemplo, compare una celda convectiva aislada con un sistema convectivo de mesoescala que puede verse como un grupo de múltiples tormentas eléctricas. Este último puede mostrarse como una forma más organizada de un evento de precipitación convectiva. En este caso, la extensión horizontal de los dos tipos, difiere alrededor de un factor de diez. Las dinámicas locales inducidas por el fenómeno denominado "cold pools" juegan un papel clave en la formación de eventos más organizados. Estos eventos (cold pools) se originan por la evaporación de las gotas de lluvia en la atmósfera, lo que provoca un enfriamiento de las masas de aire que, intensifica la fuerza de la corriente descendente debido a su densidad relativamente más alta; En la superficie, la corriente descendente se extenderá horizontalmente a decenas de kilómetros de distancia. Este efecto es tangible, por ejemplo, al observar una tormenta eléctrica cercana. La masa de aire en movimiento, relativamente densa, disloca verticalmente el aire circundante y puede desencadenar la formación de nuevas nubes convectivas; El efecto es aún más fuerte cuando dos o más de los fe-

nómenos mencionados anteriormente chocan entre sí. Además, las denominadas cold pools transportan y acumulan humedad a regiones confinadas, que representan el lugar idóneo para el desarrollo de nuevos eventos convectivos.

Además del efecto de este fenómeno (cold pools) en la formación y organización de los eventos de lluvia convectiva, poco se sabe acerca de cómo estos procesos cambian en un clima más cálido. Cómo responde la dinámica de este fenómeno en estas condiciones y cómo esto se relaciona con las características de la precipitación se considera aún, una pregunta abierta. Para profundizar en esto, usamos una configuración del modelo LES similar a la del caso mencionado anteriormente; También repetimos los experimentos con un ambiente más cálido y húmedo. De manera similar al método mencionado anteriormente sobre el agrupamiento de células de lluvia, aplicamos la misma técnica a campos de temperatura y humedad de bajo nivel para identificar las denominadas cold pools y áreas relativamente húmedas, los denominados parches de humedad ("moist patches").

Hemos visto que el aumento del tamaño e intensidad de las células de lluvia en condiciones más cálidas y húmedas tienen una fuerte correlación con el tamaño y la velocidad de propagación de las cold pools. Esto, a su vez, se relaciona bien con el tamaño y la cantidad de humedad contenida en los anteriormente denominados parches de humedad. Estas correlaciones sugieren un ciclo de retroalimentación, en el que este fenómeno (cold pools) que se originan en eventos de lluvia débiles y distribuidos inicialmente de manera bastante aleatoria, causan una mayor variabilidad en el campo de humedad de bajo nivel, desencadenando eventos que se encuentran más organizados y de mayor intensidad. Por lo tanto, la dinámica del fenómeno cold pools puede mejorar la disponibilidad de humedad local y el suministro a los eventos de lluvia de nueva formación sin una convergencia adicional a gran escala. De un grupo separado de experimentos, deducimos que la convergencia mejorada a gran escala por sí sola solo afecta el área de la celda de lluvia, pero no la intensidad.

Sin embargo, ¿se mantienen estos hallazgos en un escenario más realista de calentamiento climático? Por ejemplo, se sabe que la humedad relativa disminuirá debido al calentamiento climático en muchas regiones terrestres; Además, se espera que la atmósfera no se caliente uniformemente con la altura. Debido a la convección, el perfil de temperatura seguirá un cambio cercano a una tasa de caída adiabática húmeda, lo que conducirá a una atmósfera más estable. El diseño de nuestro experimento aplica estos principios y se crean grupos de simulación separados para ambas situaciones. Encontramos que una humedad relativa reducida con el aumento de la temperatura, generalmente amplifica aún más los eventos de precipitación, la dinámica de las denominadas cold pools y los parches de humedad. Esto resalta la humedad relativa, además de intensificar la precipitación, como otro factor que controla la tasa de evaporación de las gotas de lluvia y, en última instancia, la fuerza de las cold pools. A pesar de este efecto de amortiguación, las condiciones más estables con un aumento de la temperatura aún conducen a eventos de lluvia más intensos y más grandes que se asocian con una dinámica más intensa de los denóminados cold pools y parches húmedos.

Finalmente, los resultados presentados en esta tesis muestran que los eventos de precipitación convectiva extrema exhiben una fuerte respuesta al calentamiento climático y resaltan la importancia de la dinámica a pequeña escala en este contexto. Esto

debe tenerse en cuenta para predecir mejor los futuros eventos extremos.

1

INTRODUCTION

Let us begin this thesis with a typical summer day: clear blue sky, the sun is shining and temperatures are already well above 20 °C at 10am. Later in the afternoon you decide to escape the heat in your study room and jump on your bike to drive to the nearby canal for a swim. While driving, you barely notice that the first clouds are forming at the horizon. After a refreshing swim you lay in the sun to dry. A few hours pass until you notice that the sky has gotten much darker and towers of clouds have formed above you. It is the moment when you realize that it is time to leave and go home. A gentle breeze cools you down during the first minutes of your journey, but wind speeds ramp up quickly. The first rain drops land while you are waiting for a green light at a road crossing. Everything happens fast from now on. The heavy rain reduces visibility to a few tens of meters and strong wind gusts try to push you down. The rain water accumulates in the streets as the sewer system is at its maximum capacity. While seeking shelter at a close-by building you notice that even the cars stopped to wait it out. At that point you realize, this is a serious extreme convective precipitation event I've gotten into.

Only minor damage occurred on that day and the author of this thesis got away soaked and with cold feet, but the described characteristics make convective precipitation extremes a hazard for humans, their possessions and the environment we live in. For instance, a series of convective storms in the Lisbon metropolitan area in 2008 caused casualties and 25 % of all flood-related insurance claims of the entire decade. The event produced local precipitation amounts of up to 140 mm within 24 hours [Leal et al., 2018, 2019]. Similarly, numerous thunderstorms delivered more than 130 mm within a few hours at several locations in the Netherlands on July 2014. The damages caused by this event were estimated to more than 10 million Euros [Eden et al., 2018]. These are just two examples of high-impact convective precipitation extremes, but insurance data show that the number of such events and the associated economic losses have increased over the past decades [Hoeppe, 2016].

Given the strong potential for a high socio-economical impact, it is crucial to investigate how rainfall extremes respond to climate change. Global temperatures have been increasing and it is now widely accepted that annual precipitation amounts exhibit significant positive trends in many regions over land in midlatitudes [Hartmann et al.,

1

1

2013]. However, results are less clear for rainfall extremes due to regional variations, especially for short-term intervals on subdaily or even hourly basis, and confidence is even lower for changes in local phenomena like thunderstorms [Hartmann et al., 2013]. This is mostly because of a lack of high-resolution and long time series of observational data, which is essential to capture the rare temporal occurrence and the small-scale nature of such events. On the prediction side and with a future perspective modeling the climate system has made substantial progress over the past decades. For instance, the horizontal resolution of global climate models has increased at least five fold in the past three decades [Le Treut et al., 2007; Cubasch et al., 2012]. Nevertheless, even current high-resolution global climate models can either not fully resolve the small spatial scale of convective extremes or, if so, are computationally too expensive to produce enough data. This is also true for regional convection permitting models that typically run at even higher resolutions up to the kilometer scale [Hirt et al., 2020].

This thesis follows a different path. In a bottom-up approach, we focus on the local event perspective and dive into the characteristics of convective rainfall extremes and how processes could change in a warming climate. Therefore, we make use of high-resolution radar observations and subkilometer modeling in combination with a tracking algorithm that allows the extraction of event properties such as peak intensity, average intensity and precipitation area. The remainder of this chapter prepares the reader with processes that are relevant in the context, elaborates on the event-based approach and, finally, the specific scope and research questions of this thesis.

1.1. CONVECTIVE PRECIPITATION EXTREMES

1.1.1. CONVECTIVE PRECIPITATION

In meteorology, one generally distinguishes between two categories of rainfall formation: dynamic and convective. Both require that air is lifted to a point where the water vapor condenses and water droplets form. The result is cloud formation. The water droplets will eventually grow in size until their mass cannot be suspended in the air and they fall to the ground as rain. However, the mechanism of lifting is fundamentally different. In the case of dynamic precipitation, it is the result of large-scale lifting of air masses near frontal systems like extratropical cyclones, or forced lifting through physical obstacles such as mountain ridges. These subcategories are called stratiform and orographic precipitation, respectively.

Convective precipitation behaves differently. Figure 1.1 shows an example for illustration. Consider an air parcel (p) with a certain temperature T_p and specific humidity q_p, located near the surface. Initially, T_p equals the temperature of the environmental (e) air T_e. When heated, for example, through solar radiation, T_p will increase and the air parcel will expand making it positively buoyant, meaning that it becomes lighter than the surrounding air. While rising, T_p will decrease with a dry adiabatic lapse rate of $9.8\,\mathrm{K\,km^{-1}}$. Provided that the environmental lapse rate, the rate at which T_e decreases with height, is stronger than the lapse rate of T_p, the air parcel will remain buoyant and continue to rise. As T_p keeps decreasing, it will eventually reach a point where the water vapor in the air parcel will start to condensate and q_p diminishes. This marks the lifting condensation level (LCL), the cloud base of a convective cloud. Moreover, condensation

Figure 1.1: A convective cloud with precipitation at the cost of Arcachon, France. The horizontal line marks the cloud base (lifting condensation level). Arrows indicate convergence near the surface, the main updraft of the cloud and the divergence zone at cloud top.

releases latent heat which will decrease the adiabatic lapse rate of the air parcel, leading to more buoyancy and stronger convective updrafts. As the parcel keeps ascending, the amount of condensed water keeps increasing. Precipitation sets in eventually when the amount of condensed water typically exceeds a value of $1\,\mathrm{g\,kg^{-1}}$. The ultimate result is a characteristic cumulonimbus cloud, as seen in Figure 1.1. Convection will finally cease when the conditions stabilize.

Besides the underlying mechanism there are other characteristics that separate convective from dynamic precipitation. For instance, a single convective cloud only covers a relatively small area with a cross section of a few kilometers, while stratiform precipitation from nimbostratus clouds, associated with frontal systems, can span over hundreds of kilometers. Also, the life cycles of the two precipitation types differ. Figure 1.2 shows that convective events exhibit much higher instantaneous rainfall rates and the event peak is reached shortly after precipitation onset. Rain rates during stratiform events remain rather constant at a much lower level. Thus, convective precipitation is rather associated with flash floods with large amounts of rain in relatively short time. However, stratiform rainfall can last for multiple hours or even days with considerable accumulation of rainwater.

Finally, it is worth to mention that in reality the two precipitation types do not necessarily happen completely isolated. It is very well possible that in frontal systems alongside with stratiform precipitation, instabilities initiate convection and cause convective rainfall events. This is also true for the orographic subcategory. In both cases, the forced lifting can act as a trigger to overcome the initially stable condition.
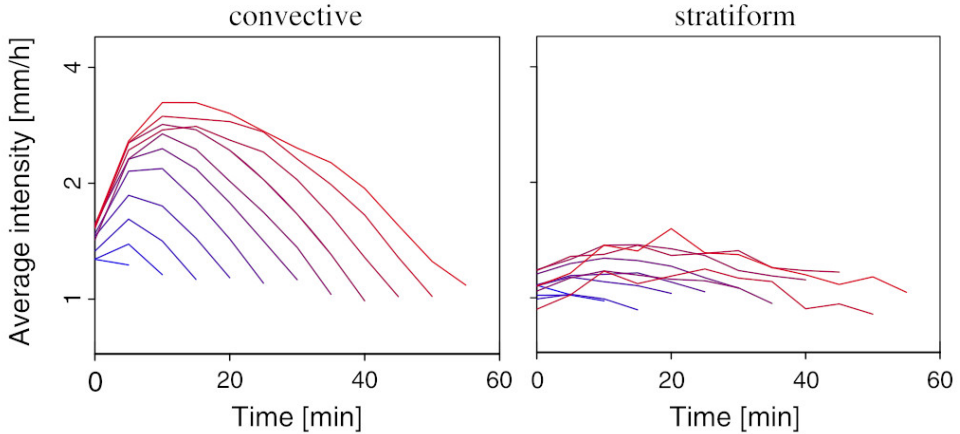
Figure 1.2: Typical life cycles of convective and stratiform precipitation events. Colors indicate the lifetime of tracks in 5-minute steps from blue to red. Reproduced with permission from Moseley et al. [2013].

1.1.2. EXTREME PRECIPITATION

The exact definition of precipitation extremes varies across the scientific literature. In general, an extreme event involves rare occurrence, high magnitude and/or high impact. High impact is a complex combination of several factors. High intensity is a major contributor, but other aspects such as geographical conditions, land cover and exposure play a crucial role as well [see e.g., Oppenheimer et al., 2012]. For instance, the two examples from the first part of this introduction might have caused significantly lower economical damage if they would have happened over a scarcely populated rural area. However, this thesis does not follow the line of impact research. Instead, we focus on extreme events defined by the frequency of occurrence. This aspect is naturally coupled to the magnitude. Figure 1.3a shows an example of an empirical distribution of 10-minute precipitation sums at a single station, here De Bilt in the Netherlands. It gets clear that higher precipitation sums have drastically lower frequencies than smaller sums. It is this tail of the distribution where we find extreme precipitation events that are relevant for the context of this thesis. A more detailed picture of this part of the distribution can be obtained by using the cumulative distribution in form of percentiles. A percentile, as the name suggests, gives the value that a certain percentage of data records does not exceed. Figure 1.3b shows this for the top-end part of the distribution. The marked 99th percentile indicates that 99 % of the records have a value of less or equal to 1.75 mm/10min. In other words, only 1 % of the data exceed 1.75 mm/10min. The percentile-based definition of extreme is used numerous times throughout this thesis. Typically, high values are chosen, such as the 95th, 97.5th or even the 99.99th percentile.

Special care must be taken if a percentile based extreme index is used in combination with a threshold, such as a minimum precipitation rate above zero, like in the example in Figure 1.3. Significant changes in the frequency of rain events over time can produce artifacts that must be taken into account when interpreting the results [Schär et al., 2016]. However, time series analysis is not a subject of this thesis. Instead, the focus lies on
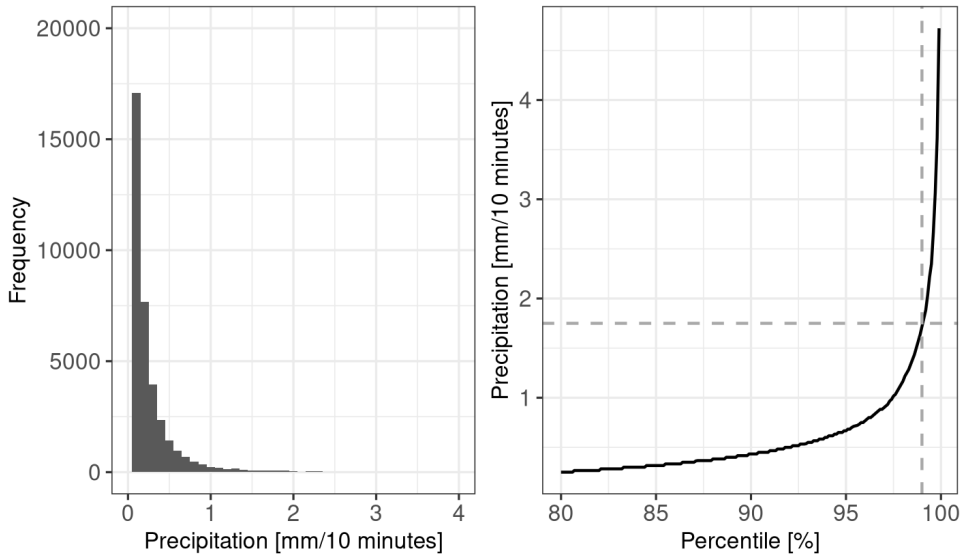
Figure 1.3: Histogram (a) and cumulative distribution (b) of 10 minute precipitation sums at De Bilt, Netherlands station for 2004 to 2015. Dashed lines in (b) highlight the 99th percentile and its value. Only records with precipitation greater than zero are included. Data retrieved from KNMI Data Platform [2021].

non-impact related processes. In pragmatic terms one could say that we simply want to know how the precipitation intensity is changing under different external conditions.

1.2. DRIVERS OF CONVECTIVE PRECIPITATION

In order to assess the effect of a warming climate on rainfall extremes, it is important to point out which processes contribute to the amount of precipitation that eventually reaches the surface.

1.2.1. THERMODYNAMICS AND PRECIPITATION SCALING

The American Heritage Dictionary defines rain as "Water condensed from atmospheric vapor and falling in drops". Although simple, this definition highlights one of the most fundamental properties of our planets atmosphere, its water holding capacity. It was formally described in the 19th century as the Clausius-Clapeyron (CC) equation. It relates the saturation water vapor pressure e_s to temperature T, and is often written in this form

$$\frac{de_s}{e_s} = \frac{L_v dT}{R_v T^2},$$

(1.1)

where R_v is the gas constant for water vapor and L_v is the latent heat of vaporization [e.g., Trenberth et al., 2003]. Considering an air parcel at a given temperature T, condensation occurs when the actual water vapor pressure e exceeds e_s, or in other words, when the

relative humidity

$$RH \equiv 100 \times \frac{e}{e_s} \tag{1.2}$$

is greater than 100 %.

For good approximation, 0.3 % error over the temperature range from $-35\,°C$ to $35\,°C$,

$$e_s(T) = 6.112 \exp\left(\frac{17.67T}{T + 243.5}\right) \tag{1.3}$$

can be used to directly compute e_s from T (in °C) [Bolton, 1980]. The graphical representation in Figure 1.4a illustrates the exponential relationship between the two parameters.
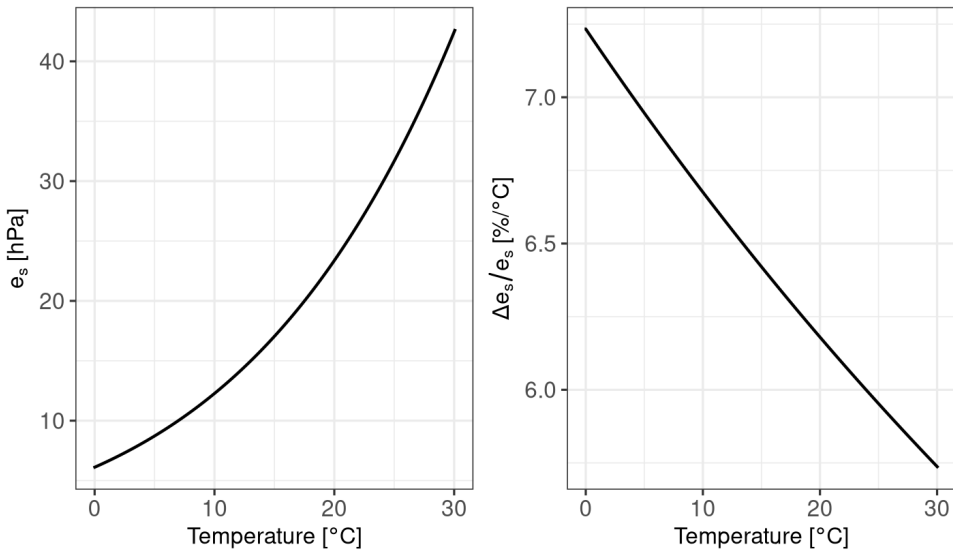
Figure 1.4: The saturation water vapor pressure (e_s) over a temperature range of 30 °C, computed from Equation 1.3 (a). The fractional rate of change ($\Delta e_s/e_s$) varies with temperature between approximately $7\,\%\,°C^{-1}$ at lower and $6\,\%\,°C^{-1}$ at higher temperatures (b).

The relevance of the $T - e_s$ relation for precipitation extremes becomes clear when looking back to Figure 1.1. In this thought experiment moist air enters the cloud at the base and ascends in the updraft where, at some height, the moisture will condense and precipitate out. Dry air leaves the column at the cloud top. We can derive that precipitation is proportional to the water vapor pressure at the surface which in turn is proportional to the specific humidity q,

$$P \propto e \propto q. \tag{1.4}$$

A reasonable first order approximation for midlatitudes is that relative humidity remains unchanged with climatic warming [Attema et al., 2014]. Thus, more moisture will enter a cloud when the temperature increases. The additional moisture will lead eventually to

higher precipitation amounts. More specifically, we can write the response of precipitation at two different temperatures as

$$\frac{P_2}{P_1} = \frac{RHe_s(T_2)}{RHe_s(T_1)}. \tag{1.5}$$

The change of precipitation follows the CC relation. This is where the rate of change of the water holding capacity of air comes into play. As shown in Figure 1.4b, e_s will increase approximately at a rate between 6 % and 7 % per degree temperature change. In the past decades numerous studies have shown that globally and on long time scales, precipitation extremes roughly follow this rate of change [e.g., Pall et al., 2007; Allen and Ingram, 2002]. This mechanism is commonly known as CC-scaling.

It is important to note that the CC-scaling only applies to the tail of the precipitation distribution, that means the highest percentiles. The global mean precipitation rate on the other hand is constrained by the energy budget rather than the available moisture and follows a much lower rate of about $3\,\%\,K^{-1}$ [e.g., Allen and Ingram, 2002].

The above mentioned mechanism of CC-scaling assumes that relative humidity remains constant as temperature increases meaning that the water vapor content scales according to the CC equation. This assumption is not always fully satisfied over land in midlatitudes [O'Gorman and Muller, 2010] which is why the dew point temperature is a better measure to relate precipitation extremes to changes in atmospheric moisture [Lenderink and van Meijgaard, 2010; Wasko et al., 2018]. The dew point temperature T_d is the temperature to which air must be cooled until condensation occurs or in other words RH is 100 %. It is defined as $e = e_s(T_d)$ and can be directly computed from e by inverting Formula 1.3 to

$$T_d = \frac{243.5}{\frac{17.67}{\ln(e/6.112)} - 1}, \tag{1.6}$$

where T_d is in degree Celsius. Thus, an increase of T_d by 1 °C results in a proportional increase of water vapor content according to the CC relation.

By substituting T_d for T in Equation 1.5, we finally eliminate RH from the scaling relation:

$$\frac{P_2}{P_1} = \frac{e_s(T_{d,2})}{e_s(T_{d,1})}. \tag{1.7}$$

1.2.2. DYNAMICS AND SUPER CC-SCALING

Besides the aforementioned thermodynamic increase of moisture supply there is a second way to amplify the moisture flux into a cloud. Enhanced dynamics lead to a larger moisture convergence. Again, we can use Figure 1.1 to qualitatively illustrate the effect. As soon as convection initiates air parcels rise in the updraft of a convective cloud. The consequence is a relatively low air pressure at the location of origin of the rising air masses near the surface. This deficit causes an inflow of surrounding air. Increasing the inflow will lead to a higher moisture flux into the convective cloud even without changing the water vapor content.

In a more formal way, we can derive a moisture budget of the atmosphere from the

1

advection equation in flux form

$$\frac{\partial \overline{q_v}}{\partial t} = -\frac{\partial \overline{uq_v}}{\partial x} - \frac{\partial \overline{vq_v}}{\partial y} - \frac{1}{\rho}\frac{\partial \rho \overline{wq_v}}{\partial z} - G,$$

(1.8)

where q_v is the water vapor specific humidity, t is time, u, v and w are the wind components in x, y and z direction and ρ is the density. G represents the autoconversion of cloud droplets to precipitation. The overbars denote the horizontal mean. The vertical integration of this equation from surface to the top of the atmosphere (TOA) results in

$$\underbrace{\left\langle \frac{\partial \overline{q_v}}{\partial t} \right\rangle}_{S} = \underbrace{-\left\langle \frac{\partial \overline{uq_v}}{\partial x} \right\rangle - \left\langle \frac{\partial \overline{vq_v}}{\partial y} \right\rangle}_{MC} + \underbrace{\rho_{sfc}(\overline{wq_v})_{sfc}}_{E} - P.$$

(1.9)

Here, S denotes the storage term, MC the moisture convergence and E is surface evaporation. Since we assume that all condensed water vapor precipitates out, G can be replaced with precipitation P. Angled brackets represent the mass weighted vertical integral following

$$\langle \ldots \rangle = \int_{sfc}^{TOA} (\ldots) \rho \, dz.$$

(1.10)

At this point, it is worth to mention that MC in equation 1.9 can be further decomposed into an advection and convergence term

$$\underbrace{-\left\langle \frac{\partial uq_v}{\partial x} \right\rangle - \left\langle \frac{\partial vq_v}{\partial y} \right\rangle}_{MC} = \underbrace{-\left(\left\langle u\frac{\partial q}{\partial x} + v\frac{\partial q}{\partial y} \right\rangle \right)}_{advection} - \underbrace{\left\langle q\left(\frac{\partial u}{\partial x} + \frac{\partial v}{\partial y} \right) \right\rangle}_{convergence}.$$

(1.11)

Here, we assume that variations of q_v along x and y are negligible, hence the missing overbars. In practice and certainly in the case of this thesis, the convergence term can be considered as the dominant contributor to the local moisture tendency. Furthermore, when equation 1.9 is integrated over large areas and long time intervals, S is relatively small. This leads essentially to a balance between MC and E as moisture inputs and P as output. For short time scales and integrated over small areas such as the footprint of convective clouds, MC and E are partly precipitated out and partly stored.

As mentioned in the beginning of this section, the dynamics associated with convective clouds have a different character near the surface than in the actual updraft of the cloud. Thus, it is useful to separate the moisture budget from equation 1.9 into a subcloud and cloud part. We do this by following the schematic in Figure 1.5. The equations for the lower and higher part follow almost directly from equation 1.9 as

$$\left\langle \frac{\partial \overline{q_v}}{\partial t} \right\rangle_{low} = -\left\langle \frac{\partial \overline{uq_v}}{\partial x} \right\rangle_{low} - \left\langle \frac{\partial \overline{vq_v}}{\partial y} \right\rangle_{low} - \rho_{cb}(\overline{wq_v})_{cb} + \rho_{sfc}(\overline{wq_v})_{sfc}$$

(1.12)

and

$$\left\langle \frac{\partial \overline{q_v}}{\partial t} \right\rangle_{high} = -\left\langle \frac{\partial \overline{uq_v}}{\partial x} \right\rangle_{high} - \left\langle \frac{\partial \overline{vq_v}}{\partial y} \right\rangle_{high} + \rho_{cb}(\overline{wq_v})_{cb} - P.$$

(1.13)
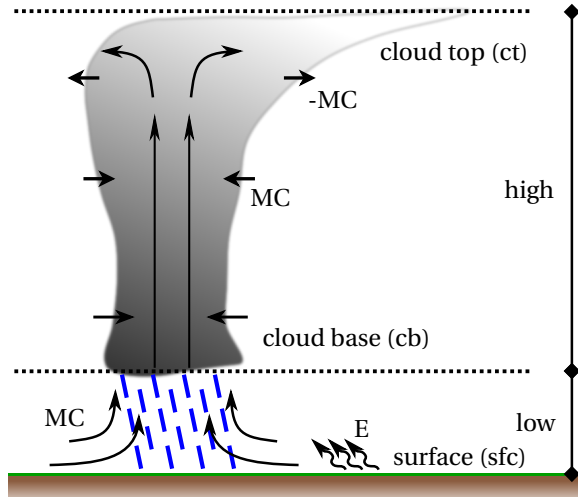
Figure 1.5: A simple moisture budget of a convective cloud separated into subcloud (low) and cloud (high) part. The main moisture supply to the cloud stems from moisture convergence (MC) and, to a lesser extent, surface latent heat flux (E) in the subcloud layer. The budget in the cloud layer is balanced by precipitation. In general, MC remains relatively small over the height of the cloud and is even negative (-MC) at the cloud top due to divergence. Note that for the purpose of simplification, we assume that vertical transport at the cloud top is negligible.

Here, the angled brackets stand for the vertical integration over the respective part of the atmosphere (see Figure 1.5), which is guided by

$$\langle\dots\rangle_{low} = \int_{sfc}^{cb} (\dots)\rho dz \qquad \text{and} \qquad \langle\dots\rangle_{high} = \int_{cb}^{ct} (\dots)\rho dz. \qquad (1.14)$$

For the purpose of simplification, we assume that the vertical transport at the cloud top is negligible. The differences between equations 1.12 and 1.13 are the sign of the vertical moisture fluxes at cloud base and the moisture flux at the surface as a source in the lower part versus precipitation as a moisture sink in the higher part.

MC and (to a lesser extent) surface evaporation are the main supplier of the moisture flux that leaves the subcloud layer at the cloud base. Especially MC, but also the moisture flux into the cloud layer can be strongly modified by low-level dynamics such as cold pools (see section 1.2.3). Thus, the main influx of moisture into the cloud layer comes from the subcloud layer. Inside the cloud layer the systematic difference between moisture inflow at lower levels of the cloud (with high q_v) and moisture outflow (with low q_v) causes a positive net convergence of moisture. On the time scale of convective rainfall events part of this moistening is used for precipitation and another part goes into the storage term of the atmosphere.

How is this related to enhanced precipitation extremes at higher temperatures? As previously mentioned, it is now widely accepted that rainfall extremes globally increase within the bounds as dictated by the CC relation. On local spatial and short time scales,

however, it has been found that the scaling of rainfall rates with temperature and moisture availability can exceed the CC-scaling rate, even by up to a factor of two [Lenderink and van Meijgaard, 2008; Lenderink et al., 2017; Loriaux et al., 2013]. This phenomenon is commonly referred to as super CC-scaling. Looking at equations 1.12 and 1.13, the horizontal convergence term increases with the CC rate. This assumes unchanged wind fields. However, a common theory [e.g., Trenberth et al., 2003; Li and O'Gorman, 2020; Nie et al., 2018] suggests that, in addition to the thermodynamic contribution to enhanced rain rates, the higher water vapor content enables the release of more latent heat through condensation. This results in return to stronger large-scale (moisture) convergence due to amplified convective updrafts. Thus, the thermodynamic and dynamic contributions to higher precipitation extremes are intertwined. One of the main questions that remains, is whether the dynamical enhancement of moisture convergence is happening mainly in the cloud layer (due to increased updraft velocities) or whether the subcloud dynamics also play a role.

1.2.3. CONVECTIVE ORGANIZATION AND COLD POOLS

So far, we have maintained a rather isolated and monolithic perspective on extreme precipitation events. That the topic goes beyond single convective clouds or events can be seen when looking at Figure 1.6. It shows precipitation fields for two different situations arguably with convective events dominating the scene. In the first case (Figure 1.6a), we find many, scattered and rather small convective cells. In contrast to that the other situation (Figure 1.6b) is characterized by a relatively low number of events, but of considerably larger size. Moreover, the largest events seem to be clusters of hot-spots of precipitation. The distances between these clusters are rather long. One could say that they are more organized. The lack of an exact definition of when convective events are more
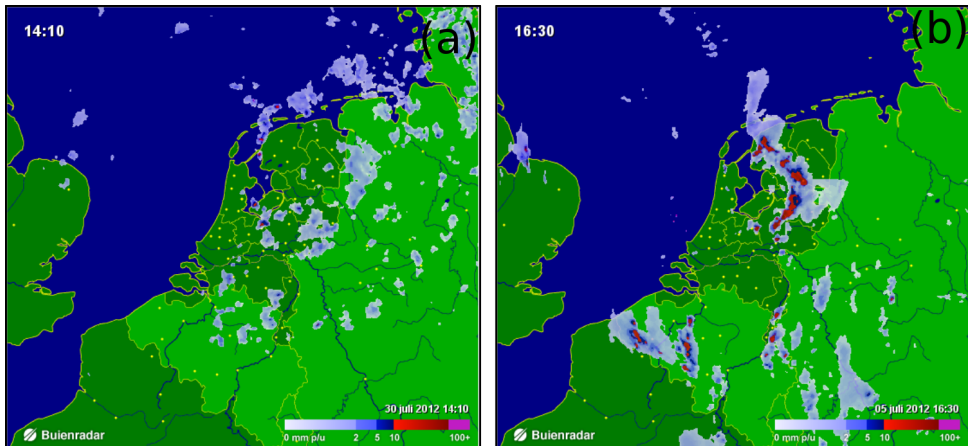
Figure 1.6: Two examples of rainfall events over the Netherlands area [Buienradar, 2021]. The situation in (b) shows larger and more organized convective cells than in (a).

or less organized has lead to a considerable number of different indices to determine the degree of convective organization. Usually, the definition of such an index follows the

particular questions and available data within a study. They range from simple nearest-neighbor distance based methods to more complex wavelet analysis [for an overview, see Brune et al., 2021]. However, most indices attempt to quantify, in some way, whether precipitation events are distributed as spatially random single cells or clustered into larger objects, such as mesoscale convective systems or squall lines. In this thesis, we refer to convective organization in a more qualitative way, following the above mentioned characteristics. Thus, the term "more organized" is used when we find a situation with a lower number of events that are larger in size.

Looking back at Figure 1.6b one might question what physical mechanism could lead to a more organized state. A phenomenon that is often brought in connection with the process of convective organization is cold pools. Figure 1.7a to d illustrates the typical life cycle of a cold pool according to Tompkins [2001]. A cold pool develops when part of the precipitating water evaporates in layers of unsaturated air. Since evaporation consumes energy the surrounding air mass cools and becomes negatively buoyant. The result is a cold-air blob that descends toward the surface. As soon as the cold pool reaches the surface, it has no other option than spreading horizontally. During this process, the cold pool remains relatively dry in the center whereas the edges are moist. The presence of wind shear forces the cold pool into an asymmetric shape. In its final stage the cold pool will flatten out and the temperature difference will eventually vanish. In its essence a cold pool is a density current that is driven by gravity and the associated temperature anomaly.
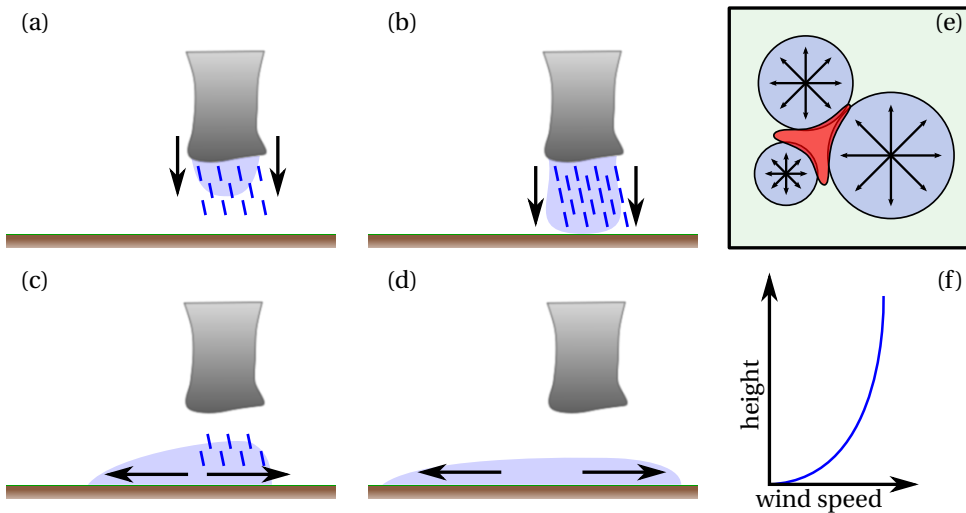
Figure 1.7: Illustration of the development of a cold pool. Evaporating rain drops cool surrounding air masses (a) which descend toward the surface (b). When the cold pool reaches the surface (c) it will spread horizontally and eventually flatten out (d). The presence of wind shear (f) causes the asymmetric shape of the cold pool. Multiple cold pools in different areas of the precipitation field will eventually collide (e). This creates areas of enhanced near-surface moisture convergence (red surface) which will be preferred locations for newly forming convective updrafts. Arrows indicate the primary direction of movement.

The described process of cold pool development imposes local dynamics that can be

crucial to the formation of deep convective clouds. For instance, it is known that cold pools, or collisions of multiple cold pools (Figure 1.7e), can trigger new convective updrafts [e.g., Hirt et al., 2020; Haerter et al., 2019]. The relatively dense air masses of cold pools cause a forced lifting of surrounding air at cold pool edges. This can be sufficient to overcome convective inhibition and trigger new convective updrafts. In the case of a collision of two or more cold pools the effect is even stronger since the horizontally enclosed air can only escape into the vertical direction. Moreover, it has been found that cold pool dynamics cause a redistribution of local near-surface moisture [Schlemmer and Hohenegger, 2016, 2014]. This is primarily due to the advection of moisture by horizontally spreading cold pools. Given that multiple cold pools exist in the domain this will lead to the accumulation of moisture in confined regions, so-called moist patches. However, how this affects the characteristics of precipitation extremes in the context of a warming atmosphere remains a largely unanswered question.

1.2.4. OTHER FACTORS

Besides the described processes, there are other factors that influence the formation of convective clouds and the amount of precipitation.

The processes inside a cloud, for example, the condensation of water vapor to droplets and their successive growth to precipitation size, happen on a microscopic scale. Here, we enter the field of cloud microphysics. While it is far beyond the scope of this thesis to mention and describe the relevant processes on this scale one can indirectly measure the impact of microphysics on rainfall amounts through a parameter called precipitation efficiency (ϵ). Generally spoken, ϵ represents the fraction of cloud droplets that reaches the surface as precipitation. It can further be decomposed into a conversion efficiency (α), which is the fraction of cloud condensate that is converted into precipitable water, and the fraction of rain drops that evaporate (β) before reaching the surface [Langhans et al., 2015; Muller and Takayabu, 2020]. More specifically,

$$\epsilon = \alpha(1 - \beta). \tag{1.15}$$

How ϵ precisely responds to climatic warming is still an open question. However, cloud-resolving simulations indicate that, under the assumption of radiative-convective equilibrium, there is only a minor dependency ($\approx 1\,\%\,\mathrm{K}^{-1}$) of ϵ on sea-surface temperature [Lutsko and Cronin, 2018]. Despite this rather robust change of ϵ with temperature, it should be noted that the absolute value depends on the applied microphysics scheme within the model. This given, the effect of how microphysics will respond to a warmer atmosphere is not a subject of analysis in this thesis.

While this thesis mainly studies the subcloud dynamics related to cold pools, dynamics in the cloud are important as well. These are connected to the instability of the atmosphere which can be measured by the convective available potential energy (CAPE). Larger values of CAPE are associated with a higher probability for convection formation and stronger updraft velocities. Accelerating updrafts can also draw in more moisture from the environment into the cloud core, producing higher rainfall rates [Loriaux et al., 2013]. Atmospheric stability is, thus, an important factor for convective precipitation.

1.3. An event-based approach

1.3.1. Definition of a precipitation event

What is the precise definition of a convective precipitation event? We have already explained the distinction of different precipitation types and how we define the term extreme. But, what exactly is an event? So far, we have used this term rather loosely but the simple illustration in Figure 1.8 will help to approach this question.
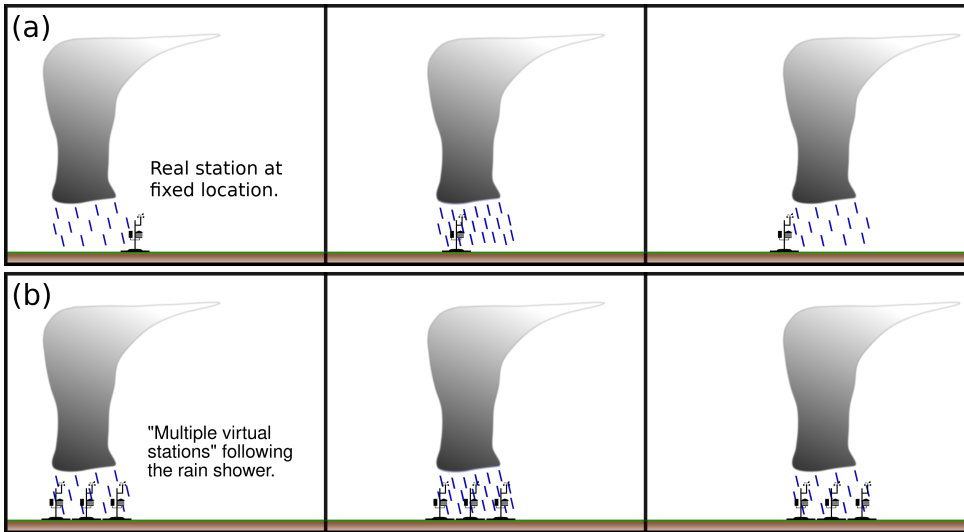
Figure 1.8: The difference between conventional station observations (a) and the Lagrangian approach (b).

Conventional station-based observations measure precipitation at a fixed point in space usually accumulated over fixed time intervals. Passing rain showers will only register at a station for the part of their life cycle during which they are above the respective location (Figure 1.8a). Thus, a station measurement is a composite of cloud properties like linear cloud size and rain intensity combined with the travel speed of a cloud. For instance, a relatively high-intensity convective cloud can produce rather low surface rain at a particular station if the large-scale wind velocity is high. Multiple stations are thus necessary to capture more data of the same shower. This approach will work better if there is a dense station network present meaning that there are many stations with short distances between each other and/or if the rain shower covers a large area and is long-lived. Nevertheless, station data can be aggregated to time series of precipitation fields even though at rather coarse resolution. If speaking of a precipitation event in this context, it is usually referred to as the footprint of a series of precipitating clouds over a certain area and time. This is, for example, the case for the two examples at the very beginning of this thesis.

The so-called Lagrangian approach offers a different perspective (Figure 1.8b). Instead of measuring passing showers from a fixed location, the observer moves with the precipitating cloud through space. One could think of multiple virtual stations that fol-

1

low a rain shower. This requires particular analysis methods and, especially, a suitable data type. Gridded data from radar observations or model output provide the spatial and temporal resolution to carry out such an analysis. The application of a specialized tracking method to this data type enables the analysis of complete individual precipitation tracks.

In this thesis, we refer to individual precipitation tracks or a specific time step within them when the term event is used. This approach allows to investigate specific properties of convective precipitation extremes.

1.3.2. TRACKING AND CHARACTERISTICS OF PRECIPITATION EVENTS

In order to examine the characteristics of extreme convective precipitation events a specialized clustering and tracking algorithm is required. The following paragraphs give the reader a general introduction to the applied technique and the specific aspects of events that are subject in this thesis. A more comprehensive description and chapter specific details can be found in the respective methods sections.
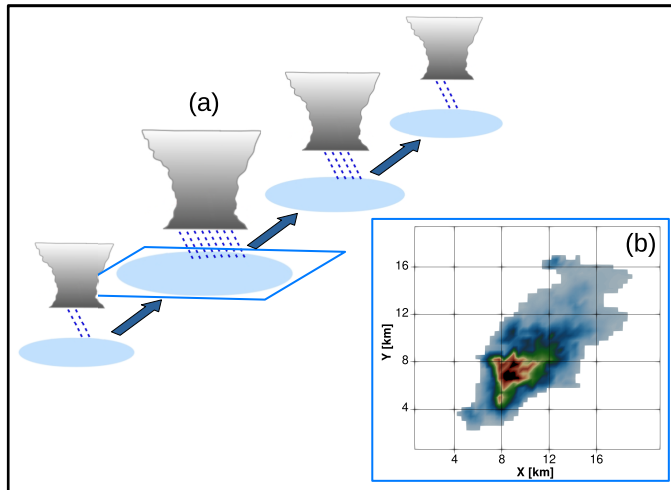
Figure 1.9: An idealized convective precipitation event at several stages of its life cycle (a). (b) shows a more realistic representation of a rain cell at the peak of the event (blue rectangle).

Consider a single track of convective precipitation through time and space. Figure 1.9a shows an idealized example at several stages. The goal of the tracking algorithm is to identify such tracks of precipitation as individual objects. Therefore, the first step is to apply a clustering routine that identifies continuous areas of precipitation and masks them by the assertion of unique labels. By overlaying the masks of subsequent time steps the identified rain cells can be connected in time. To account for the displacement of rain cells with the mean large-scale wind field this process is repeated multiple times. At each iteration an advection field is calculated from the known displacement distance of overlapping cells. This can then be used in the next iteration to advect rain cells and identify previously unknown connections between rain cells. This method is known as

iterative rain cell tracking [Moseley et al., 2013]. As a result of this, precipitation tracks are groups of rain cells that are connected in time.

At each time step, the precipitation field underneath the cloud, a rain cell, shows specific characteristics. We generally focus on two main properties the intensity and the area of the rain cell. While the area of a rain cell is a rather simple metric the intensity aspect is a more complex feature. Figure 1.9b shows a realistic example of a rain cell. It becomes clear that intensities vary considerably within the precipitation area. Depending on the objective in each chapter, we make use of different summary statistics to quantify the intensity characteristics of rain cells. First, the overall average intensity of a rain cell is used as a general indicator of its magnitude. Second, the peak (maximum) intensity gives the highest rain rate within a rain cell. Third, the product of area and average intensity represent the total amount of rain produced per unit time. Finally, to analyze the response of the spatial structure of extreme precipitation events to different conditions, we also produce spatial composites of conditionally sampled rain cells.

Lastly, we note that the described tracking method is fully applied in chapter 2. In this case, we focus on the moment in the life cycle of convective precipitation events with the highest intensity. In chapters 3 and 4 we only apply the clustering technique to identify individual rain cells. Besides tracking the life cycle of rain cells, the clustering/tracking algorithm can be also used to identify individual cold pools and confined regions of elevated moisture content. In chapter 4, we do this by applying the clustering method to low-level field anomalies of equivalent potential temperature (cold pool) and specific humidity (moist patches). As described before, the tracking part of the used software provides information about overlapping cells in between time steps. In the case of cold pools, this is particularly useful, since it enables the calculation of the areal growth rate, an estimate of the spreading speed.

1.3.3. DATA AND MODELING

This thesis follows a combined approach of observations and atmospheric modeling to study the characteristics of convective precipitation events (see Figure 1.10). Consequently, the choice of data sources and model follows the requirements governed by their high spatial and temporal variability.

In chapter 2, we use gridded rain radar observations with a continuous coverage of the Netherlands over a time period of nine years at a 5-minute time step and a spatial resolution of 1 km [Overeem et al., 2009b,a]. To connect the identified rain events with local conditions of temperature and moisture availability, station based observations of the dew point temperature at an hourly time step are used. Both data sets are provided by the Royal Netherlands Meteorological Institute (KNMI).

Despite the fact that high-resolution observations can be used to study dependencies within the present climate they are only available for short time intervals and, thus, do not provide enough data to draw definite conclusions about climate change impacts on extreme precipitation events. In chapters 3 and 4, we use an atmospheric model to examine these effects. Global and regional climate models do not resolve the spatial and/or temporal scales of convective precipitation. On the other end of the spectrum, large eddy simulation models are designed to run at very high horizontal and vertical resolutions, typically on the scale of a few tens to a few hundred meters. Here, we apply the
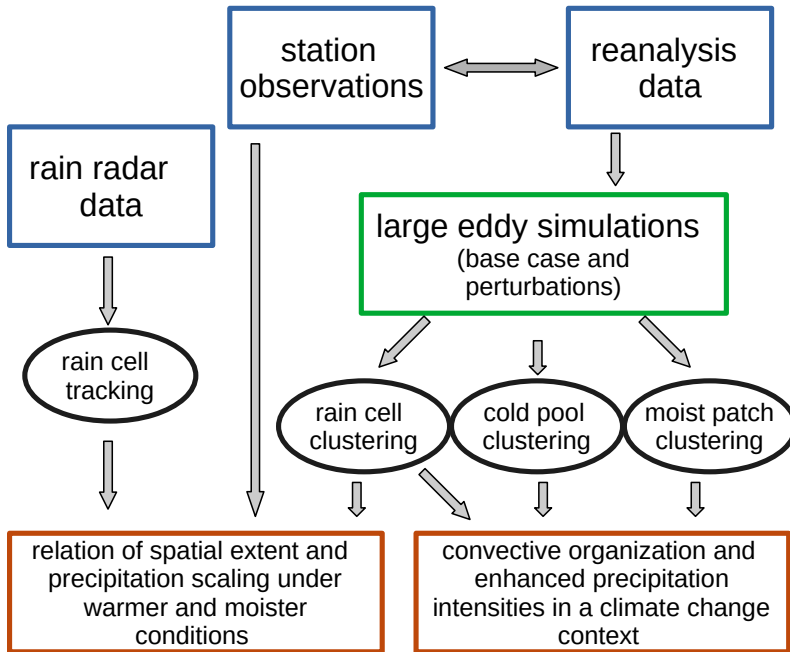
Figure 1.10: The various data sources, methods/model and objectives of this thesis.

Dutch Atmospheric Large Eddy Simulation (DALES) model in the framework of an idealized, yet realistically forced composite case [Loriaux et al., 2017]. The setup configuration originates from an observation-based selection of heavy summertime precipitation events [Lenderink et al., 2017]. Atmospheric profiles for the initiation and time-varying large-scale forcing of the model are taken from a reanalysis product since observations do not provide high enough resolution in this context. The reanalysis data itself is based on global reanalysis data which is downscaled with a regional climate model to a resolution of 12 km [Meijgaard et al., 2012]. The resulting composite case, representative for typical conditions for heavy summertime precipitation events, is perturbed in various ways to mimic climate change.

1.4. AIM AND OUTLINE

In the beginning of this chapter, we highlighted the potential for a high socio-economic impact that stems from the natural hazard of convective precipitation extremes. This renders research on this topic highly relevant but due to the small-scale nature of the phenomenon it is particularly challenging and pushes the envelope of currently available observations and models.

The aim of this thesis is to expand our knowledge about convective precipitation extremes on the local scale and the involved processes. More specifically, we focus on three major questions which will be elaborated on in the following paragraphs.

1. *What is the relation between size and intensity of convective precipitation extremes in a warmer and moister atmosphere?*

   To this date, little work has been done to answer the question about how spatial properties of convective events relate to their intensity. In chapter 2, we use radar observations in combination with a tracking routine to examine the properties of convective extreme events. We carry out a detailed analysis of their size and intensity over a wide range of dew point temperature. Additionally, we perform a sensitivity analysis on how the spatial extent of convective events influences the scaling of precipitation amounts with increased dew point temperature. In chapter 3, we use a LES model to simulate heavy summertime convective precipitation extremes at midlatitudes. We use this controlled setup to further investigate the question how size and intensity of convective rainfall events relate. Additionally, in chapters 2 and 3, we look at the spatial distribution of intensities within rain cells to investigate whether there is a connection between cell size, intensity and a redistribution of rainfall amounts within the cell.

2. *What is the role of cold pools for the size and intensity of convective events?*

   Cold pools are known to impact the initiation and organization of convection. Thus, our journey to an answer to this question starts in chapter 3, where we analyze how the precipitation field as a whole responds to warmer conditions. We achieve this by looking at the distribution of rain cell size at different stages in the LES experiments. In chapter 4, where a similar LES setup as in chapter 3 is used, we move on to investigate how cold pools respond to warmer and moister conditions and how this correlates with rain cell intensity. We characterize cold pools by their volume, which we define as the product of size and average equivalent potential temperature anomaly, and the areal growth rate. In a next step, we examine how cold pool activity relates to the advection of near-surface moisture into confined regions and how this potentially feeds back to precipitation amounts.

3. *How are convective precipitation extremes affected by a broader set of climate perturbations?*

   While the experiments in chapter 3 are more mimicking the variations within the present-day climate (constant RH and lapse rate; see Lenderink et al. [2017]), the experiments in chapter 4 probe a larger range of future climate conditions. For instance, it is known that relative humidity is rather constant over ocean areas, with slight increases possible, whereas over land it is more likely to decrease [O'Gorman and Muller, 2010]. Besides that, warming of the atmosphere is expected to vary with height [Tett et al., 1996; Bony et al., 2006]. Lastly, extreme precipitation events are often found together with a strong large-scale vertical motion [Lenderink et al., 2017]. In chapter 4, we use a LES model to simulate a variety of climate perturbations and investigate how convective precipitation extremes respond to these conditions. We therefore perform several groups of experiments which are characterized by changes in relative humidity and stability of the atmosphere. In a separate group of simulations, we investigate the effects of increased large-scale moisture

1

convergence due to stronger large-scale lifting under warmer and moister conditions.

2

THE SPATIAL EXTENT OF RAINFALL EVENTS AND ITS RELATION TO PRECIPITATION SCALING

Observations show that subdaily precipitation extremes increase with dew point temperature at a rate exceeding the Clausius-Clapeyron (CC) relation. The understanding of this so-called super CC-scaling is still incomplete, and observations of convective cell properties could provide important information. Here the size and intensity of rain cells are investigated by using a tracking of rainfall events in high-resolution radar data. Higher intensities are accompanied by larger rainfall areas. However, whereas small rain cells mainly follow CC-scaling, larger cells display super CC behavior. Even more, for dew point exceeding $15\,°C$, the rain cell size has to increase in order to sustain super CC-scaling and a remarked increase in rain cell area is found. Our results imply that the source area of moisture, the cloud size, and the degree of mesoscale organization play key roles in the context of a warming climate.

2.1. INTRODUCTION

A warmer atmosphere can hold more water. As a consequence rainfall amounts increase and precipitation extremes intensify. This relation is generally referred to as precipitation scaling. More precisely, the scaling rate is the fractional rate of change of rainfall with respect to temperature or moisture availability. Global climate models, for instance, predict that extremes of daily precipitation sums, on average, increase up to 6-7% per degree warming [Allen and Ingram, 2002; Tebaldi et al., 2006; Pall et al., 2007; Kharin et al., 2013]. This is in line with the Clausius-Clapeyron (CC) equation, which describes the water holding capacity of the atmosphere with respect to temperature [Trenberth et al., 2003]. However, focusing on much smaller-scale convective extremes, it has become evident that on subdaily and, in particular, subhourly time scales scaling rates can exceed the CC relation (called super CC-scaling) even by up to the factor of 2 (called 2CC scaling) [Lenderink and van Meijgaard, 2008; Loriaux et al., 2013; Mishra et al., 2012; Lenderink et al., 2011]. These results have been obtained by deriving the dependency of high percentiles (usually the 99th) of the rainfall distribution on surface temperature or dew point temperature from present-day short-term variability. This is usually done by a binning approach, in which precipitation intensities are paired to coincident near-surface (dew point) temperatures [Westra et al., 2014].

The cause of super CC-scaling of convective precipitation extremes on short time scales is still subject of ongoing research. Statistical effects related to the duration and type of precipitation events complicate the computation of scaling rates and their physical interpretation [Haerter and Berg, 2009; Molnar et al., 2015; Wasko et al., 2015; Wasko and Sharma, 2015]. Besides these statistical effects, dynamical effects are generally considered to play an important role [Westra et al., 2014; Trenberth et al., 2003]. According to this hypothesis, the release of latent heat due to condensation in a cloud updraft increases buoyancy and leads to stronger cloud dynamics [Loriaux et al., 2013]. This in turn causes enhanced moisture convergence, possibly from a larger area. This positive feedback may lead to a 2CC behavior [Loriaux et al., 2013; Lenderink et al., 2017]. Recent results with a convection-resolving model revealed that the organization of convective cloud systems into larger clusters plays an important role to explain super CC-scaling [Moseley et al., 2016]. Conversely, from surface observations it was found that with increasing temperature the moisture within a storm burst is redistributed toward the center inducing higher rainfall intensities but smaller spatial extent [Wasko et al., 2016].

The listed aspects bring out the multidimensionality of the scaling relationship between precipitation extremes and surface temperature and moisture. In situ observations contributed substantially to the detection and exploration of super CC-scaling. However, to further expand our knowledge about convective precipitation extremes in this context, we need to look at finer details such as the area and intensity of individual showers. Rain radar data provide a high spatial and temporal resolution. At the same time, following precipitation events through time and space creates a perspective that makes it possible to investigate their characteristics throughout the whole life cycle [Moseley et al., 2013] and allows an easier interpretation in terms of physical processes. Here we exploit the potential of a high-resolution rain radar data set using rain cell tracking and investigate the spatial properties and intensity of precipitation events and its relation to surface moisture. Therefore, we use dew point temperature T_d because it

is a direct measure of humidity and gives more robust scaling results than temperature [Lenderink et al., 2011; Lenderink and van Meijgaard, 2010]. More specifically, we focus on the following two questions: (1) what is the relation between rainfall area/level of organization and precipitation intensity and (2) how do these factors change with the surface dew point temperature.

2.2. Data and Methods

We make use of two data sets provided by the Royal Netherlands Meteorological Institute (KNMI). First, a time series of radar-based precipitation fields spanning the years from 2008 to 2016 with a time step of 5 min and a spatial resolution of 1 km [Overeem et al., 2009b,a]. For this study we select a region within a buffer of approximately 10 km around the land surface of the Netherlands (see Figure S2.1). The domain covers an area of 57 000 km^2 (roughly 280 km by 200 km). Second, we use T_d records from in situ data of the KNMI automatic weather stations (AWSs) network. For the same period as the radar data hourly time series from 35 AWSs are available (see Figure S2.1 in the supporting information). The majority of stations are free from missing values. To study the characteristics of summertime convective precipitation, we only select the months from April to September.

Using the conceptual framework of Moseley et al. [2013], we developed an algorithm to track precipitation events in rain radar data. Figure 2.1 shows a simplified illustration of how a track or event – we use these terms as synonyms – is defined. In the first step a clustering routine detects rain cells in each time step, defined as a continuous area of grid points exceeding an intensity threshold of 0.6 mm h^{-1}. At this point we determine the rain cell properties such as area, maximum intensity, and the location of the intensity weighted center of mass which is used for all distance calculations. Then a linking procedure checks for (partly) overlapping cells in subsequent time steps. The results are used to estimate how fast rain cells move between time steps. The velocities of cells that do not split or merge are averaged over a grid of 150 km by 180 km (see Figure S2.1) and are used as an approximation of the large-scale cloud advection velocity. An iterative procedure takes this velocity to advect the rain cells, rechecks for new overlaps, and updates the velocity fields. After six iterations the procedure converges, and the final links between rain cells are established to derive the rain cell tracks. There are two types of tracks: without and with splitting and/or merging of rain cells. To see an example of the first possibility, the so-called solitary track, we have to ignore the green haloed cells in Figure 2.1. If all cells were present, we would have a more complex version which involves splitting and merging of rain cells. We consider both track types in this chapter equally, unless denoted otherwise. Furthermore, we define the peak of an event as the cell with the highest maximum intensity (yellow frame in Figure 2.1). The size of a cell is represented by the square root of its area ($\sqrt{A}$).

To be taken into account for further analysis, tracks must initiate and end in the selected radar data region without crossing the boundaries. Two additional filters are applied. First, all tracks of shorter duration than three time steps (15 min) are omitted to limit the analysis to events with a complete life cycle (start, peak, and decay). Second, the distance between the first and last cell of a track must be at least 5 km. This removes

2
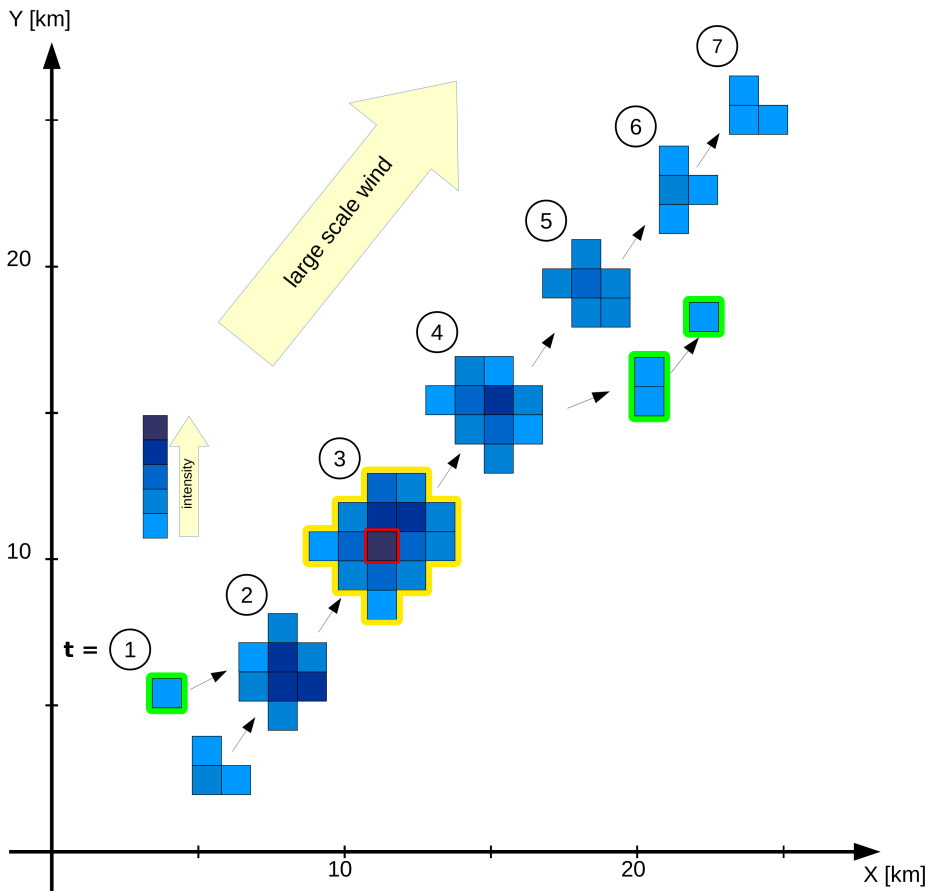
Figure 2.1: Idealized version of a rain cell track showing how rain cells are advected with the large-scale wind during the life cycle ($t = 1, 2, \ldots, 7$). Splitting and/or merging of rain cells can happen at any time. Without those cells (green halo) our example would be a so-called solitary track. The yellow framed cell holds the maximum intensity (red grid point). Note that this is a composite showing all rain cells (time steps) of a track in one image. To simplify the illustration, we avoided to draw overlapping cells.

stationary tracks which are most likely the result of pseudorain caused by ground echoes (compare Figures S2.2 and S2.3). Events which pass these filters are connected to a T_d record measured at the closest station (with data available) 3 h (± 30 min) before and at the location of the peak of the event.

To relate dew point temperature with precipitation event area and intensity, we make use of binning methods with either constant bin widths or bin sizes. In the first case we divide the T_d range into discrete equally spaced intervals. For the latter, the bin breaks are chosen to achieve approximately equal numbers of events within each bin. This procedure leads to varying bin widths, but, in contrast to a constant bin width, it allows us to include events which occur at very high T_d.

2.3. RESULTS

2.3.1. RAIN CELL TRACKING AND CELL CHARACTERISTICS

The rain cell tracking reveals a total number of approximately 1.52×10^5 tracks (with $T_d > 5\,°C$). Of these, 99 % can be connected with a T_d record from an AWS within a range of less than 35 km. The average distance is 16.4 km. Most of the events (62 %) are solitary tracks. However, the percentage of solitary tracks steadily decreases with event duration and falls below 50 % for events of 35 min and longer (Figure S2.4). This reflects the increasing probability of splitting and merging of rain cells for longer events. We observe a similar relation concerning the event size at the peak of the event (Figure S2.5). More than 50 % of the events with a size of 5 km include splitting and/or merging, and this fraction increases for larger events. So larger events have longer durations and are more likely to be affected by splitting and merging.

Generally, the highest intensities are concentrated on a small fraction of the area of a rain cell. Figure 2.2a shows a rain cell composite for the 1000 strongest precipitating events (at peak of the event) with dew points between 13 °C and 20 °C. A steep decrease of precipitation intensity with increasing distance from the center is clearly seen. A large fraction of the rain cell area has rather low precipitation intensities. The intensity profile (radial average) in Figure 2.2b further quantifies the sharp peak with a strong decline of precipitation intensity with distance to the center. Results for a subsample of events with lower humidity – between 5 °C and 11 °C dew point temperature – display a very similar dependency with distance to the center.

However, comparing the low-humidity sample with the high-humidity sample, we see much higher intensities throughout most of the rain cell in the latter. In addition to the increase in peak intensity, there is a coinciding increase in the area with high intensities. In other words, there are higher intensities within the same radius in the high-humidity sample without a clear sign of redistribution of intensities toward the center as suggested by Wasko et al. [2016]. The similarity between the distribution of intensity in the rain cell for low and high dew points motivates us to only look at the peak intensities of the event as relative changes in the peak intensity are representative for the overall intensity changes within the rain cell.

2
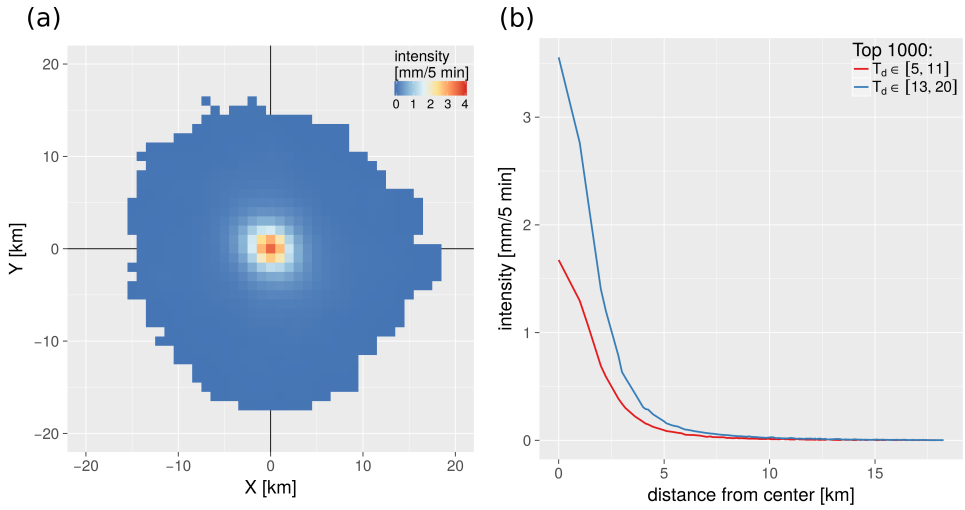
Figure 2.2: (a) Composite of the 1000 strongest precipitating events between 13 °C and 20 °C at the time of the event peak. The averaging was done centering cells on the intensity weighted center of mass (x=0, y=0). Grid points that are covered by less than 1 % of the selected events are omitted. (b) Intensities steeply decrease with growing distance from the center. The blue curve shows a radially averaged profile for the composite in Figure 2.2a. The red curve represents a corresponding subsample for T_d between 5 °C and 11 °C.

2.3.2. PRECIPITATION AREA, INTENSITY, AND T_d

We first investigate the distribution of event size as a function of T_d at the peak of the event. Figure 2.3a shows that most of the events are rather small in size, more than 50 % are typically below 4 km, and approximately 10 % exceed 7 km. The distribution of cell size depends on the dew point temperature. At lower humidity, below dew points of 10 °C, we see a weak increase in event size for the highest percentile of the distribution. However, the size distribution changes much more clearly in the high-humidity range, at T_d above 15 °C, where we see a progressive tendency toward bigger events.

Cell sizes conditioned on the rainfall intensity show a similar behavior. In Figure 2.3b we show the median cell size for a selection of events with different intensities. A rapid increase in cell size is visible for T_d beyond 15 °C to 16 °C, but the increase in the low dew point range (below 10 °C) is now almost nonexistent. In addition, it is found that cells with stronger intensity are larger. For instance, the selection of the 10 % most intense events has a size of on average 6 km or more, almost double the average size of the lowest 50 % intensity events. This correlation is by no means perfect. If there would be a perfect correlation of cell size and cell intensity (that is, a unique monotonic function exists to relate size to intensity and vice versa), then the 80th percentile of the cell size (Figure 2.3a) should match exactly with the median of area of the events selected between the 70th and 90th intensity percentile (p80, in Figure 2.3b). So, event size and peak intensity are clearly positively correlated, but there is no unique relation between cell size and cell intensity.

(a)

(b)
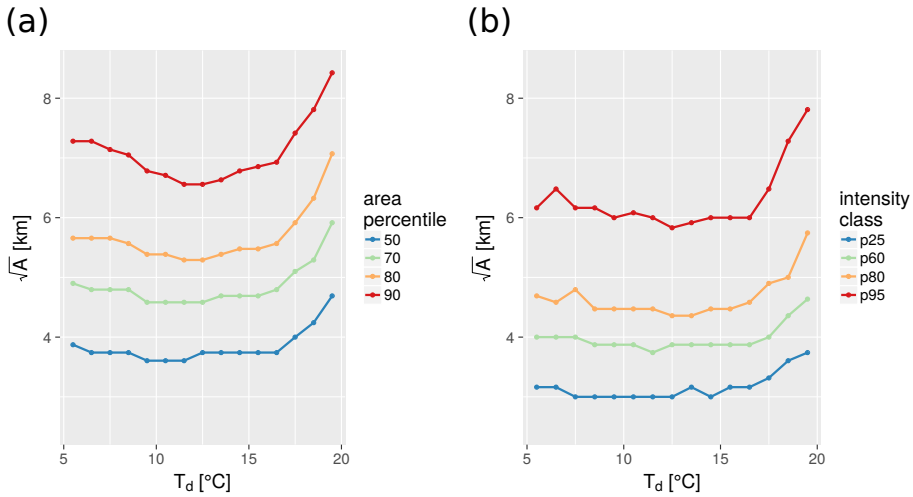
Figure 2.3: Cell size distribution (square root of the cell area at event peak) with respect to dew point temperature (derived using an equal bin width of 1 °C). (a) Percentiles of the distribution of cell size and (b) cell size conditioned on the intensity, computed by plotting the median of the area of events with intensity below the 50th percentile (p25), between the 50th and 70th percentiles (p60), the 70th and 90th percentiles (p80), and above the 90th percentile (p95).

2.3.3. EXTREME PRECIPITATION SCALING AND SENSITIVITY TO EVENT SIZE

Having found that on average bigger cells produce higher peak intensities, and that the event size distribution shifts toward bigger events beyond 15 °C dew point temperature, we now focus on the role of events size to explain precipitation intensity scaling. Figure 2.4a shows the scaling of precipitation intensity with T_d for the 90th, 95th, and 97.5th percentiles (calculated per bin). In this case, the bins are constructed to contain approximately 1000 events.

Scaling rates are close to or exceed the CC relation for dew points above 8 °C (Figure 2.4a). In general, scaling rates increase with dew point temperature and with increasing percentile. The scaling behavior of the 90th and 95th percentiles is rather similar; up to 15 °C intensities follow an approximately constant rate of 7 % °C^{-1} (CC). For higher T_d we see an exceedance of the CC rate. The 97.5th percentile appears to have a slightly higher scaling rate on a wider T_d range.

The finding of a scaling rate close to the CC relation, or slightly above, up to dew points of 15 °C, contradicts the results of previous studies which found a robust double CC scaling for (sub)hourly precipitation in the Netherlands across a much larger dew point range [Lenderink and van Meijgaard, 2008; Loriaux et al., 2013]. However, we have seen that there is a clear link between intensity and event size (see Figure 2.3b). Therefore, we split the event catalog using a size threshold of 5 km and repeat the binning procedure. This 5 km threshold divides the data approximately into 70 % small-area events and 30 % large-area events (see Figure 2.3a). The large-area events not only have higher intensities than the small-area events but also higher scaling rates (Figures 2.4b
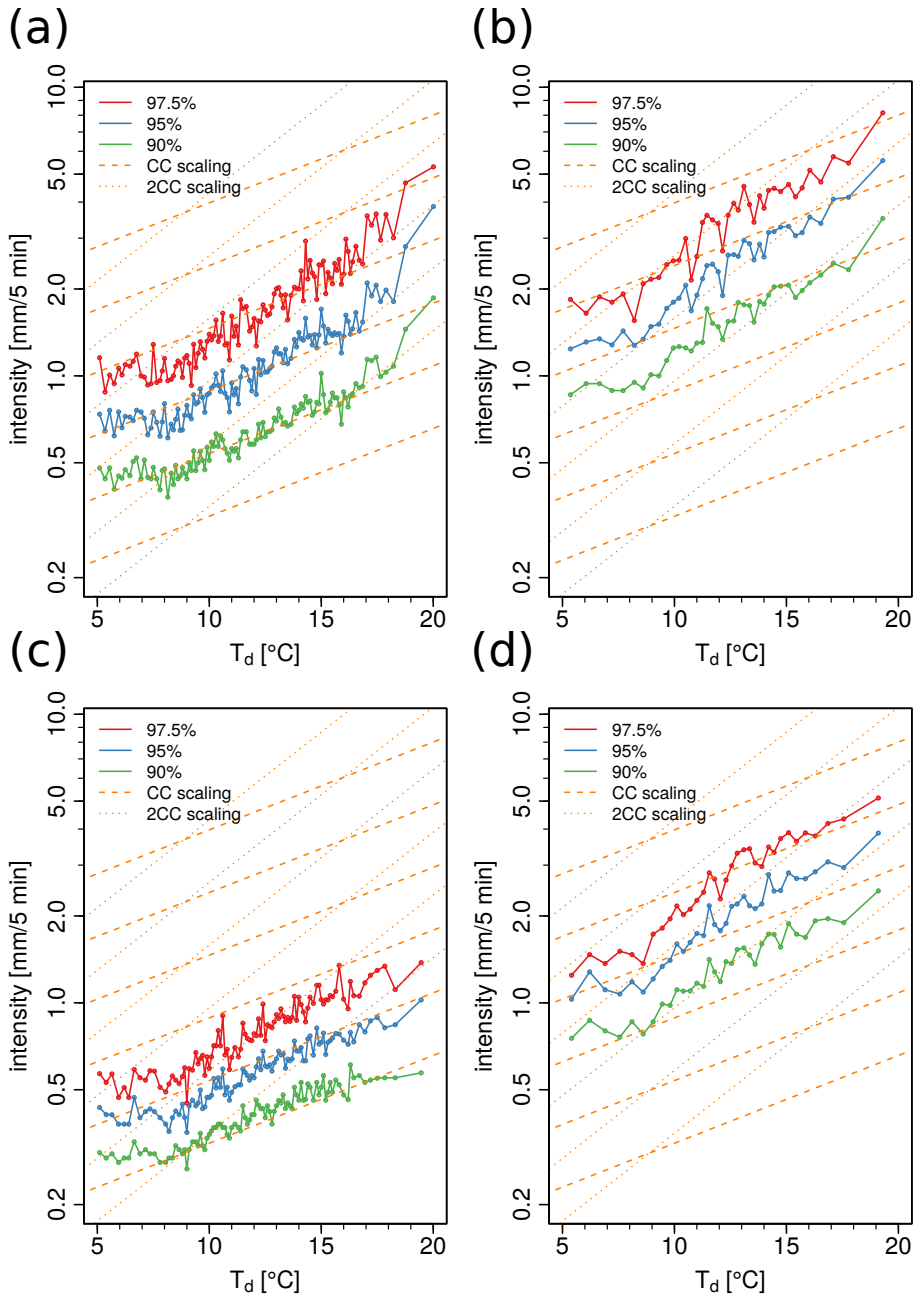
Figure 2.4: Extreme precipitation scaling with respect to dew point temperature. (a) The 90th, 95th, and 97.5th percentiles for all events. (b) The same as Figure 2.4a but for events with $\sqrt{A} > 5$ km. (c) The scaling for events with $\sqrt{A} \leq 5$ km only. (d) A subset of events with $\sqrt{A} \geq 5$ km and $\sqrt{A} \leq 9$ km. Dashed lines indicate CC scaling, and dotted lines indicate 2CC scaling.

and 2.4c). Whereas for the small-area events precipitation extremes scale with rates close to CC over the whole dew point temperature range, large-area events clearly exceed the CC scaling rate.

Using a higher event size threshold, for instance 7 km (Figure S2.6), confirms the increased scaling rate for bigger events. The diagnosis of a scaling rate close to the CC relation for smaller event sizes tends to be robust even if we omit very small events (Figure S2.7). Specifically looking at solitary tracks, which are dominant below the applied area thresholds, yields a scaling close to the CC relation, but with a slightly higher rate for the most extreme events (Figure S2.8). In contrast to that, splitting and merging tracks have higher extremes that increase stronger with dew point temperature (Figure S2.9).

Considering that larger events have higher scaling rates, it is natural to question the role of the increase in event size beyond 15 °C to 16 °C dew point temperature. In order to investigate this we limited event size to a minimum of 5 km and a maximum of 9 km (Figure 2.4d). While in the intermediate dew point temperature regime up to 15 °C, scaling rates still exceed the CC rate (close to 2CC), at higher dew point temperatures the scaling rate falls back to the CC rate. This fallback to CC rate also clearly shows up using a larger dew point bin size (compare Figures S2.10a and S2.10b). Thus, the results are robust and independent of the chosen bin size. We conclude that the inclusion of the biggest events is needed in order to maintain an enhanced scaling rate at the highest dew point temperatures. So a super CC-scaling at the highest dew point temperature range can only be sustained if there is an accompanying increase in event size.

To quantify the dependence of the intensity scaling on event size further, we calculate a scaling coefficient (fractional rate of change of precipitation intensity per degree T_d) $\alpha = \log(r)/(\overline{T}_{d,1} - \overline{T}_{d,2})$ where $r = P_{i,T_{d,1}}/P_{i,T_{d,2}}$ [Moseley et al., 2013]. For that, we take events from two T_d ranges: 5 °C to 11 °C (2) and 13 °C to 20 °C (1). $\overline{T}_d$ is the corresponding group mean of dew point temperature and P_{i,T_d} the respective i^{th} intensity percentile with $i \in \{90, 95\}$.

Figure 2.5 summarizes the results of this analysis. Including all events in the two T_d ranges, α varies between 7.8 % °C^{-1} and 9.9 % °C^{-1}. For the area constrained analysis with $\sqrt{A} \leq 5$ km and $\sqrt{A} \leq 6$ km we obtain smaller scaling rates between 6.7 % °C^{-1} and 9 % °C^{-1}. Setting a minimum area threshold, scaling rates are mostly beyond 11 % °C^{-1}. For both percentiles α steadily increases with respect to the area threshold and reaches values around 13 % °C^{-1} for $\sqrt{A} \geq 8$ km. Note that we excluded the 97.5th percentile as there are successively decreasing sample sizes at higher area thresholds. A reliable estimation of this quantile cannot be guaranteed under this circumstance. So we clearly see a scaling close to the CC relation if the event size is constrained to 5 km to 6 km, whereas bigger events scale close to 11 % to 13 % per degree.

2.4. Conclusions and discussion

In this chapter we analyzed the characteristics of showers at the time of their peak intensity using a tracking of rain cells in nine years of rain radar data of summertime conditions over the Netherlands. Using dew point temperature, we investigated how event size (defined as the square root of cell area at the time of peak intensity) and intensity depend on near-surface moisture as measured by the 2 m dew point temperature. In

2
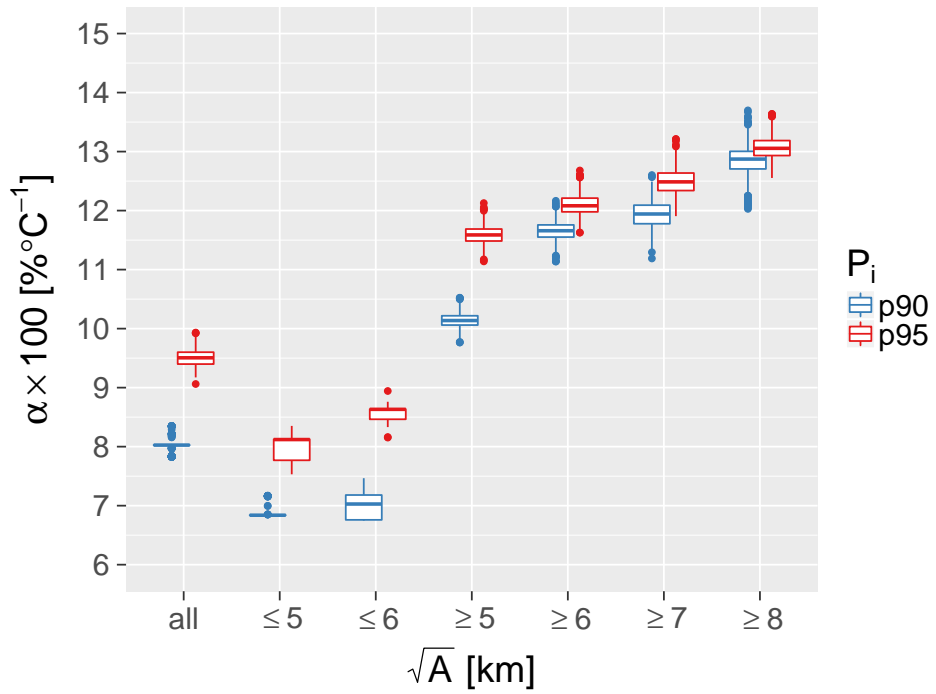
Figure 2.5: The scaling parameter α for different percentiles and area-constrained subsamples. Uncertainties are estimated repeating the calculation 1000 times while randomly dropping 10 % of the events.

general, the results show that event peak intensity and cell area are clearly related; in a statistical average stronger events are larger events. Additionally, event sizes increase remarkably at dew point temperatures above 15 celsius.

The scaling of peak intensities with dew point temperature is strongly tied to the rain cell area and only larger events can display the super CC-scaling. Events below an area threshold of 5 km to 6 km display a dependency of peak intensities following a rate close to the CC relation, predicting $6\,\%\,°C^{-1}$ to $7\,\%\,°C^{-1}$. Conversely, events which exceed the minimum event size show a scaling of peak intensities of approximately 11 % to 13 % per degree.

Beyond a dew point temperature of 15 °C, super CC-scaling can only be sustained with a corresponding rapid increase in rain cell size. This has been found by omitting the largest events from the sample, which causes the scaling rate to fall back to CC rate above 15 °C dew point. It is interesting to note that at approximately the same dew point temperature range strong feedbacks caused by latent heat come into play [Lenderink et al., 2017]. This feedback leads (i) to strongly buoyant cloud updrafts and very deep convective clouds and (ii) enhanced large-scale moisture convergence due to enhanced large-scale vertical velocities. Finally, we mention a possible link to the critical behavior as seen in tropical convection, where beyond a critical value of integrated water vapor content a steep increase in cloud size and intensity is observed [Neelin et al., 2009].

The finding that intensities increase rather uniformly over the rain cell area with dew point temperature, and the cell size increase, indicates that the shower sources moisture from a larger area. A super CC-scaling of rainfall rates within the cell must be supported by a moisture transport also in excess of the CC relation, and assuming the same source area the transport would increase only at the CC rate [Westra et al., 2014]. We note, however, that the whole life cycle of convective cells/events must be considered to be able to give a more definite answer. Nevertheless, we do not find any evidence of a redistribution of moisture toward the center at the cost of the outer region of the rainfall area as found by Wasko et al. [2016].

In summary, our results reveal that the cloud cell size plays a crucial role in the mechanism behind the super CC-scaling of convective clouds. Larger events are more likely a product of merging and splitting of rain cells, and this probability further increases at dew point temperatures above 15 °C where event sizes increase rather steeply. This suggests that the organization of convective showers into larger clusters is of importance in the context of super CC-scaling, in accordance with a recent modeling study [Moseley et al., 2016]. In contrast, super CC behavior was not obtained in simulations of rather weakly organized convection [Loriaux et al., 2017] and also not found for solitary tracks [Moseley et al., 2016]. Therefore, we think that understanding the mesoscale atmospheric and cloud dynamics is crucial to be able to better predict and understand future changes in convective storms: their intensity, their size, heterogeneity, and level of aggregation [e.g., Guinard et al., 2014; Pendergrass et al., 2016; Westra et al., 2014].

ACKNOWLEDGMENTS

2

APPENDIX

DATA AVAILABILITY

A data set with the event catalog is available at http://doi.org/10.4121/uuid:a00ab095-fb31-44e8-a77c-587063a5839e.
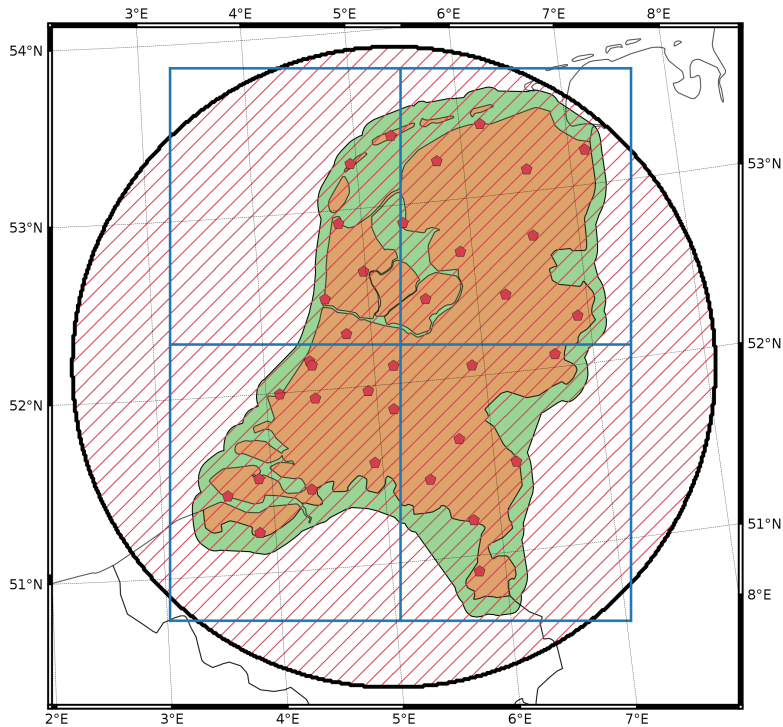
FIGURES

Figure S2.1: Data coverage of the rain radar data set (red shaded area). For the rain cell tracking, a buffer of approximately 10 km (green) around the land surface of the Netherlands (orange) is selected. Red symbols mark the locations of the 35 automatic weather stations where hourly measurements of dew point temperature are available. During the rain cell tracking the algorithm calculates how fast rain cells move between time steps. The velocities are averaged within the blue boxes.
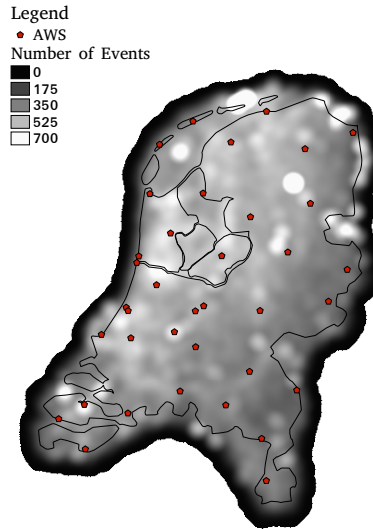
Figure S2.2: The number of tracks initiating at a certain location. Only tracks with a complete life cycle, a duration of at least 3 time steps (15 min) are included.
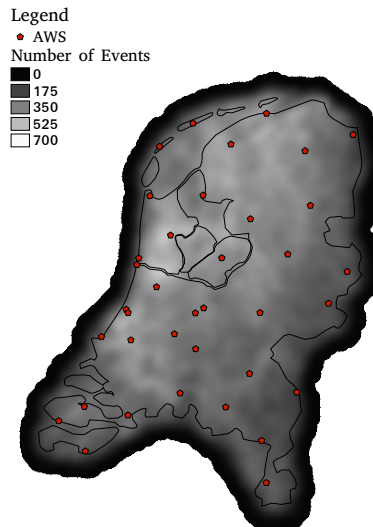
Figure S2.3: The number of tracks initiating at a certain location. In contrast to the previous figure, tracks with a path length of less than 5 km are removed. This filter excludes quasi stationary tracks which are most likely the result of ground echoes (see white areas in previous figure).
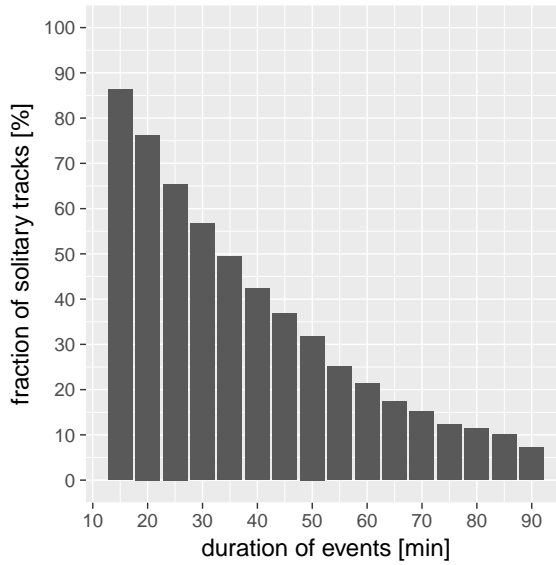
Figure S2.4: The fraction of solitary tracks (no splitting or merging cells), with respect to event duration.
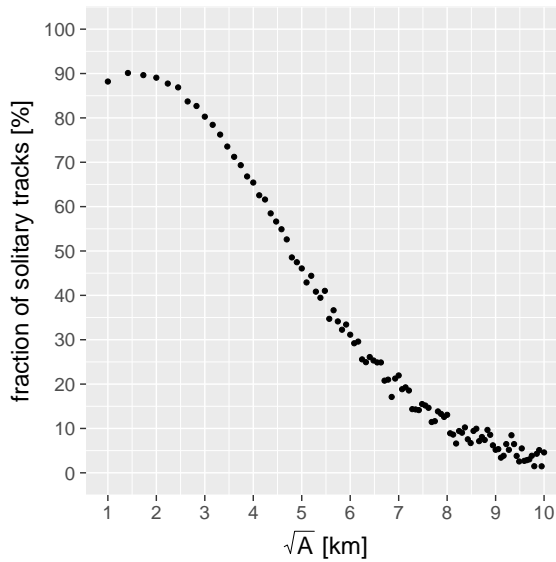
Figure S2.5: The fraction of solitary tracks (no splitting or merging cells), with respect to the square root of the area at event peak.

2
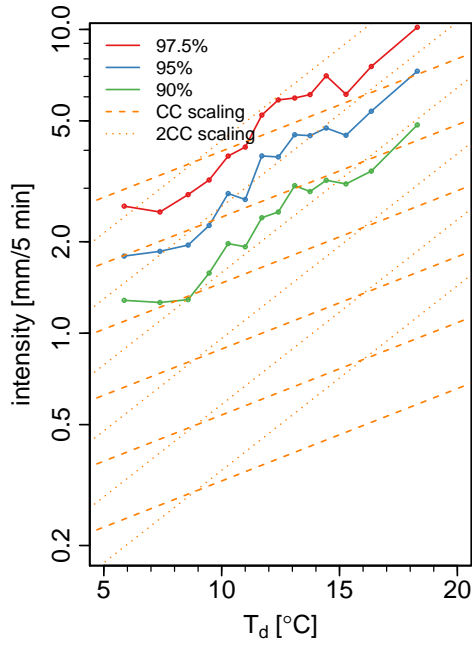
Figure S2.6: Precipitation scaling diagram for events exceeding a square root of the area of 7 km.
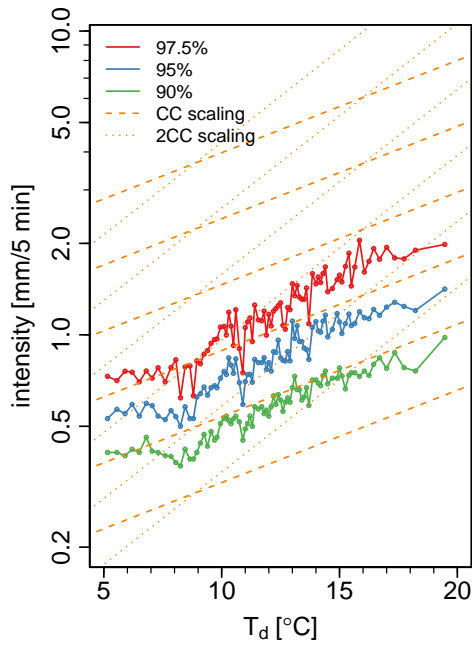
Figure S2.7: Precipitation scaling diagram for events with a square root of the area between 3 km and 6 km
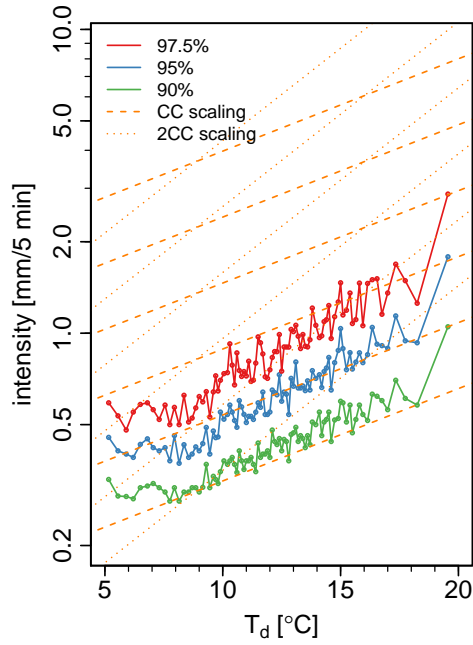
Figure S2.8: Precipitation scaling diagram for solitary tracks only.
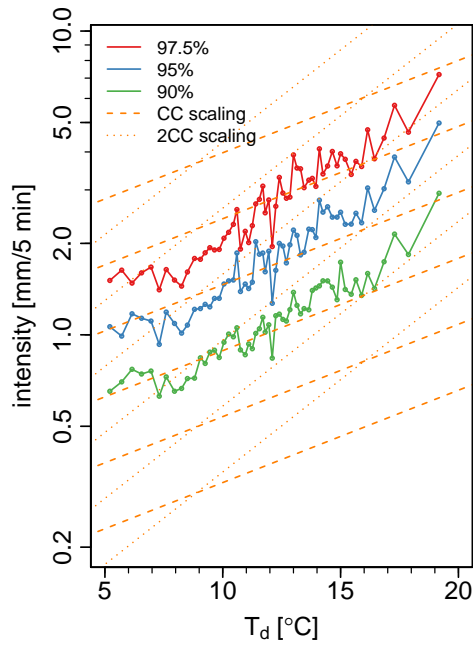
Figure S2.9: Precipitation scaling diagram for events that include splitting and merging of rain cells.

2
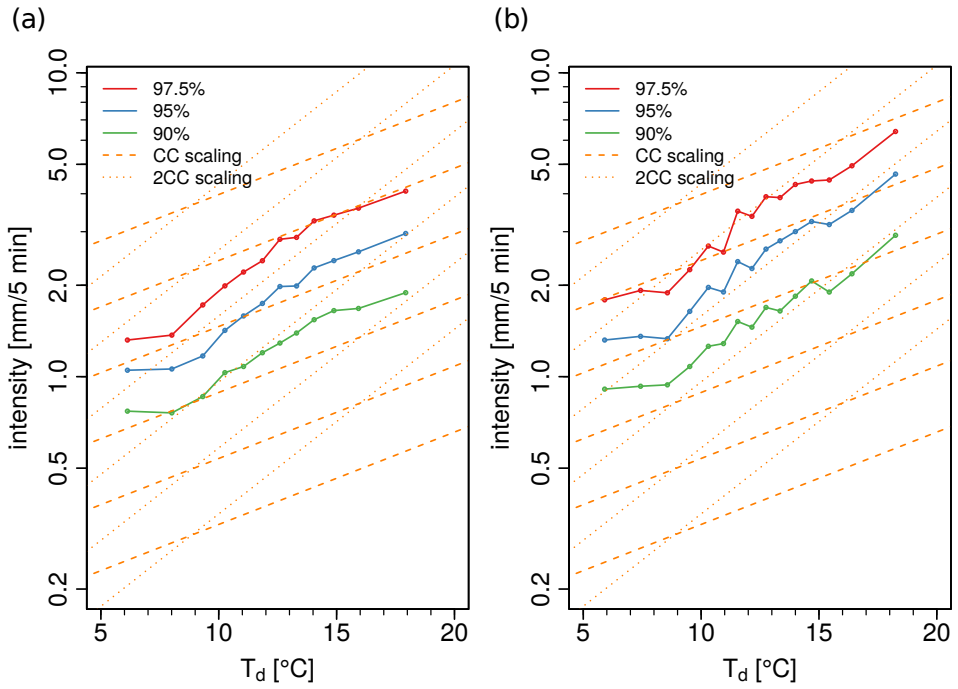
Figure S2.10: Precipitation scaling diagrams for events with a square root of the area between 5 km and 8 km (a) and for all events larger than 5 km (b). The dew point temperature bin size is set to 2500 events to yield a stronger smoothing. The difference between the two plots shows that including larger events is prerequisite to sustain super CC-scaling beyond 15 °C. Otherwise, scaling falls back to CC rate.

3

RESPONSE OF EXTREME PRECIPITATING CELL STRUCTURES TO ATMOSPHERIC WARMING

With increasing temperatures, it is likely that precipitation extremes increase as well. While, on larger spatial and longer temporal scales, the amplification of rainfall extremes often follows the Clausius-Clapeyron relation, it has been shown that local short-term convective precipitation extremes may well exceed the Clausius-Clapeyron rate of around $6.5\,\%\,K^{-1}$. Most studies on this topic have focused exclusively on the intensity aspect, while only few have examined (with contradictory results) how warmer and moister conditions modulate the spatial characteristics of convective precipitation extremes and how these connect to increased intensities. Here we study this relation by using a large eddy simulation (LES) model. We simulate one diurnal cycle of heavy convective precipitation activity based on a realistic observation-based strongly forced case setup. Systematically perturbed initial conditions of temperature and specific humidity enable an examination of the response of intensities and spatial characteristics of the precipitation field over an $8\,°C$ dew point temperature range. We find that warmer and moister conditions result in an overall increase of both intensities and spatial extent of individual rain cells. Colder conditions favor the development of many but smaller rain cells. Under warmer conditions, we find a reduced number of individual cells, but their size significantly grows along with an increase of intensities over a large part of a rain cell. Combined, these factors lead to larger and more intense rain cells that can produce up to almost 20 % more rain per degree warming and therefore have a large impact.

3.1. INTRODUCTION

How do the characteristics of rainfall extremes change with a warming atmosphere? This question has multiple dimensions and can be tackled from different angles.

The most obvious aspect is the intensity. Usually and already for several decades [Fischer and Knutti, 2016], changes in the intensity of rainfall extremes have been attributed to the increase in the water holding capacity of the atmosphere, as dictated by the Clausius-Clapeyron (CC) relation. Indeed, a number of global modeling studies have confirmed that changes in daily precipitation extremes scale with the CC rate – $7\,\%\,K^{-1}$ – when aggregated over large areas [Allen and Ingram, 2002; Tebaldi et al., 2006; Pall et al., 2007], although substantial deviations have been observed over the tropical and subtropical oceans due to large-scale dynamical feedbacks [Pfahl et al., 2017]. At the other end of the spectrum of precipitation extremes, at small spatial and temporal scales, the CC relation is also playing a key role in understanding its behavior in response to warming. Station observations show that hourly and subhourly precipitation extremes can display dependencies on surface (dew point) temperature up to two times the CC relation [Lenderink and van Meijgaard, 2008; Lenderink et al., 2011; Mishra et al., 2012; Loriaux et al., 2013]. This enhanced CC scaling of local short-term rainfall extremes can be largely attributed to convective precipitation events [Berg et al., 2013; Moseley et al., 2013]. A common hypothesis is that amplified latent heat release through higher temperatures and moister conditions leads to increased buoyancy and hence to more vigorous convective updrafts [Trenberth et al., 2003]. This potentially leads to stronger moisture fluxes into convective updrafts at the cloud base but also laterally from the cloud environment [Loriaux et al., 2013; Lenderink et al., 2017; Singleton and Toumi, 2013]. Recent research shows that the subcloud moisture convergence increases with surface temperature in convection resolving model simulations of extreme convective precipitation [Moseley et al., 2016; Haerter et al., 2017]. And even more, the spatial extent of these areas of moisture divergence and convergence increases with temperature. Therefore, this provides evidence that convective events collect moisture from larger areas with increasing temperature and moisture availability.

Thinking straightforwardly, this could imply that the spatial properties of the precipitation footprint of convective events vary with temperature and moisture availability. However, there are few studies dedicated to this aspect, and the results are contradictory. Wasko et al. [2016], for instance, show that storms in Australia become more concentrated to the center and smaller in spatial extent. A similar analysis by Li et al. [2018] based on station observations and regional climate models arrives at the same conclusion. By analysing rain radar data covering an eastern Mediterranean region, Peleg et al. [2018] also found increases in the intensity at the center of the convective cells with surface temperature but unchanged to small decreases in the area of convective cells. So all of these studies point at a redistribution of rain intensity toward the center of the convective cell at the expense of the spatial extent. However, in contrast to these findings Lochbihler et al. [2017] find that convective cells grow in size at higher dew point temperatures and that this growth accelerates beyond $17\,°C$ to $18\,°C$ dew point temperature. For the same region, Lenderink et al. [2017] obtain from station records of hourly precipitation that rainfall events at higher dew point temperatures blanket more stations than at lower dew point temperatures. In addition, a recent modeling study with a con-

vection permitting model showed a largely increased rain volume for the most intense convective systems that mainly resulted from an increase in spatial extent [Prein et al., 2017].

These contradictory findings show that the precise mechanisms of how warming influences the properties of convective rain cells remain still highly uncertain. There is reasonable consensus that intensities of convective rainfall events increase at a rate close to or beyond the CC rate [Westra et al., 2014]. However, whether convective rain cells respond at a rate close to twice the CC rate, as suggested by surface observations in a number of regions, is still unclear. As an aside, we note here that part of the contradictory results may well be related to the fact that some of these studies use dew point temperature, a direct measure of near surface absolute humidity, whereas it is still more common to use temperature as the scaling variable [Wasko et al., 2018; Lenderink et al., 2018]. For the spatial aspects, results are even more unclear, and both reductions in spatial extent with (dew point) temperature as well as increases are reported.

Therefore, we will here study these characteristics in idealized experiments using a high-resolution large eddy simulation (LES) model. In particular, we aim to answer the following questions: (i) How does precipitation intensity and area respond to warming, (ii) what is the relation between intensity and cloud rain cell size, and (iii) are there indications of a redistribution of cell intensities towards the center at the expense of cell size or rain intensities at the rain cell borders.

More specifically, we conduct simulations of a diurnal cycle with typical conditions for heavy convective precipitation in the Netherlands. This case setup is characterized by substantial time varying forcing from the surface as well as the large-scale circulation which forces the system out of equilibrium [Loriaux et al., 2017]. Therefore, our simulations are fundamentally different from quasi-equilibrium simulations performed, for instance, for the tropics, in radiative-convective-equilibrium [e.g. Romps, 2011; Muller et al., 2011]. By systematically varying the initial state of temperature and humidity, we investigate the temporal evolution of surface precipitation and the response of the rainfall field to increasing temperatures and humidity in a range from 12 °C to 18 °C dew point.

3.2. METHODS

3.2.1. LES SETUP

Simulations are carried out using the Dutch Atmospheric LES (DALES) model [version 4.1; Heus et al., 2010; Böing et al., 2012]. DALES is a LES model which uses the anelastic approximation with a turbulent kinetic energy equation for subgrid transports. The source code is distributed under the GNU General Public License v3.0 and available online (https://github.com/dalesteam/dales). A single-moment cloud microphysics parameterization scheme [Grabowski, 1998; Böing et al., 2012] is used and the radiative cooling and surface fluxes (Figure S3.1) are prescribed. For a full description of the model equations, we refer to the above-mentioned publications and the source code repository. The complete model setup is available from Data Set D3.1.

The experimental setup follows the approach developed in Loriaux et al. [2017], specifically designed to produce a simple but yet realistic forcing for convective situations.

Based on a catalog of rainfall events in the Netherlands from the past 20 years [Lenderink et al., 2017], we create a composite of approximately 300 days with heavy hourly precipitation in the summer season (April to September) in the afternoon hours (1200 to 2000 CET). Our selection is further constrained to the top 20% most intense events at dew point temperatures above 14 °C. Detailed statistics of the event catalog can be found in Table 1 of Lenderink et al. [2017]. On average, these events take place at a surface dew point temperature of 16 °C and have a peak intensity of 15 mm h^{-1}.

As in Loriaux et al. [2017], we retrieved the necessary data for the initialization, the large-scale forcing, and the surface fluxes from a concatenation of hindcasts of the regional climate model RACMO [Meijgaard et al., 2012] at a resolution of 12 km, initialized, and forced with ERA-interim reanalysis data [Dee et al., 2011].
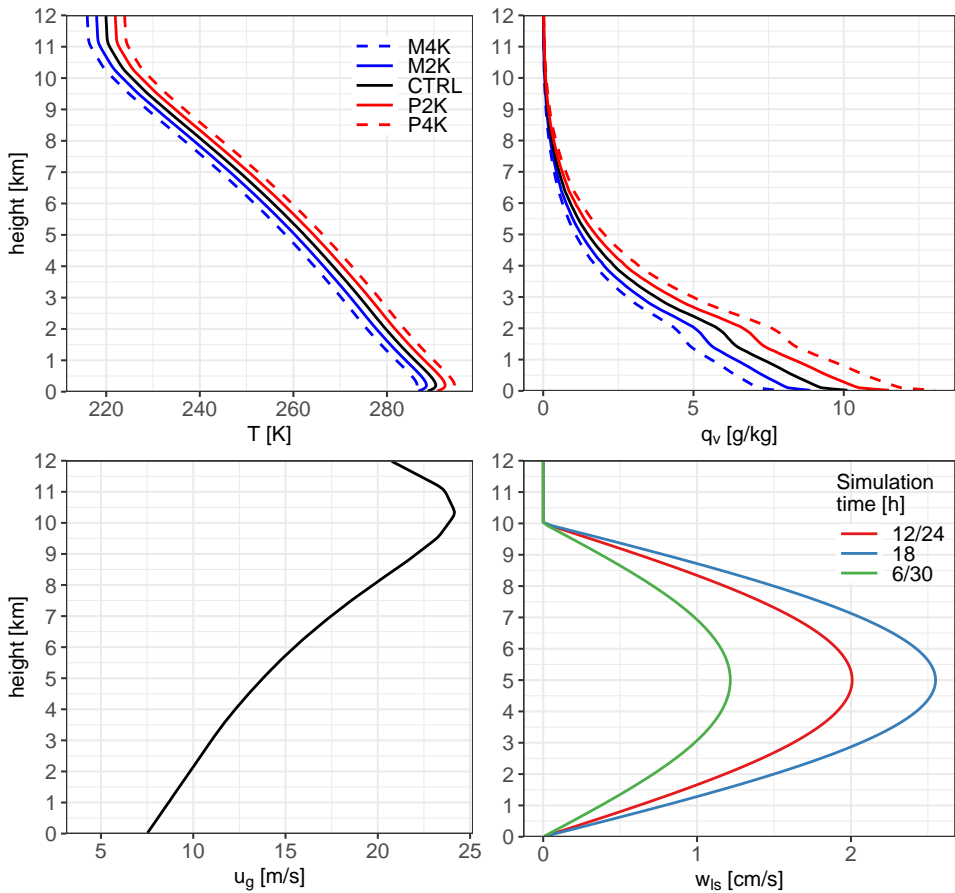
Figure 3.1: Initial profiles for temperature T and water vapor specific humidity q_v. The geostrophic wind forcing u_g is the same for all experiments and constant in time. The idealized large-scale vertical velocity w_{ls} varies in time but is symmetric to the time step at 18 hours of simulation. Here, vertical profiles of w_{ls} are shown for 6 (30), 12 (24) and 18 hours of simulation. For a time-height plot of w_{ls}, see Figure S3.2.

Initial profiles of temperature and humidity (Figure 3.1) are a composite of the 0400

CET conditions at the station with the highest rainfall amounts of each event. The model is forced with time variable (0400 to 0400 CET of the following day) surface sensible and latent heat fluxes (see Figure S3.1). In this case, the averaging was done over all stations within a radius of 70 km around the event location. Furthermore, a geostrophic wind profile (Figure 3.1) is calculated in a similar manner as the surface fluxes. Because the derived geostrophic wind profile has only little temporal variability, we applied it as a constant forcing in time to DALES. We calculated the wind speed from u and v components before averaging and serve it to DALES as the u component only.

Most extreme convective events in the Netherlands occur with considerable synoptic-scale convergence, inducing a large-scale upward vertical velocity (omega) that humidifies and destabilizes the atmosphere [Lenderink et al., 2017; Loriaux et al., 2017]. This forcing is imposed in DALES through a large-scale vertical velocity [Loriaux et al., 2017] and varies in time and with height as shown in Figure S3.2. The lower right panel in Figure 3.1 shows the omega forcing (w_{ls}) at three example time steps of the simulation. In contrast to Loriaux et al. [2017], the resulting average omega field from the selection of cases has been idealized. This has been done to filter out noise in time and height which would complicate the analysis of the results (see Lenderink et al. [2017]; Loriaux et al. [2017] for some typical results of these averaged omega fields for a typical selection of events).

Based on the control (CTRL), run we simulate four additional experiments with perturbed initial conditions. The initial profile for temperature is increased (decreased) uniformly in steps of 2 K. Keeping relative humidity constant, which is (to first order) representative in the context of climate change [Attema et al., 2014], results in an increase (decrease) of the initial specific humidity profile. We term these perturbed simulations M4K (−4 K), M2K (−2 K), P2K (+2 K) and P4K (+4 K), according to the temperature deviation relative to the control simulation.

Simulations are carried out on a domain with an extent of 192 km × 192 km in the horizontal directions and approximately 21 km in the vertical dimension. A sponge layer is used at levels above 13 km which is well beyond the maximum cloud top height. A horizontal grid spacing of 200 m makes 960 × 960 grid points. The vertical grid, 240 levels, is nonequidistant with a level thickness of around 40 m near the surface and up to 150 m in the highest model levels. To provide ample time for convective organization, we stretch out the simulation day by a factor of 1.5 [Moseley et al., 2016; Haerter et al., 2017]. This decision is motivated by two aspects. First, the model is initiated with a nearly homogeneous atmosphere in horizontal directions and turbulence needs time to build up (spin-up) during the first hours of simulation. This delays the organization of convection, and testing has shown that the highest precipitation rates are reached way beyond the peak of the large-scale forcing in the normal day setup. By giving the system more time to organize, the timing of the highest precipitation rates shifts toward the peak of the large-scale convergence and surface forcing, which is closer to observed cases [Lenderink et al., 2017]. The second aspect is that this approach increases the data output and enables more robust statistics at a reasonable additional computational cost. We stop the simulations after 30 hours since we are interested in the daytime part where the large-scale forcings are strongest.

3.2.2. PRECIPITATION STATISTICS AND RAIN CELL CLUSTERING

The simulations produce output of surface precipitation at a time step of 1 min with the full horizontal resolution. To reduce the data amount and to ease the rain cell clustering later on, we coarse-grain the data to a grid spacing of 400 m. This also drastically reduces the number of very small rain cells with low intensities. We also apply a minimum threshold of $0.6\,\mathrm{mm\,h^{-1}}$. Smaller values are set to zero. In the remainder of this study, we will use the following notation, which is, for means of simplicity, given here for a single time step.

We define the total area with surface precipitation exceeding the threshold as A. The nondimensional area fraction with rain is

$$a = A/A_D, \tag{3.1}$$

where A_D is area of the full domain (192 km × 192 km). Note that we use the lower case letters for nondimensional quantities. The total rain rate over the domain – called rain yield hereafter and denoted by P – is the rain rate aggregated over the domain and normalized by A_D. We also consider the rain rate P_r conditional on the precipitation area. They are trivially related by

$$P = aP_r. \tag{3.2}$$

At each time step, the surface precipitation output is clustered to continuous areas with rain, from now on referred to as rain cells. The algorithm to cluster is identical to Lochbihler et al. [2017]. Accordingly, neighboring grid points with precipitation above the threshold belong to the same cell. Diagonal adjacency is not allowed. The number of cells is given by N. Each cell i has different properties given by its size A_i and its mean intensity $P_{i,r}$, which is the sum of the rain rates over all grid points divided by the number of grid points belonging to the cell. The linear size L_i of a cell is defined as the linear length given by the square root of the cell area

$$L_i = \sqrt{A_i}. \tag{3.3}$$

Whenever we use the term size of a cell, we refer to this linear length.

We also define the cell-aggregated rain rate, which is given by

$$P_{i,car} \equiv A_i P_{i,r} = L_i^2 P_{i,r}, \tag{3.4}$$

which is just the total rain produced by a cell per time unit. From an impact point of view, this cell-aggregated rain rate is important when integrated over the life time of a cell as it quantifies the total amount of rain produced by a rain cell. Also, it is dynamically important as it relates to the net rate of latent heat release produced by the cell.

The domain-averaged rain yield and rain rate can be expressed in terms of the cell statistics as

$$P = \frac{\sum_{i=1}^{N} A_i P_{i,r}}{A_D}, \tag{3.5}$$

$$P_r = \frac{\sum_{i=1}^{N} A_i P_{i,r}}{A}, \tag{3.6}$$

where A is simply the sum of the area of all cells

$$A = \sum_{i=1}^{N} A_i, \tag{3.7}$$

so that the rain rate P_r is the cell-area-weighted mean of the individual cell rain rates $P_{i,r}$.

Besides the statistics of all rain cells, we also investigate the statistical properties of cells of a certain size or exceeding a certain size. In that case, the number of cells does not equal the total number of cells N but is constrained to a subset of cells satisfying a condition for L_i. For instance, a conditional precipitation rate $P_{L_1-L_2,r}$ for cells with a size between L_1 and L_2, is computed from

$$P_{L_1-L_2,r} = \frac{\sum_{i=1}^{N} I_{L_1-L_2}(i)P_{i,r}}{\sum_{i=1}^{N} I_{L_1-L_2}(i)}, \tag{3.8}$$

where the indicator function $I_{L_1-L_2}(i)$ has been introduced and is defined as

$$\begin{aligned} I_{L_1-L_2}(i) &= 1 \text{ if } L_1 < L_i \leq L_2 \\ &= 0 \text{ otherwise.} \end{aligned} \tag{3.9}$$

3.3. RESULTS

3.3.1. TEMPORAL EVOLUTION OF SURFACE PRECIPITATION

Figure 3.2 shows time series of the precipitation area fraction a, the precipitation yield P, and the precipitation rate P_r. All experiments show a similar temporal evolution for all quantities. However, we first focus on the CTRL run to illustrate the interplay between these different measures.

After the onset of rainfall, at hour 11, the area fraction rapidly increases and peaks approximately one and a half hours later. During the following one and a half hours, the area fraction drops by more than a half to about 6 % and, with a slight relief, remains at this level for about 4 h. Following this, it reaches an even lower level for the remainder of the simulation.

A similarly phased evolution is visible in the time series of precipitation yield but with even sharper transitions from lower to higher values. The precipitation yield reaches a first maximum value around hour 12 and a second peak 5 h later. In between, there is a period of 2 h with less activity. The area fraction considerably differs between these two time windows. This indicates that the precipitation field as a whole undergoes significant changes.

At this point we introduce the definition of two phases of precipitation activity with distinct spatial characteristics as well as intensities (gray areas in Figure 3.2). We note that these two phases are by no means discrete stages of the simulation but rather part of a continuous transformation of precipitation characteristics. By choosing time intervals of the same length, we obtain two comparable samples to robustly probe the precipitation field at different stages during the process of convective organization. Phase I is the time frame around the first peak of area fraction. This phase is also characterized

3
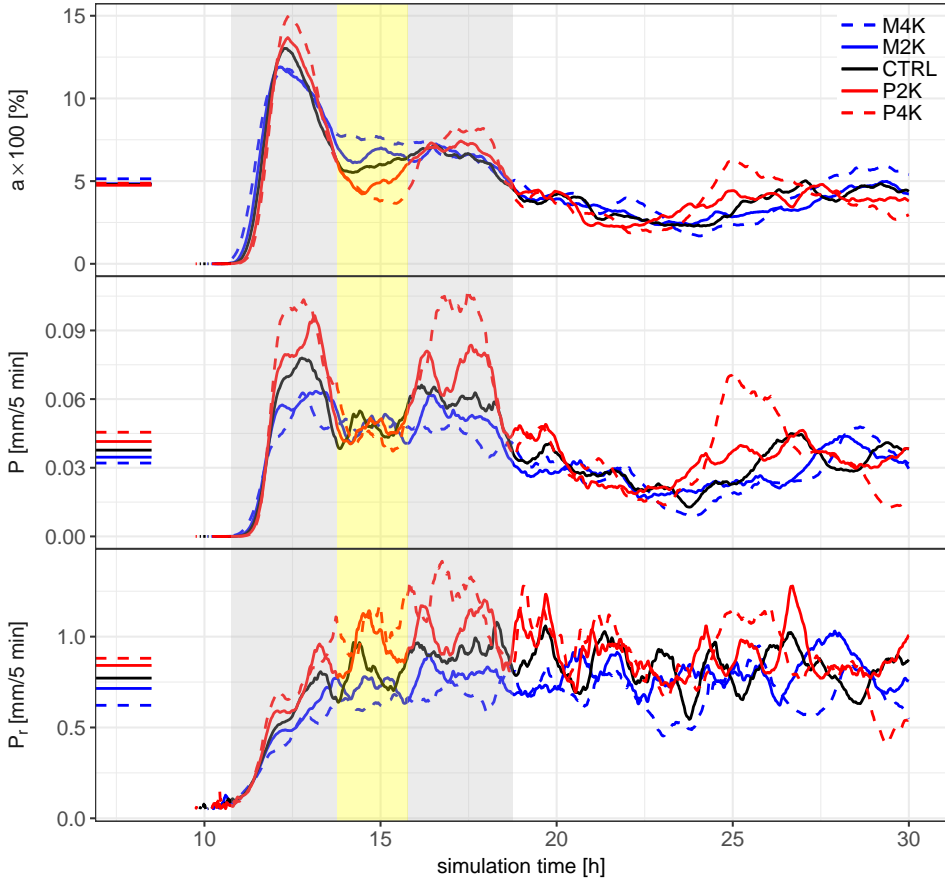
Figure 3.2: Time series of domain averaged precipitation measures for all experiments. From top to bottom: the precipitation area fraction a, the precipitation yield P and the precipitation rate P_r. The gray areas mark the selected time frames for phases I and II (see text for explanation). The yellow area is the transition phase. The line segments on the y-axis mark the time average of each quantity.

by a sequence of relatively high values of precipitation yield. In a similar way, we define phase II as the time window which covers the second plateau of precipitation yield. Both phases have a length of 3 h and cover the two peaks of the precipitation yield. We call the time span between the two phases the transition phase (yellow area in Figure 3.2).

The area fraction in Phase II is considerably lower than in Phase I. Since the level of precipitation yield in phase II is comparable to phase I, the precipitation rate must compensate this. Indeed, the precipitation rate continuously increases roughly until the end of phase II. Afterward, the precipitation rate shows no clear tendency but larger fluctuations than before. Thus, the precipitation field in phase I is characterized by a relatively large precipitation area with relatively low rainfall intensities. During the transition to phase II, the precipitation area decreases, but the rain rate increases.

The temporal evolution of all three precipitation characteristics is similar for all experiments, but there are also substantial differences. The area fraction in phase I peaks at higher values in the warmer runs. In contrast to that, the area fraction in the transition phase is higher for colder experiments. All runs reach approximately the same area fraction in phase II. The precipitation yield shows a similar systematic behavior. From the coldest to the warmest experiment, the yield gradually increases in both phases. The precipitation rate correspondingly increases until the end of phase II in all experiments with the highest/lowest values in the P4K/M4K run.

There are two major characteristics which deserve additional attention in this context. First, the timing of the two phases is nearly the same across all experiments. This is aided by the fact that we used perturbations in temperature while keeping the relative humidity constant, which implies an unchanged dew point depression and therefore approximately the same lifting level of condensation. Moreover, all experiments share the same prescribed large-scale forcing for convergence and surface fluxes (see Figure S3.2 and Figure S3.1). Consequently, the destabilization of the atmosphere and initiation of convection as well as the point where saturation and finally precipitation sets in are similarly timed between the experiments. The same factors play a crucial role for the timing of phase II. Due to the moisture removal through rain in phase I, it takes time until the surface latent heat flux and moisture input through large-scale convergence (which scales roughly with the CC relation, see Figure S3.3) replenish this deficit. Simultaneously, the surface heat flux and large-scale convergence counteracts the stabilizing effect of convection from phase I: While the surface forcing causes a warming in the lower levels, the large-scale convergence which is strongest in the mid-troposphere (see Figure S3.2) induces cooling (see Figure S3.4). This aspect is closely connected to the second peculiarity: the occurrence of the transition phase in between the two active phases. In warmer runs, we observe a higher precipitation area fraction, rate, and yield in phase I. Thus, the stabilizing effect is stronger (see Figure S3.4) and affects a larger part of the domain which then leads to a lower area fraction in the transition phase before phase II sets in.

Up to the end of phase II, at hour 18, convective activity shows a systematic response to the warmer and moister atmospheric conditions. These are imposed by the initial conditions but also by the dependency of the large-scale moisture convergence which roughly follows the CC relation [Loriaux et al., 2017]. After phase II, the response is less systematic, and because of large temporal variations, it is also more difficult to compare

the different runs. Part of this may be related to the fact that the surface forcing is small after 18 hours (see Figure S3.1), which limits further destabilization of the atmosphere. Further on, we will therefore focus on the two active phases I and II because they show a clearly systematic behavior and they are still relatively strongly influenced by the initial conditions and the large-scale forcing (Figures S3.1 and S3.2).

3.3.2. SPATIAL CHARACTERISTICS OF THE PRECIPITATION FIELD

A qualitative overview of how the spatial variability in the precipitation field depends on temperature and humidity can be achieved by looking at snapshots at different stages of the simulation. In Figure 3.3 we show the rainfall field at the center of the time windows of phases I and II for the M4K, CTRL, and P4K runs. Phase I is characterized by many, more or less regularly distributed rain cells of small spatial extent. Five hours later in phase II, most of the smaller rainfall areas have been replaced by or grown into considerably larger cells. Moreover, rain cells become larger and more intense under warmer and moister conditions in both phases.
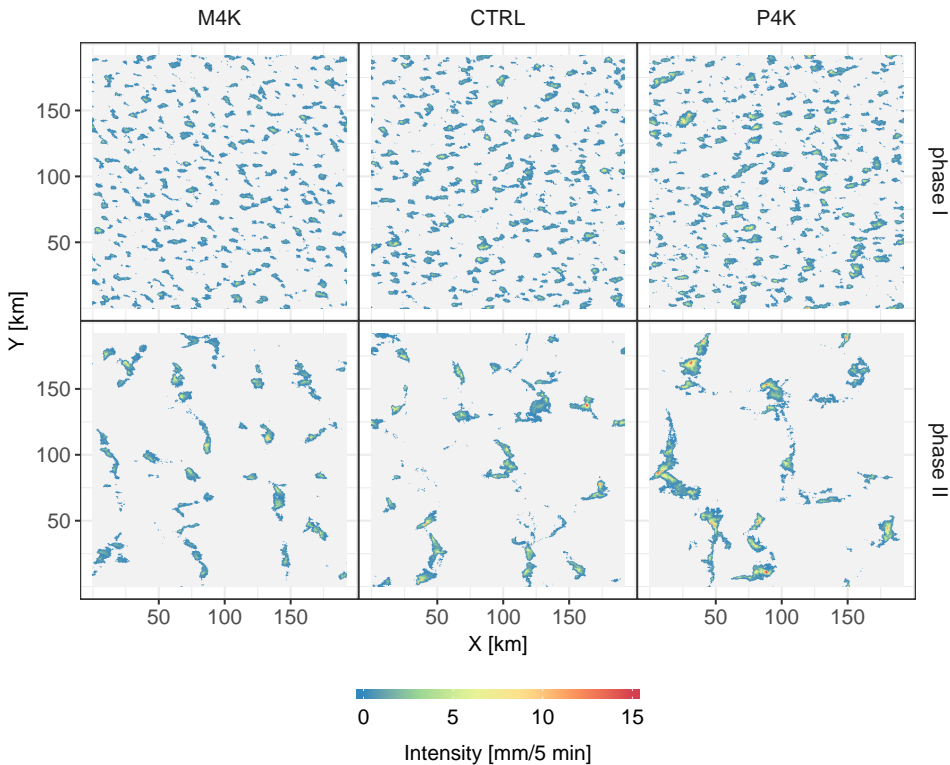
Figure 3.3: Snapshots of the precipitation field at the center of phase I and phase II (upper and lower panels). Three experiments: M4K, CTRLand P4K (left to right). Grey areas indicate no or below-threshold precipitation.

The evolution from finer to coarser structures is similar to the results of Moseley et al. [2016] where the spatial scale of areas of low level moisture convergence and divergence increases in the course of the simulation. Indeed, a Hovmoeller diagram of vertical velocity, a proxy for convergence, at 100 m (Figure S3.5) reveals comparable patterns. Snapshots of the full horizontal field in phases I and II complement the picture, indicating that distances between regions of strong convergence increase (Figure 3.4). The process seems to be amplified by higher temperatures.
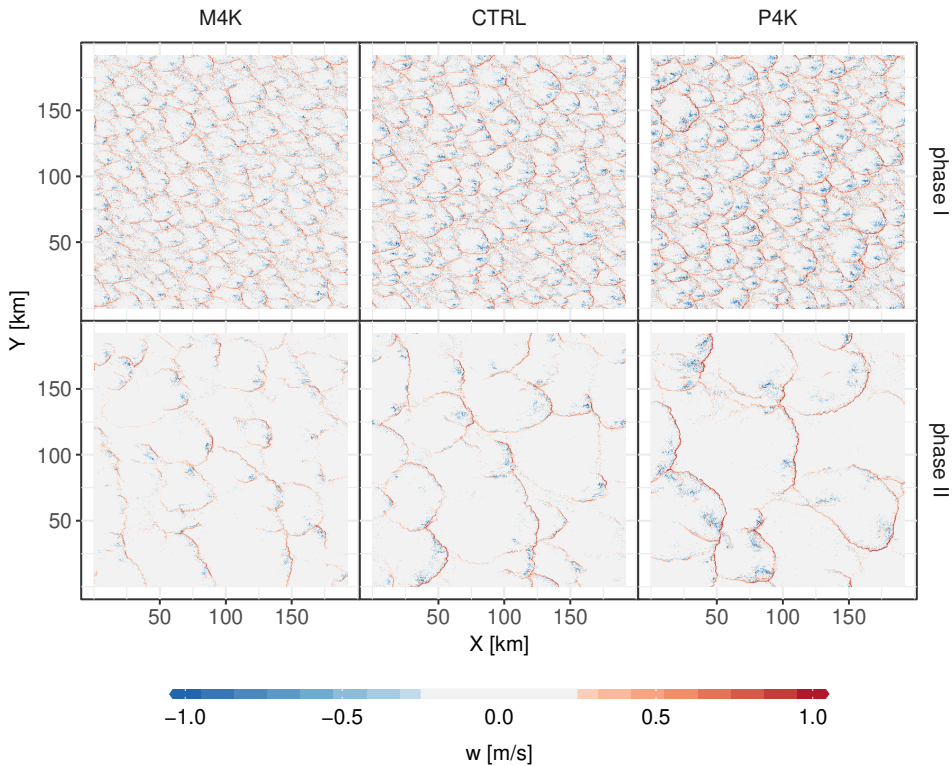
Figure 3.4: Snapshots of vertical velocity w at a height of 100m. Note that values between $-0.25\,\mathrm{m\,s^{-1}}$ and $+0.25\,\mathrm{m\,s^{-1}}$ are colored in gray.

In the following sections, we will, according to the structure of Figure 3.3, examine how the spatial variability and intensities change with varying temperature, as well as between the two active phases of convective rainfall. To this purpose, we investigate the properties of rain cells, which are defined as continuous areas with rainfall. We extract the size L (square root of the area) of rain cells in phases I and II and calculate the number of cells that exceed a certain size (Figure 3.5). In phase I, all experiments have similar distributions up until a size threshold of approximately 5 km. Beyond this size, the distributions diverge for the different experiments. For instance, rain cells larger than 8 km are, in absolute terms, four times more frequent in the P4K run than in the M4K run. This

represents a corresponding change of the empirical cumulative distribution function for the different experiments (Figure S3.6). Thus, larger rain cells grow further in size and become more frequent with increasing temperature and moisture availability.
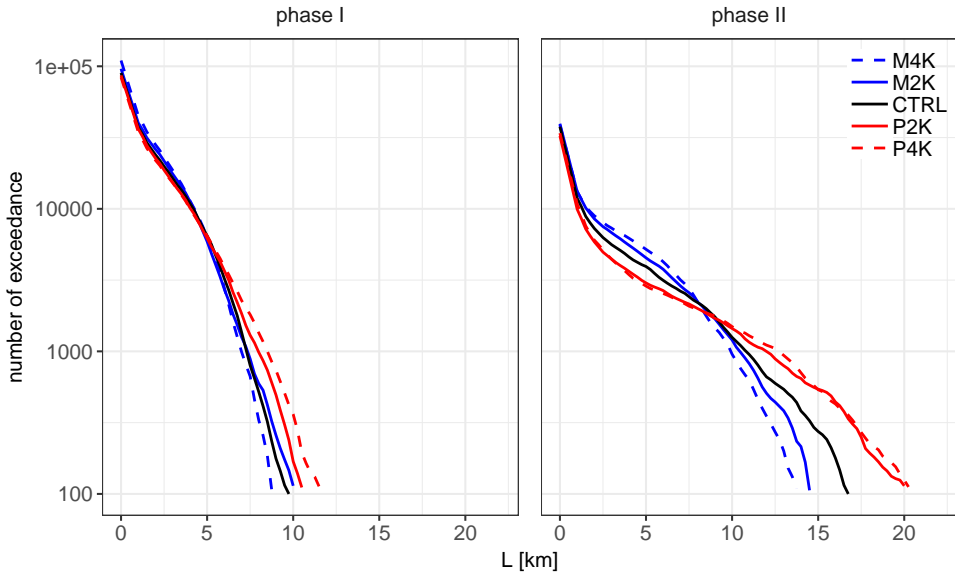
Figure 3.5: The number of rain cells which exceed a certain size L in phases I and II. We cut off at the threshold with less than 100 cells left. Note the logarithmic y-axis.

Proceeding to phase II in Figure 3.5, we see a drastic change of the situation. A remarkable difference to phase I is the general increase of rain cell size. Across all experiments, the curves reach higher values before they drop off to very low numbers of cells. Another distinct difference to phase I is the weaker decrease of number of cells with cell size which implies that the total rainfall area is more determined by the larger cells. Again, a consultation of the empirical cumulative distribution function confirms the aforementioned aspects (see Figure S3.6). Colder runs bear a larger number but smaller sized rain cells than the warmer runs. The precipitation field of the warmer runs is characterized by fewer but larger rain cells. The total number of rain cells in each phase varies accordingly: In phase I, the P4K run has 24 % less cells compared to the M4K run; in phase II, it is 12 %. This characteristic is also visible in the top panel ($L > 0$) of Figure 3.6.

The temporal evolution of the transition from smaller to larger cells in the course of the simulation is depicted in Figure 3.6. Choosing a rain cell size of 9 km and counting the number of cells that exceed this value (within a moving time window of one hour) reveals a nearly continuous scale increase across all experiments. For the lower threshold (6 km), we see that warmer model runs have more cells in phase I than the colder experiments. In phase II, this hierarchy reverses. For the higher thresholds, a clear dominance of the warmer experiments emerges. A threshold of 12 km is already beyond the range of the cell size distribution of phase I for all experiments except P4K. None of the
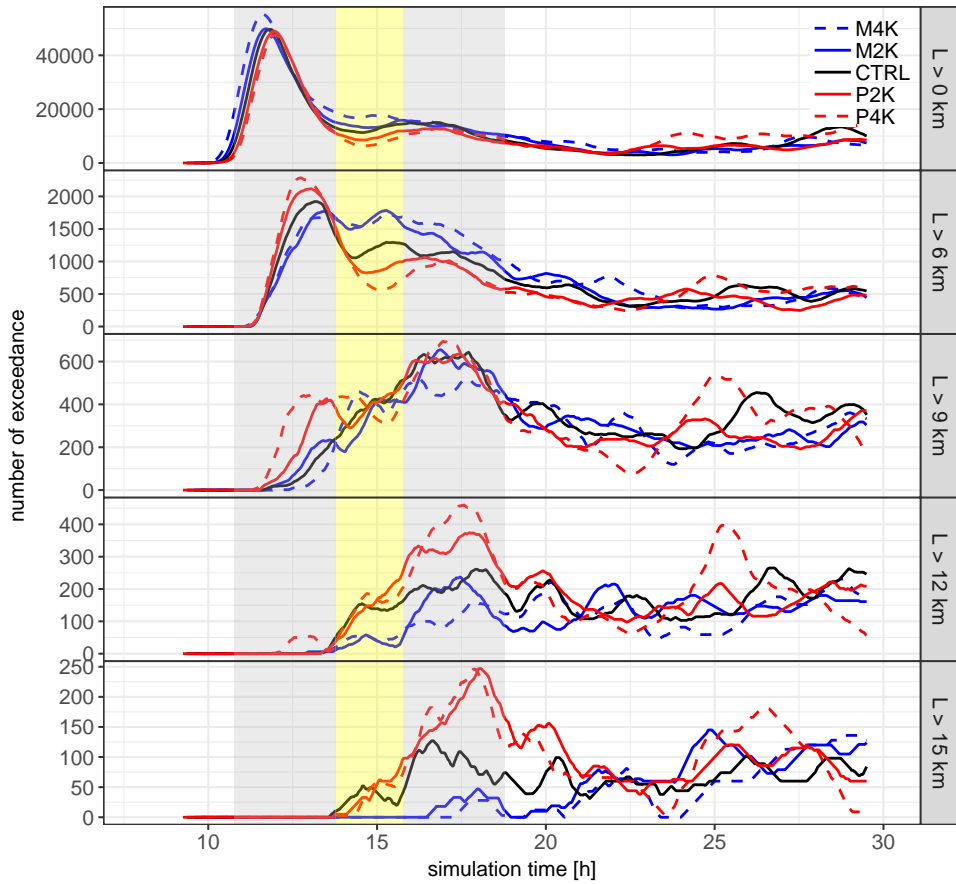
Figure 3.6: Time series of number of exceedance conditional on various thresholds for size L (grey box on the right side). Numbers are counted in a moving time window of one hour.

experiments reaches cell sizes exceeding 15 km. The presence of such cells kicks in during the transition to phase II with the strongest rate of increase in the P2K and P4K runs. However, about 2 to 3 hours after phase II, the time series of all experiments reach a comparable level, and the temporal variability is clearly larger than the systematic differences between the experiments. Snapshots of the precipitation field in this part of the simulation (Figure S3.7) show no clear tendency of an increase of rain cell size with dew point temperature. A replication of Figure 3.5 with data from two additional time windows, centered at 23 hours and 27 hours of simulation time (Figure S3.8), confirms the lack of a systematic response of rain cell sizes to the perturbed initial conditions in the last part of the simulation.

3.3.3. RAINFALL INTENSITY AND THE RELATION TO SPATIAL PROPERTIES

Besides the growth of the largest rain cells with dew point temperature, the snapshots in Figure 3.3 indicate an accompanying intensification of rainfall rates. To quantify this relation, we perform a scaling analysis. More specifically, we relate extreme rainfall statistics to dew point temperature and calculate the fractional rate of change by fitting a linear model to log-transformed precipitation intensities. To obtain an overview on the general increase of intensities with dew point temperature, we first carry out the scaling analysis for unconditional grid point based rainfall rates. The most left panels in Figure 3.7 show the results for both phases. To ease the visual interpretation of the scaling rates, we transformed the y-axis to a logarithmic scale and added auxiliary lines that indicate a fractional increase of $10\,\%\,K^{-1}$. Thus, the slope of the scaling line is the fractional rate of change per degree dew point temperature.

In correspondence to Figure 3.2, intensities are higher in phase II compared to phase I. Also, intensities are higher for the warmer runs. Depending on the chosen percentile, they scale with a rate ranging from around $7.8\,\%\,K^{-1}$ to approximately $10\,\%\,K^{-1}$. Despite the difference in intensities between phase I and II, the scaling rates are quite similar.

To examine how this finding relates to the intensities of rain cells, we repeated the analysis with rain cell average intensities instead of grid point intensities. The results are depicted in the middle panels of Figure 3.7. Similar to the grid point intensities, the two highest percentiles of rain cell average intensities follow approximately the same scaling rate in both phases and are only shifted on the vertical axis. However, for the lower percentiles in phase II, scaling rates stall and even reverse to a negative scaling. Moreover, compared to the grid-point based scaling estimate, we find that rain cell average intensities scale at lower rates ranging from $5.3\,\%\,K^{-1}$ to $7.2\,\%\,K^{-1}$ for the 97.5th and 99th percentile.

Taking into account the rain cell size, we repeated the scaling analysis with the cell-aggregated rain rate. The right panels in Figure 3.7 show the results. The large difference in absolute values between phase I and II reflects the presence of considerably larger rain cells in phase II. The fact that warmer runs generally have larger rain cells induces that scaling rates are higher than for grid point based or rain cell average intensities. In phase I, the cell-aggregated rain rate increases on average by $11.3\,\%\,K^{-1}$ with a maximum of about $13.2\,\%\,K^{-1}$. In phase II, scaling rates reach $16.2\,\%\,K^{-1}$ to almost $20\,\%\,K^{-1}$ (97.5th and 99th percentile). For the lower two percentiles in phase II, we observe as in the analysis for the rain cell average intensity that the scaling rates stall or even change sign.
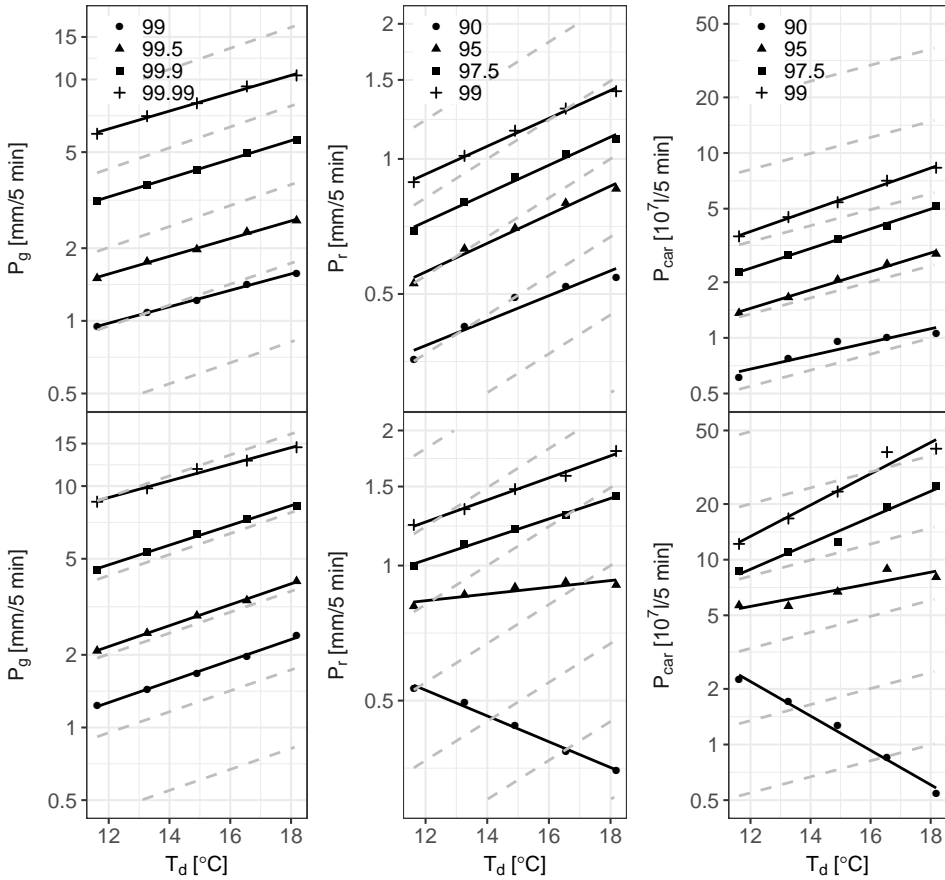
Figure 3.7: Scaling of high percentiles of various rainfall measures with dew point temperature T_d. From left to right: grid point intensities P_g, rain cell average intensities P_r and cell-aggregated rain rate P_{car}. Upper panels show the results for phase I, lower panels for phase II. Percentiles for P_g are derived from all available data. That includes grid points with no precipitation. Each run is located on the x-axis according to the average dew point temperature (lowest model level) of the whole model run. The CTRLsimulation is at approximately 15 °C. Dashed lines indicate a fractional increase of $10 \% \mathrm{K}^{-1}$. Note the logarithmic y-axes.

3
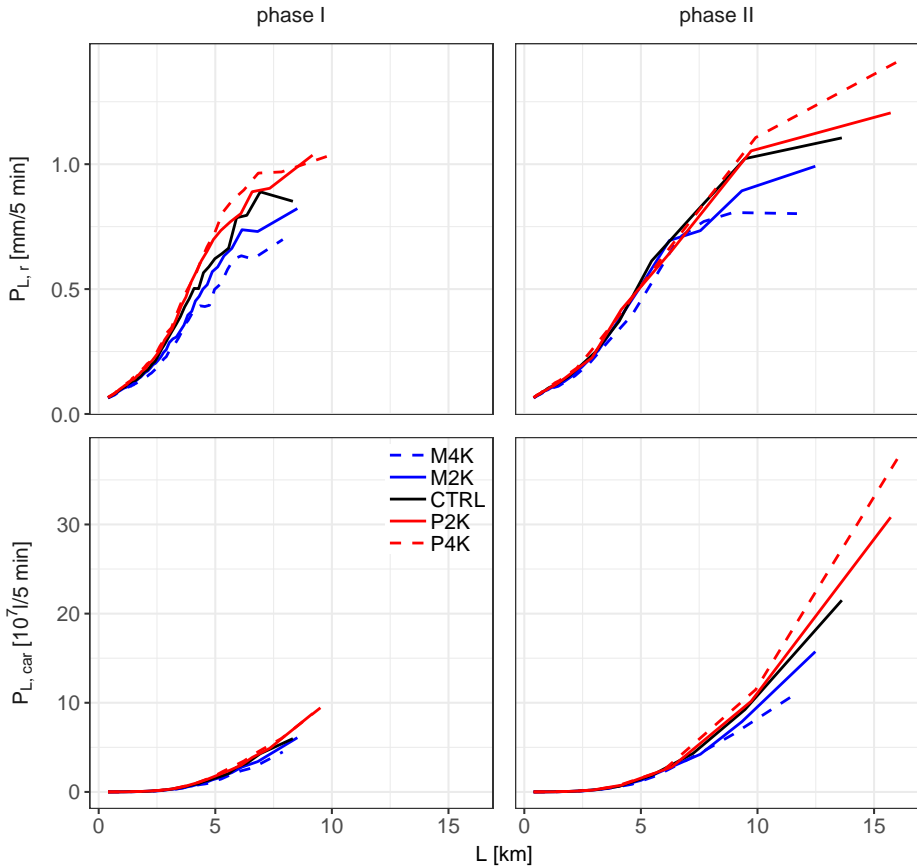
Figure 3.8: Average cell mean intensity conditional on cell size $P_{L,r}$ (upper panels) and cell-aggregated rate $P_{L,car}$ (lower panels). Cells are binned based on their size with (at least) 1000 cells in each bin. The mean intensity and mean cell-aggregated rate are plotted against the mean cell size in each bin.

These results highlight that the reshaping of the precipitation field between phases I and II has systematic consequences. Rain cells in phase I do not only grow substantially in size during the transition to phase II, they also become stronger in intensity. Both factors together yield higher precipitation amounts in phase II. Warmer temperatures and higher moisture availability amplify these two processes.

To visualize how cell size relates to cell intensity and cell-aggregated rain rate, we conditioned these statistics on the cell size (see equations 3.8 and 3.9). The mean cell intensity increases with cell size (Figure 3.8). Also, the warmer runs have higher intensities for cells of the same size. The behavior can been seen for both phases. In phase II, however, up to cell sizes of 8 km, the intensity of all experiments is similar and, therefore, does not depend on dew point. This is about the same cell size threshold as in Figure 3.5,

where a decrease in cell number with warming turns into an increase.

The cell-aggregated rain rate shows a similar behavior. Values mostly increase with warming. For instance, a rain cell in the P4K run has a larger aggregated rain rate than a rain cell of the same size in the M4K experiment. However, compared to the mean cell intensity, the relative difference of the maxima between the two phases is larger. Additionally, cell-aggregated rain rates, especially in phase II, steeply increase for the largest rain cell sizes. Analogous to the mean cell intensity, the cell-aggregated rate is similar in all experiments up to a cell size of 8 km. This possibly explains the stagnation of scaling rates for the lower two percentiles of rain cell average intensity and cell-aggregated rain rate in Figure 3.7 since smaller rain cells have generally lower intensities.

In summary, warmer and moister atmospheric conditions lead to a faster growth of larger cells that are more intense. Together, they produce much higher cell-aggregated rain rates, well exceeding the CC rate of $7\,\%\,K^{-1}$.
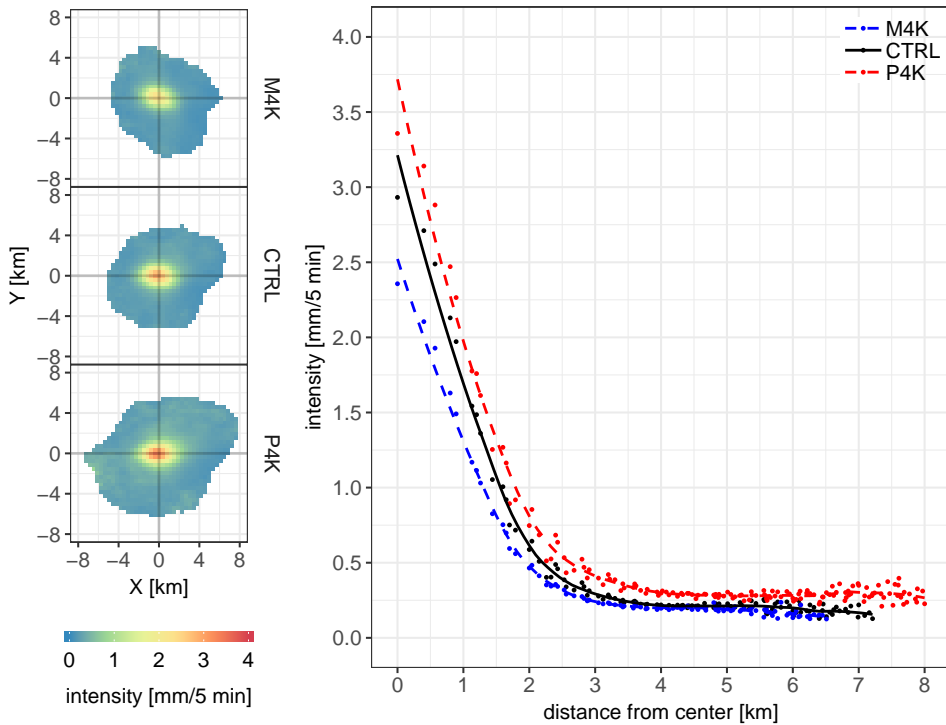
Figure 3.9: Composites (median) of the 5000 strongest precipitating rain cells in phase I (left) and the corresponding radial averages (right). Rain cells are centered on the intensity weighted center of mass. Note that individual cells might be larger since we exclude grid points from the composite which are covered by less than 250 rain cells. Radial averages are constructed by using the number of cells that cover individual grid points of the same distance as weights. Dots in the right panel represent the calculated average intensity at a certain distance. The lines are local polynomial regression fits.

Up to now, we only considered the cell mean intensity and did not investigate whether there is a redistribution of intensities within the cell. To investigate this, we made spatial

composites of the 5000 strongest precipitating cells during phase I (Figure 3.9), noting that a similar analysis for phase II is not possible due to the asymmetric shape of cells and their limited number. The composites show that rain cells cover, on average, a larger area in the P4K experiment than in the CTRL or M4K runs. Intensity increases as well. The corresponding radial averages extend our knowledge about their characteristic by the fact that intensities also increase at larger distances from the center. There is no indication of a redistribution of intensities toward the cell center at the expense of the intensities at the cell borders.

3.4. CONCLUSIONS AND DISCUSSION

This chapter presents the results of idealized convection resolving simulations with a setup that comprises typical conditions for heavy rainfall in midlatitudes. The construction of the case was accomplished by compositing the forcing from a reanalysis product using a set of observed extremes [Lenderink et al., 2017] for the Netherlands following the approach of Loriaux et al. [2017]. This produces a realistic forcing in terms of large-scale and surface driven components. However, the fact that the meso-organization of the rain events takes longer forced us to stretch out the day from 24 to 36 hours in order to obtain a realistic timing in the peak of the convective activity as compared to the large-scale forcing. While this obviously reduces the realism of the case setup, the length of strong and organized convection in the period we study (less than 10 hours, phase I and phase II) is still within the lifespan of observed mesoscale convective systems [Feng et al., 2012]. Another potential drawback is that our simulations make use of a rather simple microphysics scheme. A single-moment microphysics parameterization keeps the computational cost of our simulations on a feasible level. However, we note that the choice of the microphysics scheme can influence, for example, in-cloud properties such as updraft velocities and latent heating, mostly through ice-related processes [Fan et al., 2017]. Moreover, the representation of ice-related microphysics can affect the simulated response of extreme precipitation to surface warming [Singh and O'Gorman, 2014].

Besides the control simulation, we conducted a set of experiments with perturbed initial temperature and specific humidity profiles. With this as a basis, we examined the evolution of the precipitation field throughout one diurnal cycle and its response to changes in atmospheric temperature and moisture content.

The simulations are characterized by a development toward larger rainfall structures in time. After the onset of precipitation, many small, regularly scattered rain cells are present (phase I). Correspondingly, the precipitation area fraction quickly peaks. About 5 h later (phase II), we observe that, while the precipitation area fraction has decreased, the precipitation field reshaped to fewer but larger rain cells. The distribution of rain cell size undergoes radical changes during the transition between the two phases. Many of the small cells of phase I decay, and fewer but much larger rain cells start to develop. At the same time, these larger rainfall structures have higher intensities than the small cells of phase I. Overall, precipitation rates, with minor fluctuations, continuously increase until the end of phase II.

Both phases demonstrate a systematic response to the initial conditions, but after the end of phase II, results are much more similar across all experiments. In both phases,

rainfall rates are higher under warmer conditions and the dependency of extreme precipitation rates on surface dew point temperature exceeds the CC relation. However, cell mean intensities scale below the CC relation. These apparently conflicting rates are caused by the presence of more larger cells with higher intensities in the warmer simulations. Particularly in phase II, the cell size distribution is strongly determined by the largest rain cells. Even more, the growth of the largest rain cells with higher temperatures occurs at the cost of smaller sized rain cells. Consequently, the number of rain cells decreases. A conditional analysis of cell intensity on its size revealed a strong relation between the two characteristics. Indeed, area and mean intensity combined as the cell-aggregated rain rate shows a much stronger scaling with ambient dew point temperature, well exceeding the CC relation in both phases. The increase of intensities throughout most of the rain cell area plays a key role in this context.

Our results suggest that higher temperatures and a proportional increase of moisture availability according to the CC relation lead to a stronger organization of convective precipitation cells to larger spatial extent with higher intensities. We find no signal of a concentration or limitation of intensity increase to the center of rain cells accompanied by a decrease of the spatial extent and a redistribution of moisture as proposed by Wasko et al. [2016], Li et al. [2018], and Peleg et al. [2018]. We note that these studies cover different regions of the world with different climates which complicates a comparison. In this context moisture limitation may play an important role for the redistribution of intensities within rain cells. Also, besides technical aspects (e.g., different metrics for the spatial extent or the use of dew point versus dry bulb temperature), part of the conflicting results may be explained by the approach to define rain events. For instance, Wasko et al. [2016] and Li et al. [2018] cluster station observations with simultaneous rain within a certain radius to rainfall events. This method considers only larger storms and misses information at locations without stations. Here we include finer details of convective rain cells and are able to sample a more continuous spectrum of the their size in the range from around 12 °C to 18 °C dew point temperature. Given this, we find that intensity and size of rain cells jointly increase under warming atmospheric conditions which is in line with the results of Lochbihler et al. [2017] and Lenderink et al. [2017].

APPENDIX

DATA AVAILABILITY

Data Set D3.1: A data set with the DALES case setup is available at
https://dx.doi.org/10.4121/uuid:1b74fab6-461e-44fd-a283-45b1a2f11d56.

FIGURES

3
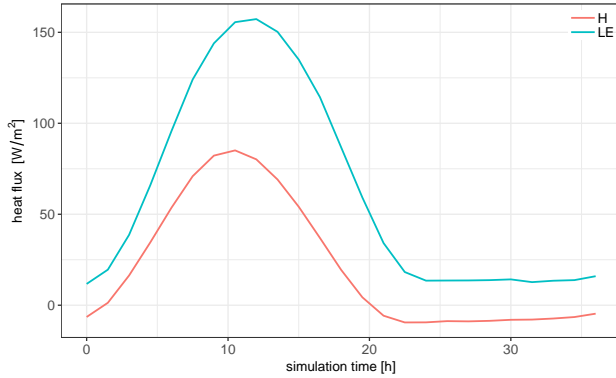
Figure S3.1: Surface forcings for the DALES simulations. Sensible (H) and latent heat (LE) fluxes.
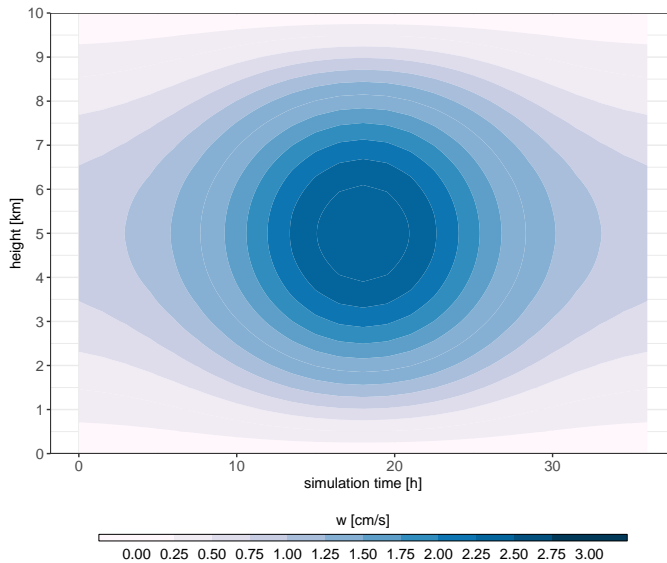
Figure S3.2: Idealized large scale forcing for vertical velocity w.
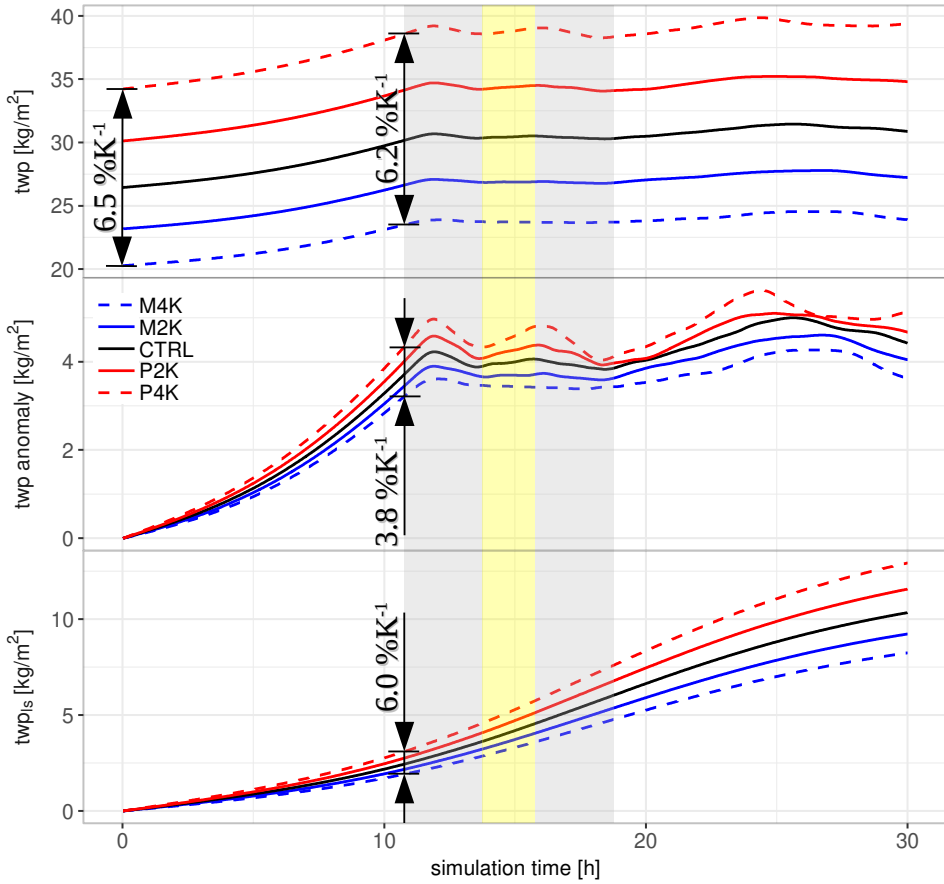
Figure S3.3: Time series (domain averages) of total water path (twp), the total water path anomaly (with respect to initial conditions) and the contribution of the large scale moisture convergence (twp_{ls}). Scaling rates of each quantity at certain time steps of the simulation are added as annotations.

3
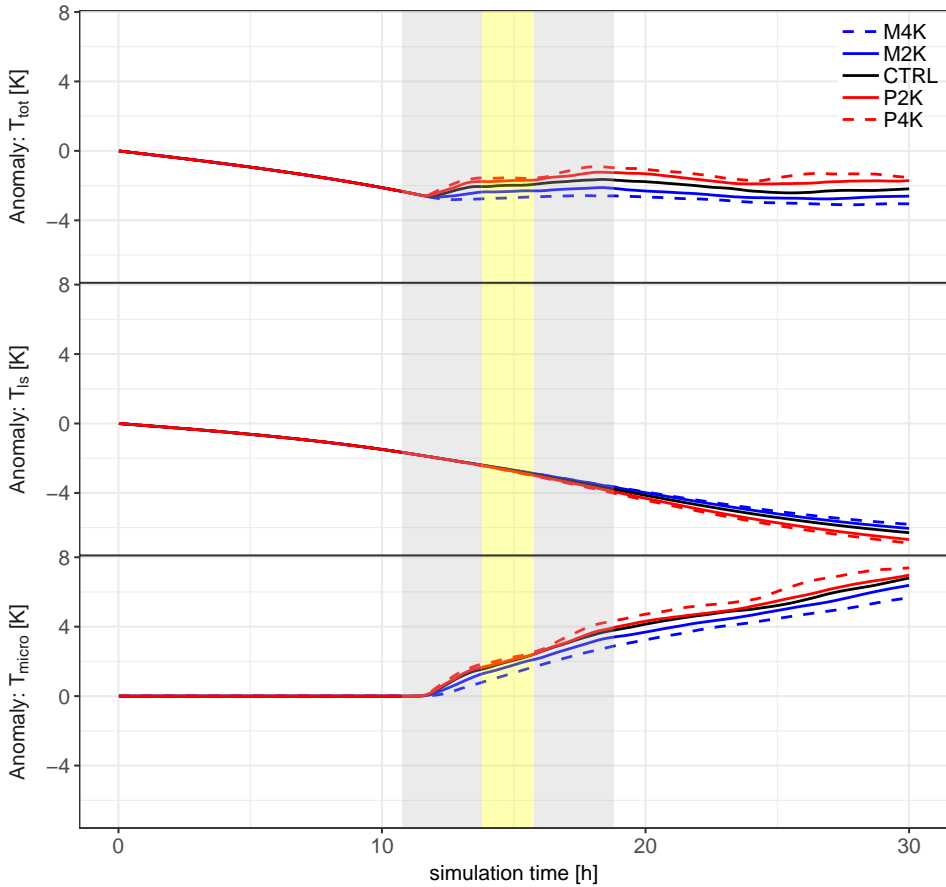
Figure S3.4: Time series (domain averages) of temperature anomaly T_{tot} (with respect to initial conditions), the contribution of the large scale convergence T_{ls} and the latent heating due to microphysics T_{micro} at a height of approximately 5 km.
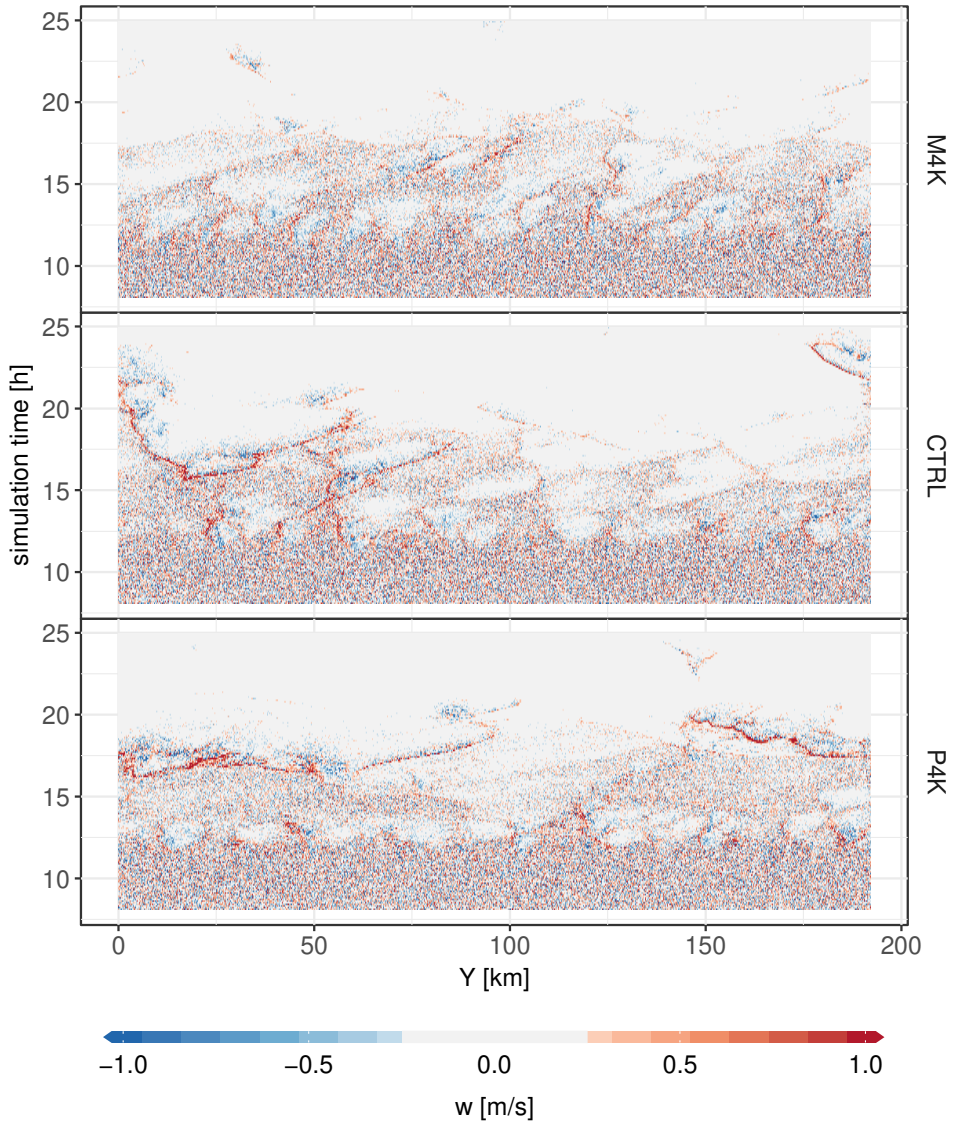
Figure S3.5: Hovmoeller diagram of vertical velocity w at 100m above ground for the M4K, CTRL and P4K simulations. The vertical axis represents time while the horizontal axis is the spatial y dimension of the simulation domain.

3
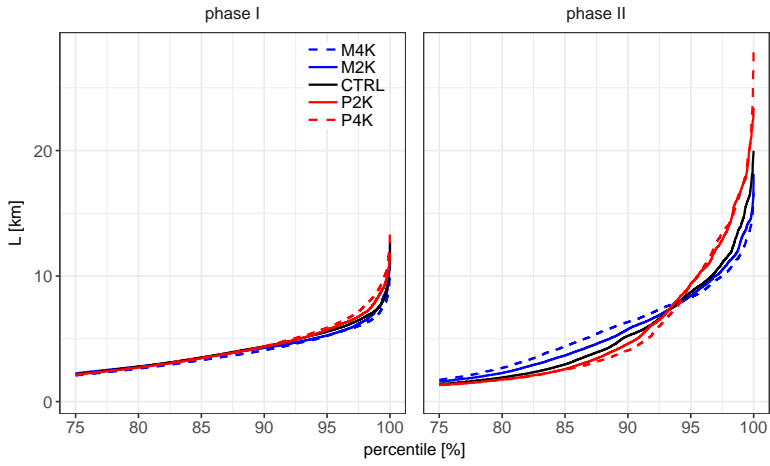
Figure S3.6: Empirical cumulative distribution function (ECDF) for the size L of all rain cells in phase I and phase II.
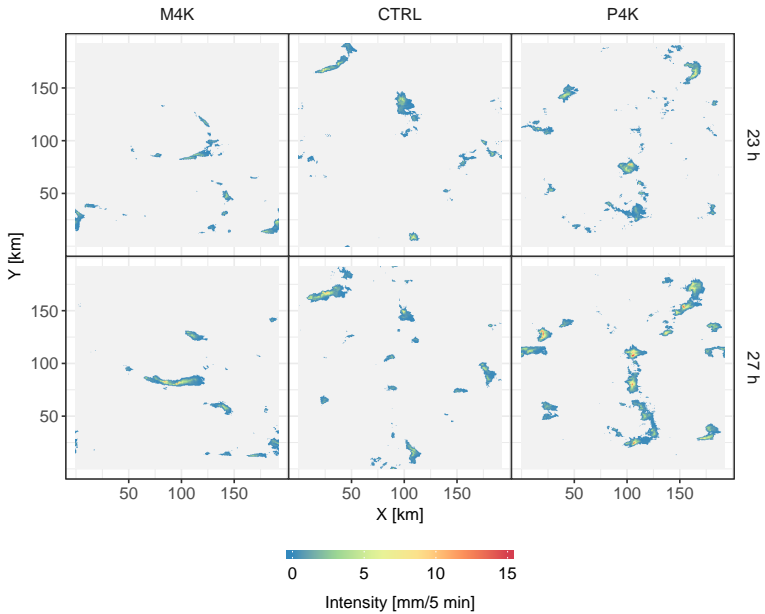
Figure S3.7: Snapshots of the precipitation field at 23 hours and 27 hours of simulation time.
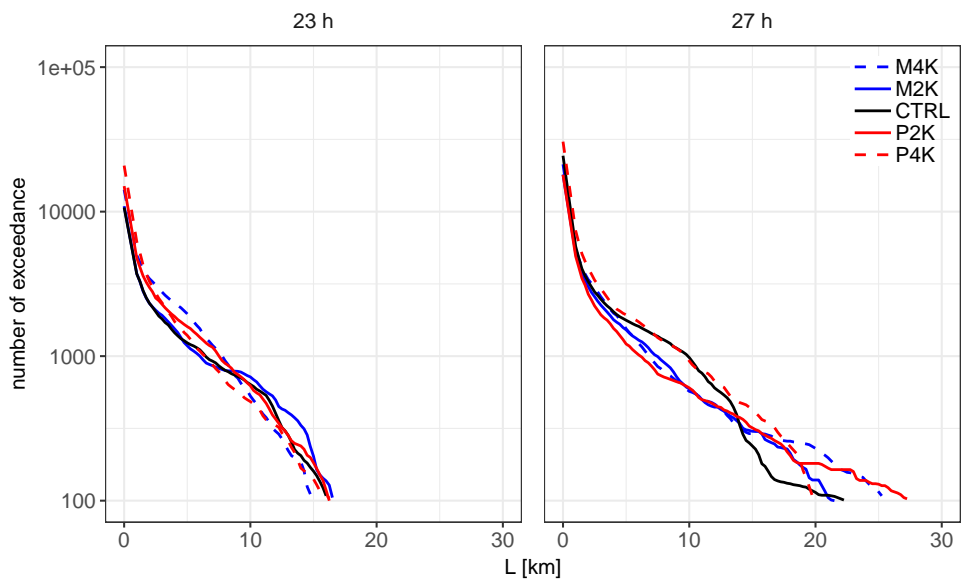
Figure S3.8: The number of cells that exceed a certain size L for two time windows of three hours centered around 23 hours and 27 hours simulation time.

4

COLD POOL DYNAMICS SHAPE THE RESPONSE OF EXTREME RAINFALL EVENTS TO CLIMATE CHANGE

There is increasing evidence that local rainfall extremes can increase with warming at a higher rate than expected from the Clausius-Clapeyron (CC) relation. The exact mechanisms behind this super CC-scaling phenomenon are still unsolved. Recent studies highlight invigorated local dynamics as a contributor to enhanced precipitation rates with warming. Here, cold pools play an important role in the process of organization and deepening of convective clouds. Another known effect of cold pools is the amplification of low-level moisture variability. Yet, how these processes respond to climatic warming and how they relate to enhanced precipitation rates remains largely unanswered. Unlike other studies which use rather simple approaches mimicking climate change, we present a much more comprehensive set of experiments using a high-resolution large eddy simulation (LES) model. We use an idealized but realistically forced case setup, representative for conditions with extreme summer precipitation in midlatitudes. Based on that, we examine how a warmer atmosphere under the assumption of constant and varying relative humidity, lapse rate changes and enhanced large-scale dynamics influence precipitation rates, cold pool dynamics, and the low-level moisture field. Warmer conditions generally lead to larger and more intense events, accompanied by enhanced cold pool dynamics and a concurring moisture accumulation in confined regions. The latter are known as preferred locations for new convective events. Our results show that cold pool dynamics play an increasingly important role in shaping the response of local precipitation extremes to global warming, providing a potential mechanism for super CC behavior as subject for future research.

4.1. INTRODUCTION

Precipitation extremes are commonly expected to increase with global temperature rise. Global climate model simulations show, that on large spatial and long temporal scales, the Clausius-Clapeyron (CC) relation presents a robust constraint in this context [Pall et al., 2007; Tebaldi et al., 2006]. However, there are indications that on small spatial and short temporal scales a warming atmosphere enables rainfall amounts to increase above the CC rate of $7\,\%\,°C^{-1}$. For instance, Lenderink and van Meijgaard [2008] and Loriaux et al. [2013] showed that extremes of hourly and subhourly precipitation observations in the Netherlands exhibit an increase with warming up to $14\,\%\,°C^{-1}$. Similar results have been obtained for other locations, for example, in Germany [Berg et al., 2013; Moseley et al., 2013], Hong Kong [Lenderink et al., 2011], and some regions of Australia [Wasko et al., 2018].

The mechanism behind the phenomenon of enhanced precipitation scaling with warming beyond the CC rate is still subject to ongoing research. A common theory suggests that invigorated convective updrafts through additional latent heating amplify moisture convergence and therefore moisture supply to the storm itself [Trenberth et al., 2003]. Indeed, enhanced large-scale convergence is often found in combination with high precipitation rates and even further increases at warmer and moister surface conditions [Lenderink et al., 2017]. The spatial properties of rainfall events might also play a crucial role here. Rain radar data analysis reveals that convective rain cells grow larger and intensify over most of their area at higher temperatures and moisture availability [Lochbihler et al., 2017]. Similar results from LES simulations confirm that size and intensity of rainfall events are clearly linked in such a scenario [Lochbihler et al., 2019]. This indicates that enhanced precipitation intensities are at least partly attributable to a larger area of moisture supply to the storm.

Another potential driver for enhanced precipitation rates with warming is cloud-cloud interaction through cold pools. According to Tompkins [2001], cold pools generally evolve in the following manner. After an initial cooling and moistening of the subcloud layer through the evaporation of falling rain drops, the resulting relatively cold and dry air masses descend to lower levels, driven by gravity, and eventually reach the surface. This forces the cold pool to spread horizontally and while it remains relatively dry in the center the edges are moist. The resulting dynamics let cold pools play an important role for the formation of deep convection. If cold pool formation is suppressed, clouds remain small and shallow [Khairoutdinov and Randall, 2006; Böing et al., 2012]. Furthermore, the triggering of convection at cold pool edges [e.g., Tompkins, 2001; Seifert and Heus, 2013; Torri et al., 2015; Hirt et al., 2020] or by collision of two or more cold pools [e.g., Haerter et al., 2019] plays a crucial role in the process of convective self-aggregation and organization.

Cold pool dynamics also modify the local low-level moisture field and, hence, moisture availability to convective clouds. For instance, Schlemmer and Hohenegger [2016] show, by using idealized large eddy simulations (LES), that most of the accumulated moisture in nonprecipitating regions stems from the advection through laterally spreading cold pools. Other sources, for example, surface fluxes, play a rather minor role in this context [Schlemmer and Hohenegger, 2016; Fuglestvedt and Haerter, 2020]. These regions of relatively higher moisture content are then preferred locations for new con-

vective cells. Evidence for the link between cold pool induced moisture convergence and subsequent convective events is further strengthened by Fuglestvedt and Haerter [2020]. The authors use a back tracking method to establish a direct connection between cold pools as moisture conveyors and new convective rain events.

In this study, we use an LES model (200 m resolution on a 192 km × 192 km domain) to analyze cold pool properties, and their relation to rainfall rates, for a case of heavy convection at midlatitudes. Previous studies have used rather simple perturbations to mimic climate change [e.g. Haerter and Schlemmer, 2018], but here we present a much larger set of perturbed experiments. These perturbations reflect warmer climatic perturbations, and cooler as well, based on projected changes of large-scale conditions in global climate model simulations. As such, besides perturbations with uniform vertical warming, and constant relative humidity, also different perturbations with enhanced warming at upper levels (reflecting a stabilization of the atmosphere in terms of the dry lapse rate) and decreased relative humidity are studied. Although these perturbations cover a broad range of possible future conditions, they obviously do not sample climate change to a full extent.

These experiments also differ from the radiative-convective equilibrium (RCE) simulations performed for the tropics where CC scaling robustly applies [e.g. Fildier et al., 2017; Romps, 2011]. Instead of studying the quasiequilibrium response in RCE, we use a strongly time varying forcing which destabilizes the atmosphere and provides moisture, and which are connected to surface fluxes and the passage of a larger-scale (synoptic) disturbance. For each of the resulting 25 experiments, we identify rain events, cold pools, and moist areas by a clustering method. We investigate how the intensity and size of rain events differs between the different simulations and how cold pool activity and the low-level moisture field relates to that.

4.2. METHODS

4.2.1. SIMULATION SETUP

We use the Dutch Atmospheric Large Eddy Simulation (DALES) model [v4.1; Heus et al., 2010; Böing et al., 2012] with a single moment cloud microphysics scheme [Grabowski, 1998; Böing et al., 2012]. The evaporation of rain drops is parameterized as a function of the saturation deficit of the surrounding air mass, making the model suitable to study the effects of cold pools. The large scale forcings, radiative cooling (1.5 K/day) and surface fluxes are prescribed. The simulations run with a horizontal resolution of 200 m on a domain of 192 km × 192 km. The vertical grid has 240 levels with a variable layer thickness ranging from 40 m near the surface to 150 m at the top.

The case setup and forcing is similar to the LES simulation in Lochbihler et al. [2019] and Loriaux et al. [2017]. They were derived from a typical summer day with extreme precipitation in the Netherlands under current climate providing initial conditions (Figure 4.1), surface forcing and large-scale winds, including the large-scale vertical velocity, omega [for details, see Lochbihler et al., 2019]. In contrast to the case setup in Lochbihler et al. [2019], we used a normal day length, but to allow a longer period of organized convection, we instead extended the peak forcing of omega and surface fluxes during the second half of the simulation (see Figures S4.1 and S4.2). This is primarily needed
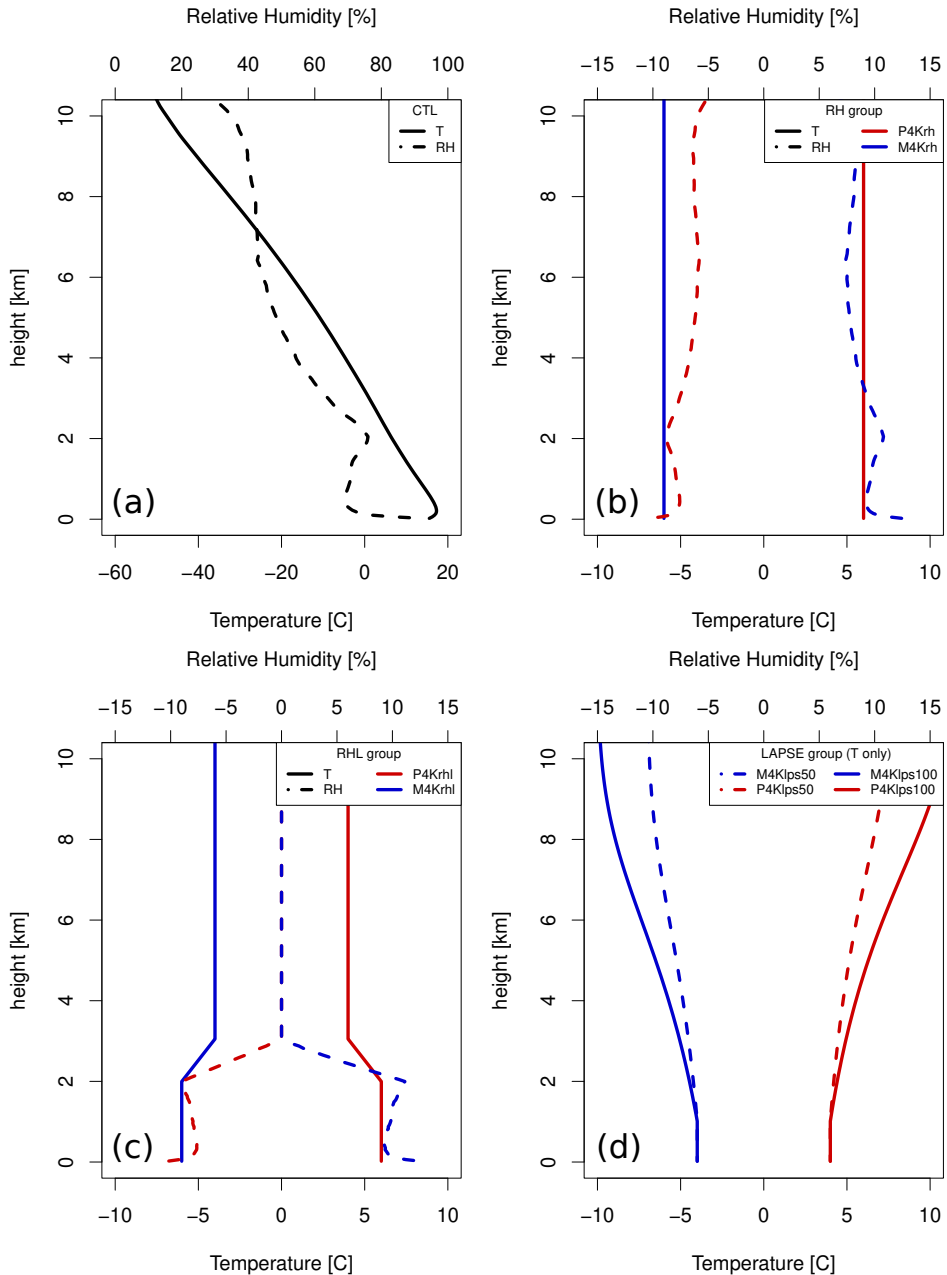
Figure 4.1: Initial temperature T and relative humidity RH profiles of the CTL setup (a) and the relative change of both variables for various types of perturbations, more specifically the RH (b), RHL (c) and LAPSE (d) groups. Note that, except for the LAPSE group, solid lines indicate temperature (bottom axis) and dashed lines represent relative humidity (top axis).

to provide more robust statistics and to overcome limitations from the initialization by spatially uniform conditions leading to an initial convective state which is still characterized by many (unorganized) small-scale showers and considered less realistic [see also Lochbihler et al., 2019]. After this initial state, the precipitation field transforms into fewer but larger multicell events. We refer to this characteristic when we use the term organized.

In addition to the CTL run, we ran a large number of experiments with different perturbation strategies. In total, there are five groups of perturbations which are summarized in Table 4.1.

The first experimental group, named the TEMP group, perturbs the initial temperature profile in steps of 2 K from −4 K to +4 K with respect to CTL. This perturbation is constant with height. The profile of specific humidity is adjusted to keep relative humidity identical to CTL. This leads to an increase/decrease of dew point temperature as indicated in the experiment name tag. The changes in near surface dew point are used as a tag in all other experiments. We note that the stability of the atmosphere with respect to moist processes decreases from colder to warmer runs in such a setting.

Since relative humidity is generally expected to decrease with a warming atmosphere over land [e.g., O'Gorman and Muller, 2010], the second group, RH, introduces changes of relative humidity. This is achieved by taking the profiles of the TEMP group and further increase temperature by 1 K for P2K and 2 K for P4K (P2Krh and P4Krh). In case of the M2K and M4K experiments, temperature is lowered by the respective value (M2Krh and M4Krh). This causes an approximately uniform decrease of relative humidity for the warmer runs (P2Krh and P4Krh), whereas in the colder experiments, humidity is closer to saturation. Figure 4.1b illustrates this for the M4Krh and P4Krh experiments. The M2Krh and P2Krh experiments are approximately half way in between. We note that by applying this procedure, the absolute humidity of the air – near surface as measured by the dew point temperature but also in a vertically integrated sense – is the same as in the TEMP group.

In a similar way, but restricted to levels below 3 km, the experiments in the RHL group have a lower (higher) relative humidity for the P4Krhl (M4Krhl) experiments. Figure 4.1c illustrates this perturbation. This approach represents a more realistic vertical profile of relative humidity changes with warming specifically in the case of extreme precipitation events [see Figure 1b in Attema et al., 2014]. To avoid an abrupt jump of temperature and relative humidity, we linearly interpolate temperature between 3 km and 2 km. Below 2 km, the profiles are identical to the M4Krh and P4Krh experiments. We note that, whereas in RH the atmospheric dry lapse rate (dry stability) is unchanged compared to the TEMP group, in this experiment changes in dry stability occur due to the enhanced boundary layer warming imposed.

Atmospheric warming due to a climate change is expected to vary with height, which is primarily related to convection which tends to keep the atmospheric lapse rate close to a moist adiabat with greater warming aloft [Tett et al., 1996; Bony et al., 2006]. To account for these changes in the thermal stratification as the atmosphere warms, we apply a nonuniform temperature perturbation. Using a similar approach as in Loriaux et al. [2013], the temperature perturbations of the experiments M4Klps100 and P4Klps100 of the LAPSE group follow a moist adiabatic lapse rate, while the M4Klps50 and P4Klps50

experiments are subjected to a temperature change that is halfway between a moist adiabatic perturbation and a uniform perturbation. More specifically, the resulting temperature profiles are a linear combination of a constant shift (e.g., P4K) and (the fraction of) a moist adiabatic temperature perturbation. For a more detailed description, see section 5 in Loriaux et al. [2013]. All profiles of the temperature perturbations from the LAPSE group are displayed in Figure 4.1d. Note, that all these perturbations are uniform below 1 km which is approximately equal to the height of the lifting condensation level. The specific humidity is modified in all the experiments of the LAPSE group to keep the relative humidity identical to CTL. Since moist adiabatic perturbations hardly affect the moist stability of the atmosphere, it should be noted that the destabilization of the atmosphere with warming is much stronger for the TEMP group than for the LAPSE group (see also Figure S4.3 that shows the time development of the CAPE of the various experiments). Also, we note that the vertically integrated water vapor is not identical to the corresponding experiments in the TEMP group (compare Figure S4.4).

The last perturbation group varies the large-scale convergence (LS). Extreme precipitation events are often associated with a strong large-scale vertical lifting [Lenderink et al., 2017]. Thus, we carry out an additional group of simulations, LS, with enhanced forcing of the large-scale vertical velocity, w_{ls}. This is done by increasing w_{ls} in the TEMP experiments by 30 % and 60 %.

As an aside we note that, due to intensive testing, we were able to obtain three realizations of the CTL and two of the M2K. They are represented as separate dots/lines in all following figures.

4.2.2. IDENTIFICATION OF RAIN CELLS, COLD POOLS, AND MOIST PATCHES

Following the approach of Lochbihler et al. [2017, 2019], we group continuous areas of surface precipitation to clusters hereby called rain cells. Two grid points belong to the same rain cell if they are neighbors in x or y direction. In order to avoid small cells with low intensity, grid points below a threshold of 0.6 mm h^{-1} are ignored. For the same reason we first coarse grain the precipitation output from a resolution of 200 m to 400 m.

The principles of the described clustering process can also be used for the identification of cold pools. However, the detection criteria are obviously different. We follow the method of Schlemmer and Hohenegger [2014, 2016]. Since a cold pool is a descending, relatively cold and dry air mass originating from evaporation of rain drops, the equivalent potential temperature (θ_e) is a suitable indicator to diagnose the presence of a cold pool. More specifically, we calculate a low-level average of θ_e and subtract the domain average for each time step to obtain the horizontal field anomaly $\Delta\theta_e$. Unlike Schlemmer and Hohenegger [2014, 2016], we have only output for two model levels at 20 m and 100 m. The $\Delta\theta_e$ fields are first coarse grained to the same resolution as the precipitation output and then smoothed with a Gaussian low-pass filter to remove remaining numerical noise. Figure 4.2a shows an example taken from the control simulation. In contrast to Schlemmer and Hohenegger [2014], we choose a less restrictive threshold for $\Delta\theta_e$ of −1 K. Testing has shown that this allows for smoother cold pool edges and thus reduces the cutoff of grid points which belong to the same cold pool. However, in accordance with Schlemmer and Hohenegger [2014], we neglect all cold pools that do not reach −2 K. In case of cold pools we also aim to quantify the areal growth rate. Thus, in-

4

	name tag	group tag	perturbation
•	CTL	-	-
•	M4K	TEMP	full-column -4K with const. RH
•	M2K	TEMP	full-column -2K with const. RH
•	P2K	TEMP	full-column +2K with const. RH
•	P4K	TEMP	full-column +4K with const. RH
▲	M4Krh	RH	like M4K but with additional -2K; RH = CTL +10%
▲	M2Krh	RH	like M2K but with additional -1K; RH = CTL +5%
▲	P2Krh	RH	like P2K but with additional +1K; RH = CTL -5%
▲	P4Krh	RH	like P4K but with additional +2K; RH = CTL -10%
■	M4Krhl	RHL	like M4K but with additional -2K below 2 km
■	P4Krhl	RHL	like P4K but with additional +2K below 2 km
+	M4Klps50	LAPSE	M4K with 50% moist adiabat superimposed; RH = CTL
+	P4Klps50	LAPSE	P4K with 50% moist adiabat superimposed; RH = CTL
⊞	M4Klps100	LAPSE	M4K with full moist adiabat superimposed; RH = CTL
⊞	P4Klps100	LAPSE	P4K with full moist adiabat superimposed; RH = CTL
◇	CTLls30	LS	CTL with 30% enhanced large-scale convergence
⊕	CTLls60	LS	CTL with 60% enhanced large-scale convergence
◇	M4Kls30	LS	M4K with 30% enhanced large-scale convergence
◇	P4Kls30	LS	P4K with 30% enhanced large-scale convergence
⊕	M4Kls60	LS	M4K with 60% enhanced large-scale convergence
⊕	P4Kls60	LS	P4K with 60% enhanced large-scale convergence

Table 4.1: Table of experiments. See text for a more elaborate explanation of the different perturbation strategies.

formation about overlapping cold pools from one time step to another are saved during the clustering procedure.
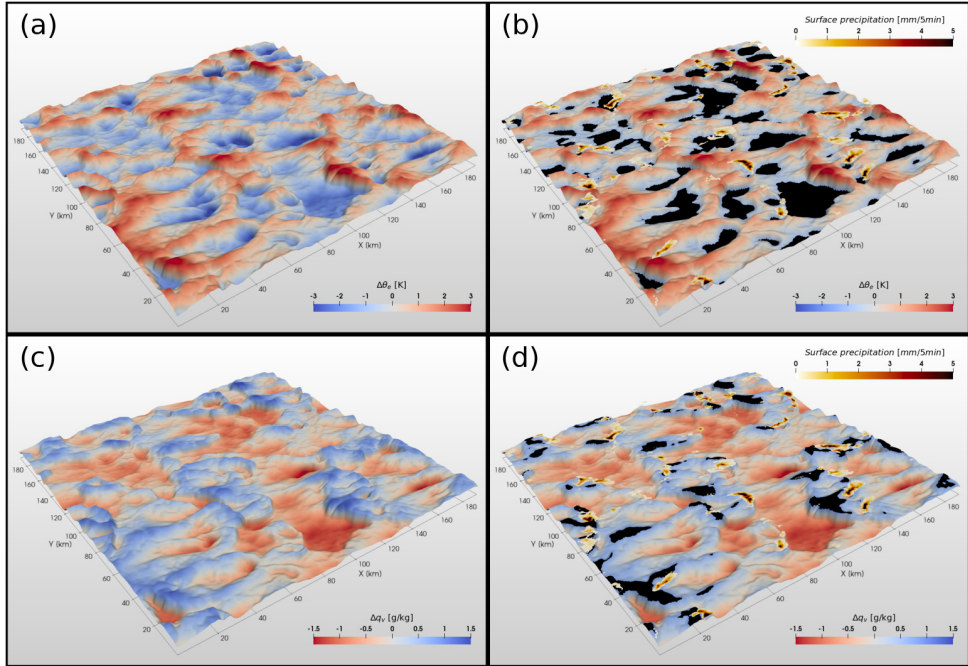
Figure 4.2: An illustration of the clustering of $\Delta\theta_e$ to cold pools (a, b) and Δq_v to moist patches (c, d). Left panels show the plain $\Delta\theta_e$ and Δq_v fields after 18 hours simulation time. Identified cold pools and moist patches are overlaid in black in the right panels. Note that, in addition to the color mapping, the 2D fields are warped by the values of the respective variable for an easy visualization of the steep gradients along cold pool and moist patch edges. An animated video (video animation V1) showing the temporal evolution of the low-level $\Delta\theta_e$ fields is available from the appendix.

Finally, we also apply the clustering technique to field anomalies of water vapor specific humidity, Δq_v, to detect relatively moist areas in the domain, called moist patches [Schlemmer and Hohenegger, 2016]. The same averaging and smoothing procedure is used as for $\Delta\theta_e$ is. The threshold for Δq_v is $0.75\,\mathrm{g\,kg^{-1}}$.

4.2.3. PRECIPITATION MEASURES, CHARACTERISTICS OF RAIN CELLS, COLD POOLS, AND MOIST PATCHES

We use domain averaged precipitation statistics for a first basic comparison of the different perturbation groups. We apply the same threshold as used for the rain cell clustering procedure. Thus, grid points with a rain rate less than $0.6\,\mathrm{mm\,h^{-1}}$ are considered as zero precipitating. For each time step, we calculate the domain averaged conditional precipitation rate P_r and the precipitation area fraction α. P_r is the mean rainfall rate over all grid points with precipitation in the domain, hence the term conditional. Zero precipitating grid points are excluded from the averaging process. α is defined as the number of grid point with precipitation divided by the total number of grid points in the domain. In

both cases, grid points with precipitation rates below the clustering threshold are considered as zero precipitating grid points.

The clustering algorithm allows the derivation of several metrics to describe the properties of rain cells, cold pools, and moist patches. The subscript i in the following definitions represents a single rain cell, cold pool, or moist patch. The linear size L_i of rain cell i is defined as the square root of the area A_i. Second, we calculate the average intensity of each cell $P_{i,r}$ by summing up the rain rates of all grid points belonging to a cell divided by their number. To capture the combined effect of rain cell area A_i and intensity $P_{i,r}$, we define $P_{i,car}$ which is the product of the area and intensity and, thus, the total amount of rain produced by a rain cell per unit time.

In order to characterize cold pool activity, we make use of two measures. First, the cold pool volume $C_{i,v}$ which is defined as the product of the cold pool area and its average θ_e anomaly. This gives a combined estimate of how large and deep cold pools grow and, at the same time, allows for an easier visual interpretation than each variable separately. For the sake of an easier visual interpretation, we drop the negative sign of $C_{i,v}$. Second, we derive the areal growth rate of a cold pool $C_{i,gr}$. This is done by matching overlapping cold pools in subsequent time steps and calculating the difference in area. Only cold pools that do not split in the next time step, and have not just merged, are considered (that is, only one forward link and zero or one back link in time). So area growth/decrease due to the merging or splitting of cold pools is excluded. To measure the growth of active cold pools, we restrict our analysis to those that grow in time and have an overlap with at least one rain cell.

The accumulation of low-level specific humidity in moist patches is measured in analogy to the cold pool volume. We therefore define the moist patch volume $M_{i,v}$ as the product of the moist patch area and its average Δq_v.

4.3. RESULTS

4.3.1. SIMULATION OVERVIEW

The applied perturbation strategies create a diverse set of experiments. A modification of initial temperature, lapse rate, relative humidity, and large scale convergence potentially influences several precipitation characteristics, for instance, the temporal evolution during the model day, rainfall intensities, and spatial properties of the precipitation field as well as individual events. In order to give an overview over the most fundamental differences between the experiment groups, we first focus on domain average precipitation statistics. Figure 4.3 shows the temporal evolution of the precipitation area fraction α and conditional rain rate P_r for the different groups.

The precipitation area fraction principally shows a similar temporal evolution for all experiments in all groups. Following an initial rapid increase after precipitation onset, the area fraction quickly decreases to a lower level for the rest of the simulation. In contrast to that the rain rate rather continuously increases. This behavior has been described in Lochbihler et al. [2019] and essentially indicates a transition from a state with widespread small-scale unorganized showers to a state with a more limited number of showers, that are larger, more organized and more intense.

Besides these general commonalities of the experiments, there is a number of dis-

tinct differences between the groups. First and most obvious, the modification of relative humidity alters the timing of the precipitation onset. While the increased relative humidity in the M4Krh experiment shifts the precipitation onset toward the beginning of the simulation, we find a postponed onset in the P4Krh run. The other experiments line up in between at nearly constant intervals. This is most likely the effect of a lower lifting condensation level due to the higher relative humidity in the colder runs of the RH (and RHL) group. The opposite is the case in warmer simulations. Another difference between the TEMP and RH groups is a reversed order of the experiments with the highest area fraction during the first hours after precipitation onset. In the TEMP group, the P4K experiment shows the highest area fraction while in the RH group the M4Krh experiment sits on top. In a later stage of the simulation, these differences virtually vanish.

Compared to the TEMP group the warmer experiments in the RH group show larger temporal fluctuations, indicative of more vigorous dynamics. Additionally, within the RH group the precipitation rates, after the onset of rain, spin up much faster in warmer experiments than in colder experiments and, in a similar way, temporal variability of the rain rate increases with warming. The large fluctuations of the area fraction and rain rate in the P4Krh experiment indicate short bursts of intense precipitation most likely caused by few but relatively large events; the smooth and steadily increasing rain rate in the M4Krh experiment on the other hand is symptomatic of numerous small, continuously emerging, and decaying events. According to Lochbihler et al. [2019], the enhanced temporal fluctuations in warmer runs can be traced back to a stronger stabilization of the atmosphere after precipitation rates peak. Subsequently, more time is needed until the prescribed large-scale convergence and surface fluxes refill the moisture deficit. The consequence is a more reduced rain activity after each burst of precipitation (see time series of CAPE and water vapor path in the Figures S4.3 and S4.4 in the appendix).

The temporal evolution of surface precipitation in the other groups follows very similar paths. In the same way as the RH group, the experiments in the RHL group show substantial shifts of the precipitation onset. The time difference is about five hours. However, in contrast to the RH group the initial precipitation area fraction for the P4Krhl experiment is higher than in the M4Krhl run. Nevertheless, just as in the RH group, both the increase in rain rate over time and the temporal variability are lower in the colder than in the warmer runs.

With an increased large scale convergence in the LS group, we observe a generally increased area fraction (compare dashed with solid lines). In the first hours after onset, this group shows the highest values of all experiments. The P4Kls60 experiment reaches a peak of 27%. However, the precipitation rate shows no significant difference when compared to the TEMP. Thus, we find that a modification of the large scale convergence predominantly alters the area fraction of precipitation and not its intensity. This is in accordance with Loriaux et al. [2017] who further hypothesize that an increased large-scale vertical lifting triggers convection easier at more locations in the domain, leading to a higher area fraction but not necessarily higher precipitation rates per event.

A modification of the lapse rate has a small impact on the timing of precipitation onset. As expected, more stable conditions (in terms of lapse rate) slightly delay the onset and first peak of precipitation (as in P4Klps50 and P4Klps100), whereas the more unstable condition in the colder runs lead to slightly earlier onset of precipitation. In the
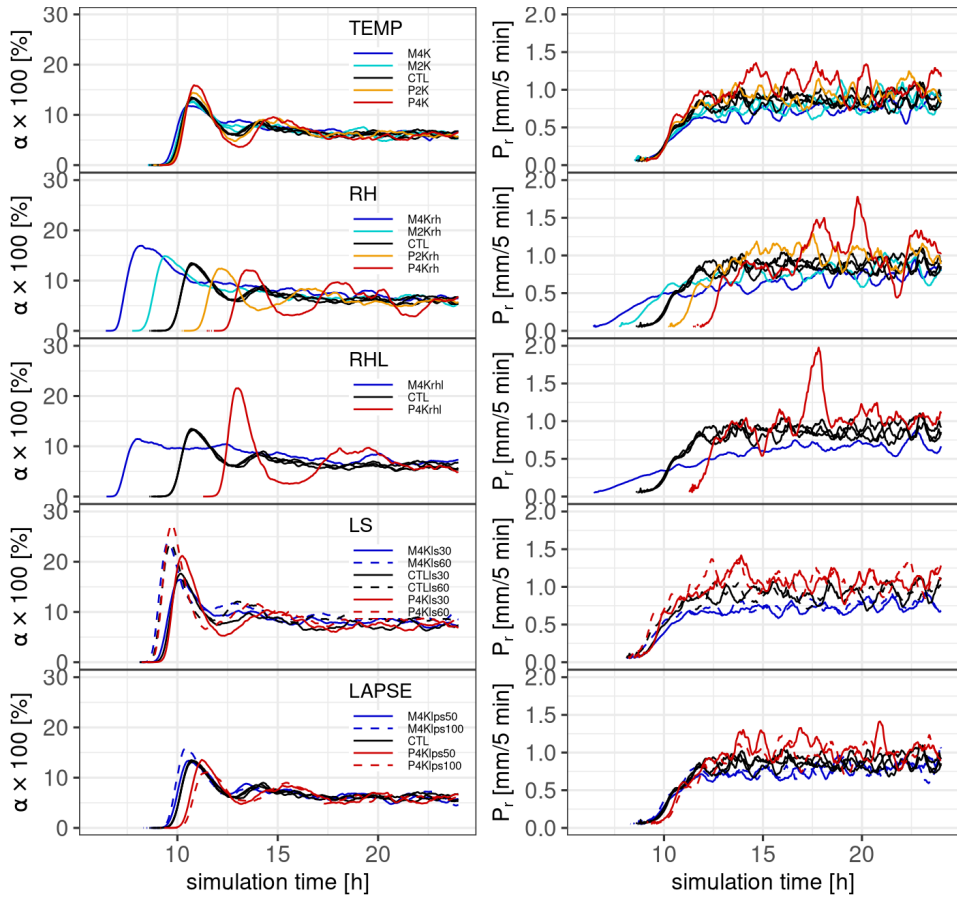
Figure 4.3: Time series of precipitation area fraction α (left panels) and conditional precipitation rate P_r (right panels). Each panel, from top to bottom, shows one specific perturbation group together with the control simulation.

most extreme experiments (P4Klps100 and M4Klps100), we find a reduced/increased precipitation area fraction in the first few hours after onset. The remaining part of the simulation in the LAPSE group shows no significant difference of area fraction between the experiments. Apart from this the precipitation rate increases from the coldest to the warmest experiments.

While domain averaged rain statistics reveal some basic properties of the response of the different experiments, they do not reveal the rain cell properties very well. In order to investigate rain cell properties in the next sections, and how they relate to the cold pool properties, we pooled data over a sufficiently long time window of the simulation. As found in Lochbihler et al. [2019], in the course of the simulation, the precipitation field undergoes significant changes from many small cells to fewer but bigger events. Since we are particularly interested in the characteristics of convective precipitation in a more organized state, we choose to sample only events from a time window at a later stage of the simulations. Due to the obvious timing differences, we set the sampling interval relative to the time of precipitation onset. More specifically we use only data between 3 h after onset until 9 h after onset. This way we avoid a pollution of the statistics with data from around the first peak of precipitation area fraction where almost all rainfall events are of type small single-cell convection. Furthermore, the 6 h length of the time window guarantees a sufficient amount of precipitation events even for the RH and RHL groups. This choice proves robust even when choosing a different start for the analysis time window (compare Figure 4.5d and Figure S4.5).

4.3.2. INTENSITY AND SIZE OF RAIN CELLS

Figure 4.4 shows the empirical cumulative distribution function (ECDF) of cell size and intensity for the experiments in the TEMP group derived from the 6 h time window. It illustrates that the size of large rain cells (> 95th percentile) increases with temperature from the M4K to the P4K experiment. Below the 95th percentile threshold, cells are smaller in colder runs compared to warmer experiments. The same observation can be made for the intensity of rain cells (Figure 4.4b).

Since we are particularly interested in the most extreme and largest events, and at the same time, aim at comparing all experiments in all groups, we chose to calculate a high percentile from the distributions of cell size and intensity and use this percentile in further analysis. For this purpose, we choose the 99.5th percentile which is beyond the pivot point (95th percentile) but not yet prone to be polluted by outliers and therefore poor statistics. The 99.5th percentile is marked by a black vertical line in Figures 4.4a and 4.4b. Despite the fact that other percentiles deliver very similar results (see Figure S4.5), we find that this choice provides the best compromise with respect to the varying sample sizes between the different experiments.

Figure 4.5 shows the results of this analysis. Since at first sight the results of all experimental groups may be overwhelming, we introduce this plot by separating out the results of the different experiment groups here. Figure 4.5a compares the TEMP and LS groups. With focus on the x-axis, it becomes clear that for both groups one can observe an increase of rain cell intensity from the coldest to the warmest experiments. Concurrently, rain cells grow in size. However, the enhanced large scale convergence in the LS group seems to generally only increase the rain cell size while cell intensities remain vir-
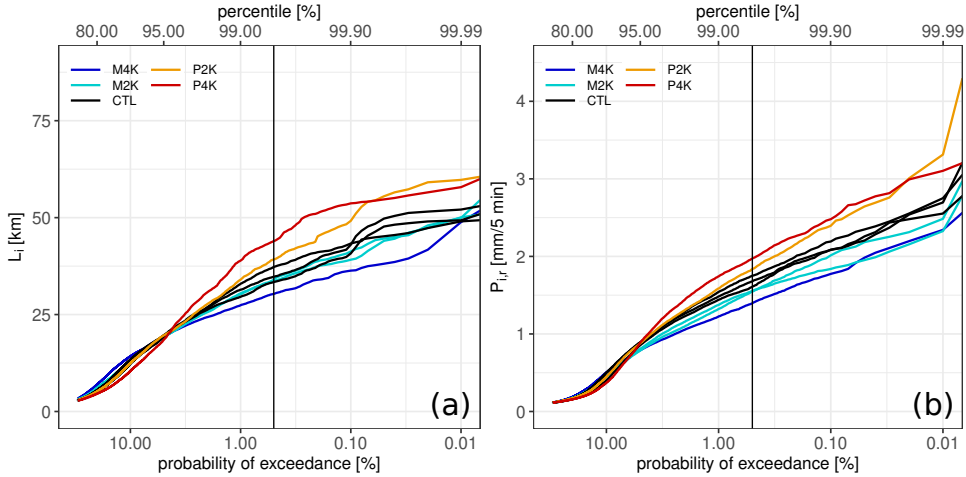
Figure 4.4: Probability of exceedance for rain cell size L_i (a) and average intensity $P_{i,r}$ (b) for the experiments of the TEMP group. Top axis shows corresponding percentiles. The 99.5th percentile is marked by a black vertical line.

tually the same as in the TEMP group. This appears as a vertical shift, as indicated by the arrows in Figure 4.5a. In essence, this resembles the domain wide increase of precipitation area fraction as described in the previous section, see also Figure 4.3. We note that these results contradict the theory that the higher area fraction is caused by a larger number of events of roughly the same size, as speculated by Loriaux et al. [2017].

The response to stability changes in the LAPSE group with respect to the standard group, TEMP, is less univocal.While the full adiabatic perturbations, M4Klps100 and P4Klps100, are on a clear trajectory toward the CTL setup (see arrows in Figure 4.5b), the intermediate experiments, M4Klps50 and P4Klps50, have a less unique direction. Nonetheless, in the first case, it can be concluded that cell intensity and size are eventually both affected by this perturbation setup.

In case of the perturbations of the relative humidity, the RH and RHL groups, there are multiple aspects (Figure 4.5c). First, although there is no increase of rain cell intensity from the P4K to the P4Krh experiments, the rain cells are larger in the latter case (red vertical arrow). This is particularly interesting since these experiments have the same amount of water vapor in their initial profiles and differ only in temperature and thus relative humidity (see Figure S4.4). The opposite behavior can be observed in the case of the M4K and M4Krh experiments: cell intensity decreases while the size remains nearly the same (blue horizontal arrow). In between, the P2Krh experiment shows a different behavior. Compared to their equivalents from the TEMP group cell size and intensity increases. Even more, both cell size and intensity increase to a point that are almost equal to the ones in the P4K experiment. This means, that a slightly lower relative humidity can boost precipitation intensity and event size to an equivalent level as in a considerably moister and warmer situation. The opposite behavior can be observed for the M2K and M2Krh experiments. The diagonal arrows in Figure 4.5c illustrate the described shifts.

4
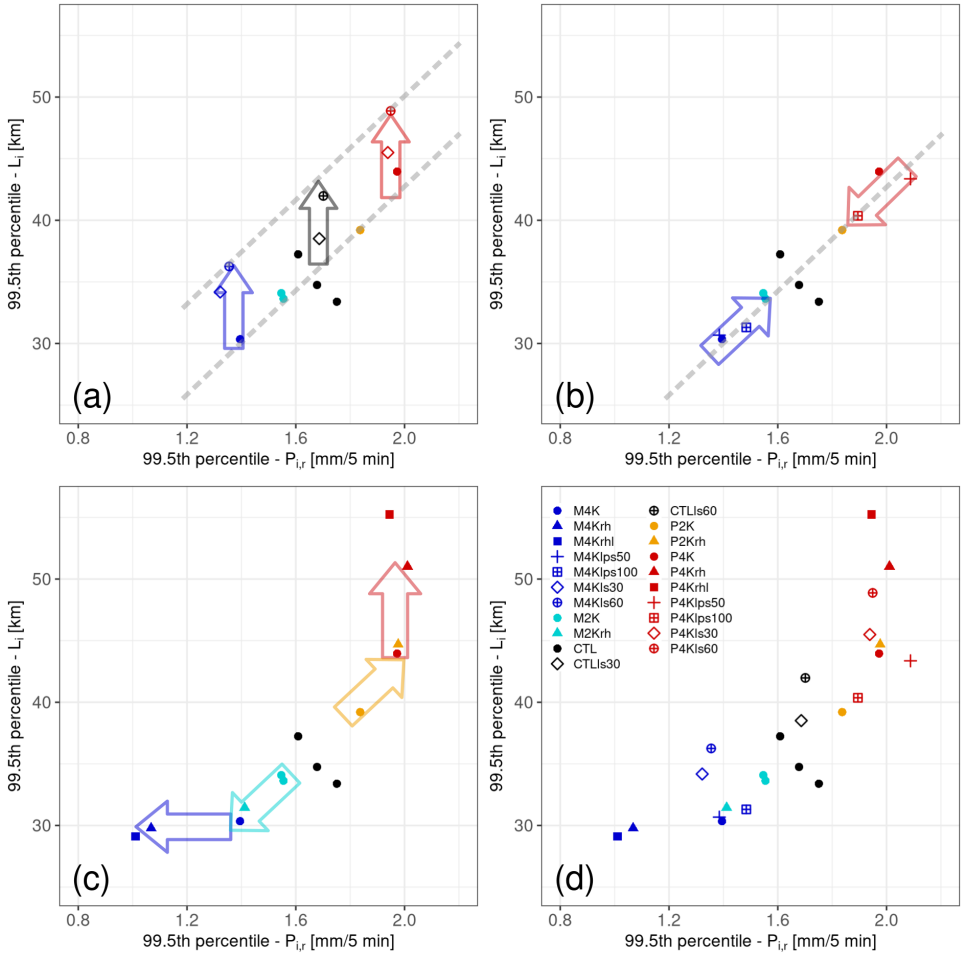
Figure 4.5: The 99.5th percentile of cell average intensity $P_{i,r}$ versus rain cell size L_i. Panel a shows the TEMP and LS groups, b the TEMP and LAPSE groups, c the TEMP, RH and RHL groups. All groups together are depicted in d. Arrows illustrate relative changes with respect to the TEMP group (see text).
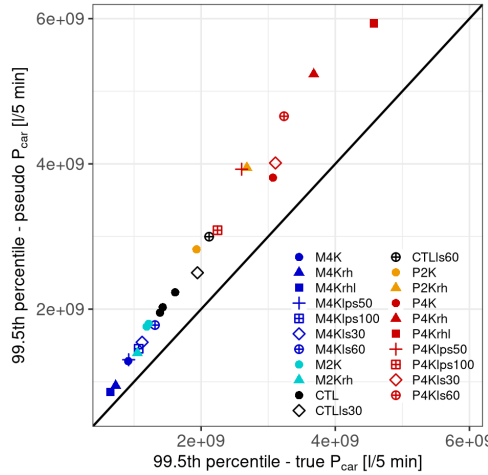
Figure 4.6: A comparison of the product of the 99.5th percentiles of cell intensity and area (pseudo P_{car}) and the true value of the cell-aggregated rain rate (true P_{car}).

The response of cell intensity and size in the RHL group seems to follow a similar path although the signal is stronger for the colder runs than for the warmer experiments. We note that enhanced warming only near the surface also changes the atmospheric stability compared to RH group where warming is applied to the whole atmospheric column (compare CAPE time series in Figure S4.3). This complicates interpretation. Also, we can not identify a reason for the upper and lower bounds on $P_{i,r}$ and L_i. We conclude that changes in relative humidity have quite strong impacts on cell size and intensity. Surprisingly, a lower relative humidity with warming leads to bigger/more intense cells, and vica versa.

In the proceeding we will relate the rain cell properties to cold pool properties. To do so, we will take the product of rain cell area and intensity, and call this measure the cell-aggregated rain rate P_{car}, which is the total amount of rain per unit time. From the previous results it is already clear that rain cell intensity and size are well related, but it is not so clear whether the product of the 99.5th percentiles of intensity and area gives a good measure of the 99.5 percentile of cell aggregated rain rate. Therefore, Figure 4.6 shows the product of the 99.5th percentile of cell area and average intensity (pseudo P_{car}) in relation to the true value of the 99.5th percentile of P_{car}. Despite a slight deviation from the diagonal, both quantities linearly increase from the coldest to the warmest experiments. This shows that the separate contributions of cell size and intensity to P_{car} systematically add up across all simulations. This is even closer to unity at lower percentiles (see Figure S4.6).

Using P_{car} as the rainfall statistics, we investigate its relation with the cold pool properties. This will be done in two separate parts. First, we concentrate on how rainfall affects cold pool dynamics. In the second part, we investigate how cold pool dynamics alter the variability of the low-level moisture field and how this could feed back to the rainfall statistics. We note that obviously these two are intertwined forming a feedback

loop, yet for means of simplicity and physical understanding we present both parts separately.

4.3.3. COLD POOL ACTIVITY IN RESPONSE TO RAIN ACTIVITY

We make use of two quantities related to cold pool activity. While cold pool volume measures the combined effect of the area and depth of cold pools, the growth rate indicates the speed at which active cold pools spread. Again, a percentile from the distribution of the cold pool property (growth and volume) is chosen similar to rain cell precipitation. Here, we chose the 95th percentile, which is lower than the 99.5th percentile for rain cell statistics. Since precipitation precedes the formation of a cold pool and cold pools without an associated rain cell are excluded from our analysis, sample sizes are even smaller than those for rain cells. Only selecting cold pools with increasing size, as we do in the case of cold pool growth rate, further shrinks sample sizes. Under these circumstances, we chose the 95th percentile. Testing has shown that the 95th percentile captures the most extreme cold pools in all experiment groups while still guaranteeing a robust estimate despite the varying sample sizes.
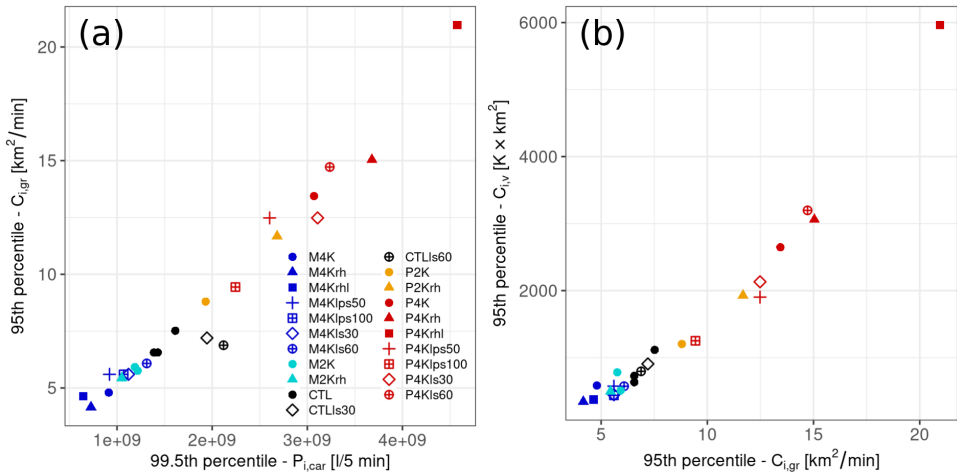
Figure 4.7: Cell-aggregated rain rate $P_{i,car}$ in relation to cold pool growth rate $C_{i,gr}$ (a) and cold pool growth rate compared to cold pool volume $C_{i,v}$ (b).

Since evaporation of rain is the primary driver for cold pools, we start by looking at the relation between the rain produced by a cell ($P_{i,car}$) and cold pool growth rate ($C_{i,gr}$), see Figure 4.7a. Assuming that the evaporation is proportional to the rain cell rain rate, we expect a good correlation. Indeed, a very strong relation is found between $P_{i,car}$ and cold pool growth rate, with data almost on a straight line (through the origin). In general, larger and stronger precipitating rain cells cause faster spreading cold pools. However, the strength of the response depends on the initial temperature. $C_{i,gr}$ and $P_{i,car}$ rather weakly increase with initial temperature in the coldest simulations. Those experiments are densely packed in the lower left corner of Figure 4.7a. In warmer simulations, we find that the spread increases the higher the temperature.

Looking specifically at the TEMP group, we find that cold pool growth rate continuously and strongly increases with higher temperature and moisture availability from the M4K to the P4K experiment. The stronger large scale convergence in the LS group virtually has no additional effect on the cold pool growth rate when compared to the TEMP group despite the presence of larger rain cells (see Figure 4.5a). In the LAPSE group, the previously described trajectory from the corresponding experiments in the TEMP group toward the CTL run appears to be a persistent feature: Cold pool growth rate decreases along with rain cell-aggregated rain rate from the P4K to the P4Klps100 experiment and vice versa from M4K to M4Klps100. The RH and RHL however respond differently in terms of the cold pool volume. The experiments in both groups show, in relation to their partners in the TEMP group, a further amplification of the signal. For instance, $C_{i,gr}$ further increases from the P2K to the P2Krh and from the P4K to the P4Krh experiments. The P4Krhl experiment has the fastest spreading cold pools. Cold pool growth rate in the M2Krh, M4Krh and M4Krhl experiments responds the opposite way, although the signal is rather weak in this case. We therefore conclude that evaporation of precipitation, the main driver of cold pools, further increases at decreased relative humidity and, thus, leading to stronger cold pools at comparable rainfall intensity in an atmosphere which is closer to saturation (e.g., compare P4K and P4Krh experiments).

Due to the nature of cold pools which are essentially density currents, one would expect that faster spreading cold pools are associated with a stronger and more spacious θ_e anomaly. Figure 4.7b confirms this relation. Cold pool volume - the product of the average θ_e anomaly and the area of a cold pool - linearly increases with cold pool growth rate, and therefore with the initial temperature of the different simulations. Again, the rate of increase with initial temperature is lower for colder simulations than for the warmest. Particularly the warmest experiments in the RH and RHL groups exhibit a strong increase when compared to the TEMP group. The damping effect of a more stable atmosphere on the warmer side of the LAPSE experiments is also reflected here in form of smaller and weaker cold pools which eventually spread slower.

4.3.4. Low-level moisture and rain activity in response to cold pool activity

One of the key characteristics of laterally spreading cold pools is that they create a divergent wind field near the surface, and areas of convergence at the cold pool fronts and where different cold pool collide [Schlemmer and Hohenegger, 2014]. Given the presence of multiple cold pools in different locations, this eventually leads to confined regions with strongly enhanced moisture content (see Figure 4.2).

We quantify these relatively moist regions in the domain by the product of their average moisture content and area, called moist patch volume. In analogy to previous figures, we draw a high percentile from the distribution of moist patch volume for all experiments. We chose the 95th percentile since sample sizes are relatively small compared to rain cells.

A direct comparison with cold pool volume, see Figure 4.8a, illustrates the effect of cold pool activity on the low-level moisture field. Warmer conditions generally lead to larger moist patches of higher moisture content. Moist patch volume is roughly four times higher in the P4K experiment than in the M4K run. The effect is, however, stronger
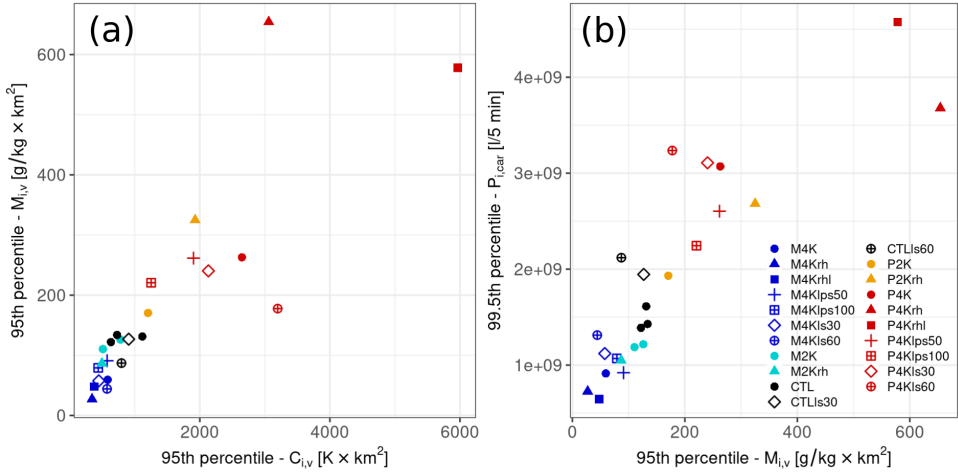
Figure 4.8: The 95th percentile of cold pool volume $C_{i,v}$ compared to moist patch volume $M_{i,v}$ (a) and moist patch volume compared to cell-aggregated rain rate $P_{i,car}$ (b).

for simulations warmer than CTL. Colder model runs are densely packed together at relatively low moist patch volumes. In particular the relation with cold pool volume reveals that small, shallow and, thus, slowly spreading cold pools in the coldest simulations create moist patches which barely emerge above the average q_v field. For instance, the M4Krh simulation stands out with very small cold pool and moist patch volumes. In contrast to that, the warmest simulations in the RH and RHL groups have, by far, the highest moist patch volume. Compared to the TEMP group, amplified cold pools due to a reduction of relative humidity boost the accumulation of moisture in confined regions. Lower precipitation amounts due to increased stability in the P4Klps100 experiment lead to weaker cold pool activity and eventually to a slightly smaller cold pool volume as in the corresponding simulation from the TEMP group (and vice versa for the M4Klps100 experiment). Interestingly, the strongly enhanced large scale convergence in the CTLls60 and P4Kls60 experiments seems to reduce the moist patch volume. The reason for this behavior is not completely clear since there is virtually no change in cold pool activity (with respect to the TEMP group). Even more, the slightly increased cold pool volume and growth rate in the P4Kls60 experiment suggests the formation of wetter and larger moist patches. Thus, we speculate that the applied threshold for the moist patch clustering plays a role in this case. A strong uniformly applied moisture tendency through large scale convergence causes the domain averaged specific humidity q_v to increase. This average is mostly dependent on grid points outside moist patches (see Figure 4.2). A threshold of $0.75\,\mathrm{g\,kg^{-1}}$ might then be too high which potentially leads to relatively smaller moist patches after the clustering with eventually lower moist patch volume.

To examine how a concentrated accumulation of moisture through cold pools feeds back to precipitation amounts Figure 4.8b depicts the relation between moist patch volume and cell-aggregated rain rate. We find that increased moist patch volume at higher temperatures correlates well with enhanced rain cell intensity and size. The previously

described tendencies in each perturbation group hold well in this context. For instance, the experiments in the TEMP group reveal a strongly linear correlation between moist patch volume and cell-aggregated rain rate. When compared to the RH and RHL groups, reduced relative humidity leads to higher precipitation amounts inside rain cells (and vice versa). The LAPSE group confirms that when the temperature perturbation approaches a moist adiabat, and therefore stabilizes the atmosphere, attenuates the signal in comparison with the TEMP group. In the case of the LS group, despite increased cell-aggregated rain rates, we find no further increase in moist patch volume when compared to the TEMP group.

As a final remark, we note that, despite there is a clear relation between cold pool activity, moist patch volume, and rain event intensity, the described processes are intertwined and progress concurrently, possibly at different stages. This limits the ability to derive a direct causality from the presented statistics alone. However, it has been shown that new deep convective clouds form at locations of elevated moisture, of which a substantial part stems from the advection through cold pools [Schlemmer and Hohenegger, 2016]. This link is further strengthened in a more recent study by Fuglestvedt and Haerter [2020]. They use a backtracking approach to identify cold pools as moisture conveyors for newly emerging deep convective clouds. In a more qualitative way, this process can be observed in video animation V1 where "waves" of warm and moist low-level air masses with high θ_e at the cold pool fronts "disappear" at locations where new rain cells appear slightly later.

4.4. CONCLUSION

In this study, we examined the impact of various atmospheric perturbations, which are relevant in the context of climate change, on the characteristics of rain in convective cloud systems. To this end, we created a set of high-resolution large eddy simulations for a typical convective event at midlatitudes over a range of dew point temperatures, and in addition, groups based on accompanying changes in relative humidity, temperature lapse rate, and large-scale convergence. With this set of experiments aimed to represent different climatic conditions, we examined how, and to which extent, cold pools relate to rain cell size and intensity.

A general conclusion for all experimental groups is a general increase of intensity and size of precipitation events with higher temperatures. The warmest simulations show the strongest signal. However, the details of the response in each experimental group differ. For instance, we find that enhanced large-scale convergence under warmer conditions (LS group) only increases event size when compared to the latter alone (TEMP group). A stabilization of the atmosphere under warmer conditions according to a moist adiabat (LAPSE group) hampers the development of intense rain events under warmer conditions and, thus, weakens the signal when compared to a vertically uniform warming (TEMP group). Finally a modification of the relative humidity with warming (RH and RHL groups) bears the strongest response of intensity and size of rainfall events. However, this comes at the cost of number of events due to a later onset of precipitation in the course of the simulations. In other words rain events become more rare but their extremes increase at a much higher rate when compared to a constant relative humidity

perturbation (TEMP group).

Cold pool activity concurrently increases with stronger and larger rainfall events under warmer conditions, confirming results in Haerter and Schlemmer [2018]. A very strong relation between the aggregated rain rate of extreme cells and the growth rate and size of cold pools is found, unifying all experiments onto an almost single curve relating rain rate to the cold pool statistics. In this case, the warmer runs with decreased relative humidity lead to the largest cold pools. Thus, we can identify two fundamental factors in our simulations that control the magnitude of cold pool activity. First, higher precipitation rates enable more evaporation of rain drops. This enhances the cooling rate of air masses which eventually form the cold pool. Second, a reduced relative humidity causes enhanced evaporation of rain drops at similar precipitation rates. The combined effect of these processes causes the warmer experiments with lower relative humidity to have the strongest response in cold pool dynamics.

Reversely, cold pool dynamics appear to influence local low-level moisture variability and subsequent rainfall formation, affirming Schlemmer and Hohenegger [2016], but now in a climate change context. Although the relation between cold pool statistics and moist patches – amount of excess moisture contained in confined, moist areas – appears less distinct, larger cold pools generally lead to larger moist patches. Subsequently, larger moist patches again translate into larger aggregated rain rates from rain cells. Physically, enhanced cold pool activity amplifies the advection of moisture into confined regions and this directly relates to intensified rainfall events. The most intense and fastest spreading cold pools are found in the warmest simulations. This enables moisture transport over longer distances and greater accumulation into moist patches. Again the warmest, lower relative humidity runs lead to the largest moist patches.

Concluding, we showed that cold pools play a crucial role in shaping the response of convective rain extremes in a large set of simulations, representing different climatic conditions. In general, cold pool dynamics increase in warmer conditions, and we speculate that this feedback loop might play an important role explaining deviations from the CC-scaling in the response of rain extremes to global warming. Yet, we also note that the stabilization of the atmosphere (according to a moist adiabatic lapse rate) appears to dampen feedback from cold pool dynamics but on the other hand projected decreases in relative humidity appear to strongly amplify their influence. Further investigating these feedback processes, preferably also in different modeling setups, is therefore highly recommended.

Acknowledgments

APPENDIX

DATA AVAILABILITY

A data set with the DALES case setup is available at https://doi.org/10.4121/13241072, the video animation V1 from https://doi.org/10.4121/13241081, and the software used for clustering can be found under https://doi.org/10.4121/13241102.
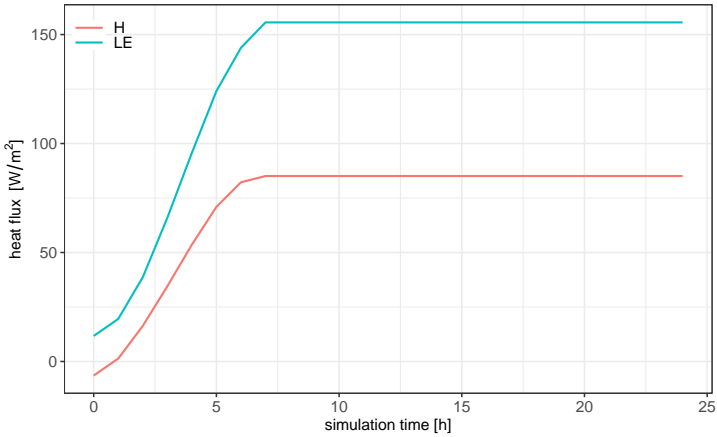
FIGURES

Figure S4.1: Time series of the prescribed sensible (H) and latent (LE) heat fluxes.
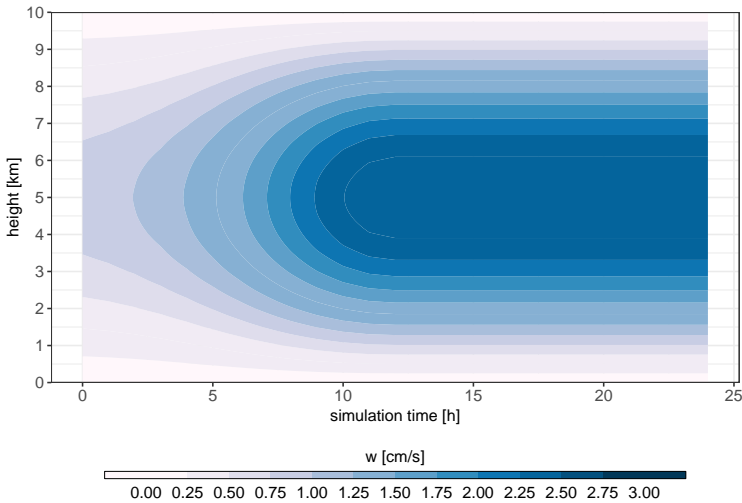
Figure S4.2: Time height plot of the prescribed large scale vertical velocity.
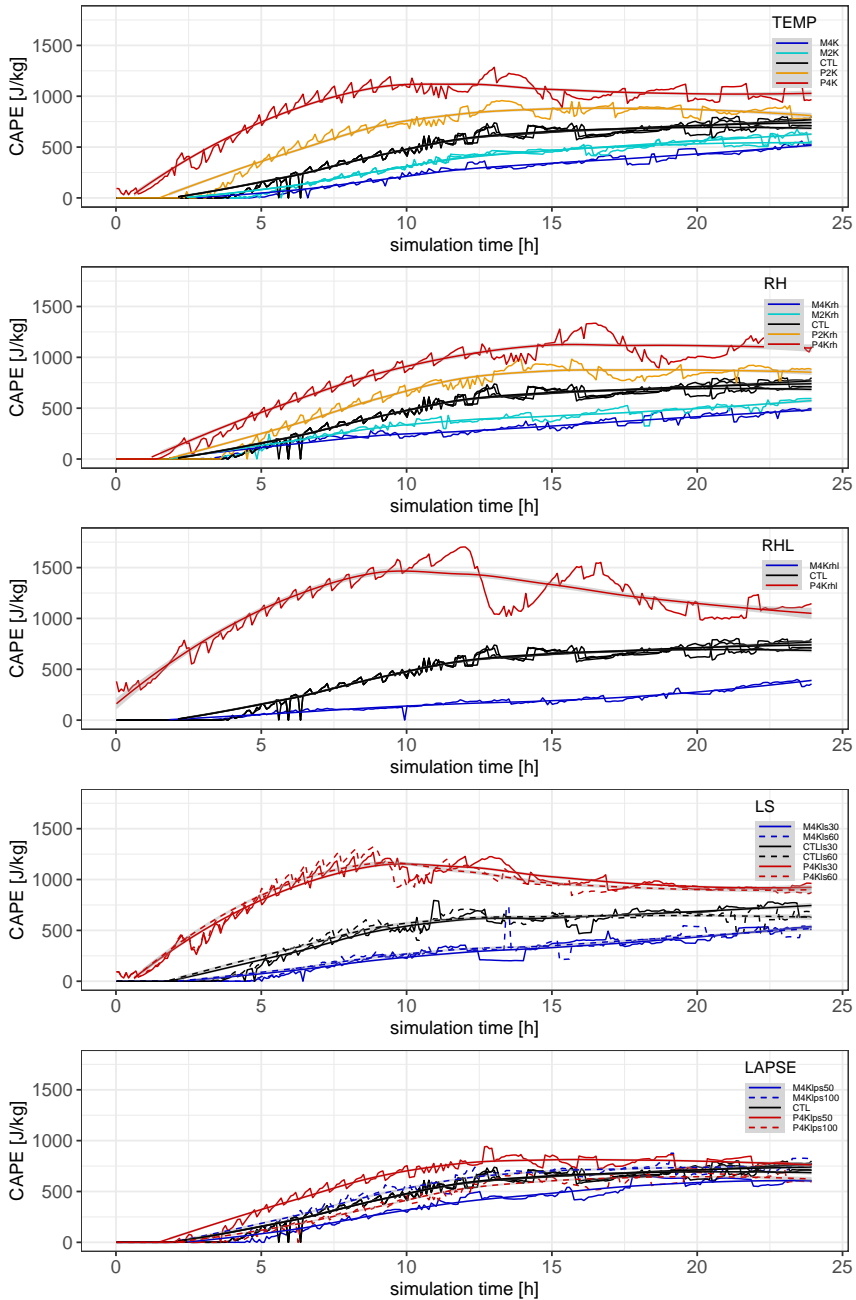
Figure S4.3: Time series of the domain average CAPE for all groups.
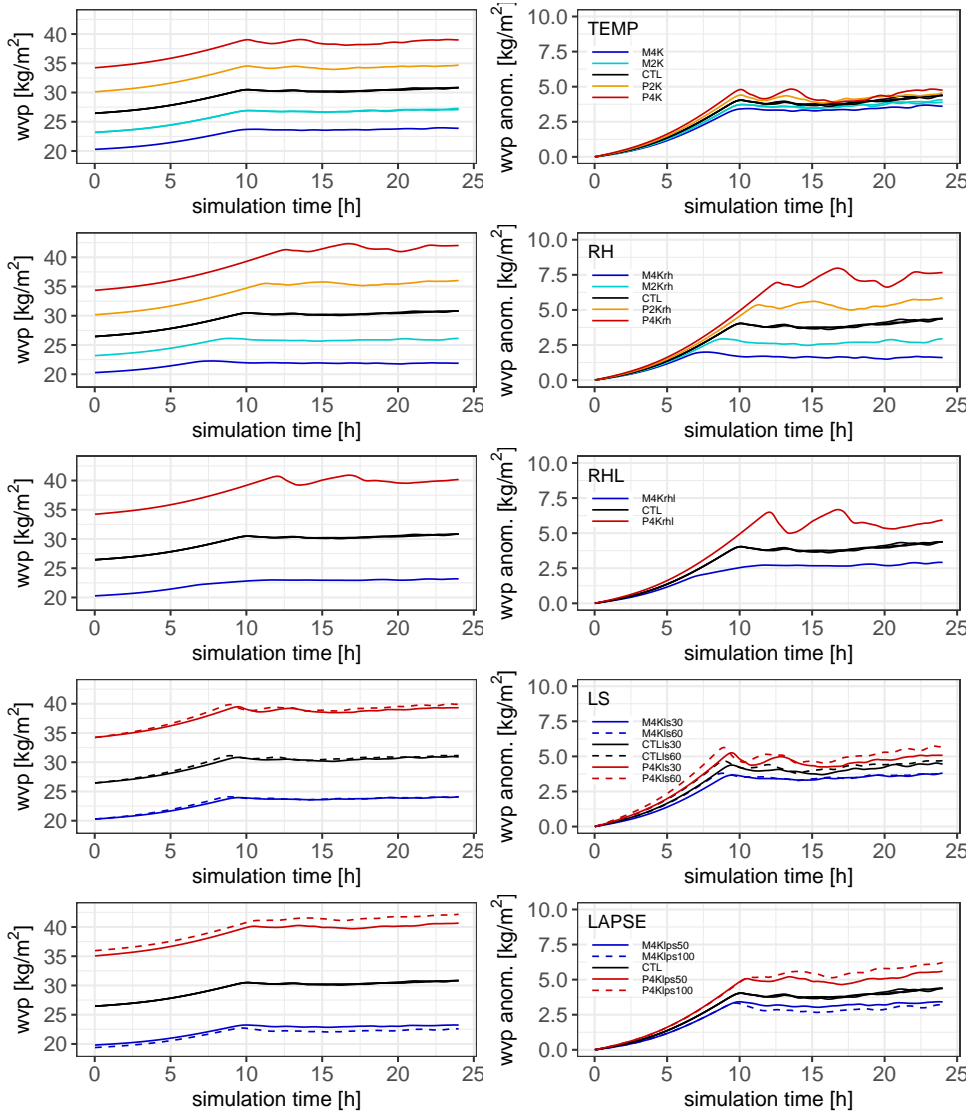
Figure S4.4: Domain average time series of water vapor path (wvp) in absolute values (left) and relative to the beginning of the simulation (right). Each row represents one perturbation group.

4

4
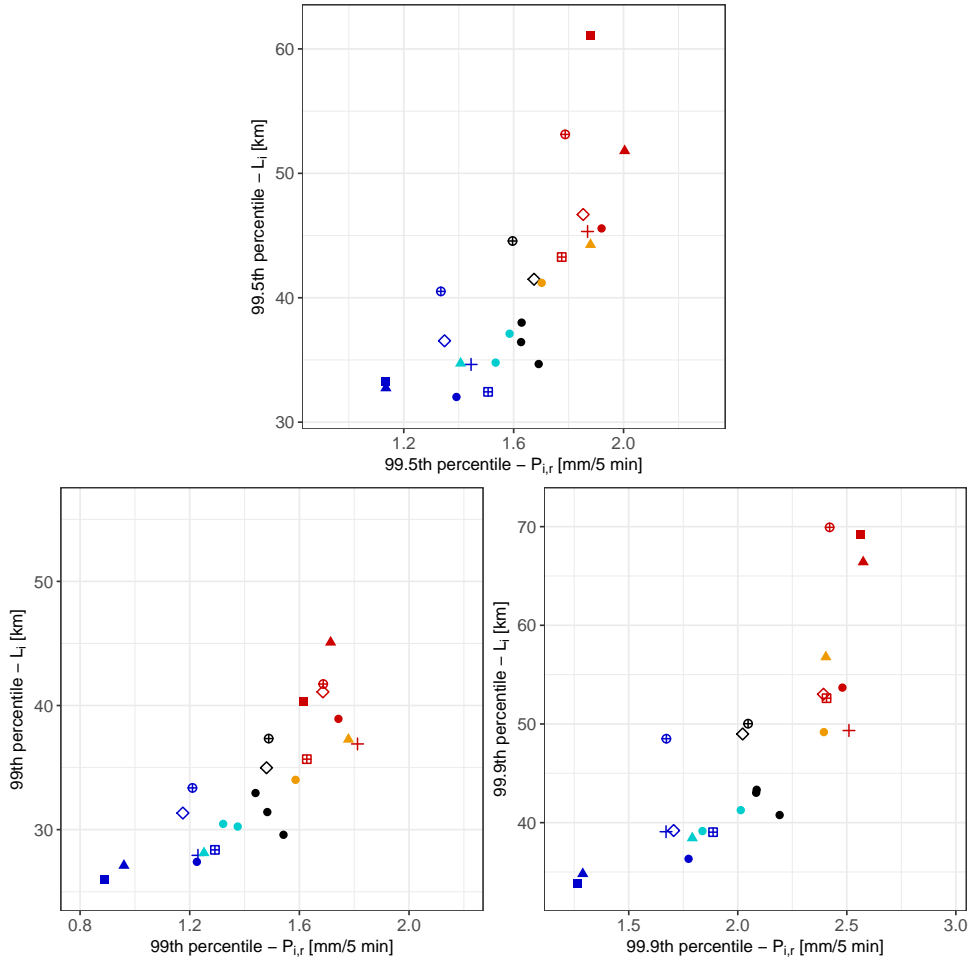
Figure S4.5: Statistics of cell average intensity $P_{i,r}$ versus rain cell size L_i. The top shows the 99.5th percentile sampled from rain cells between five to eleven hours after precipitation onset. Plots in the bottom row are for the same time interval as in Figure 5 from the main text but use the 99th (left) and 99.9th percentile (right).
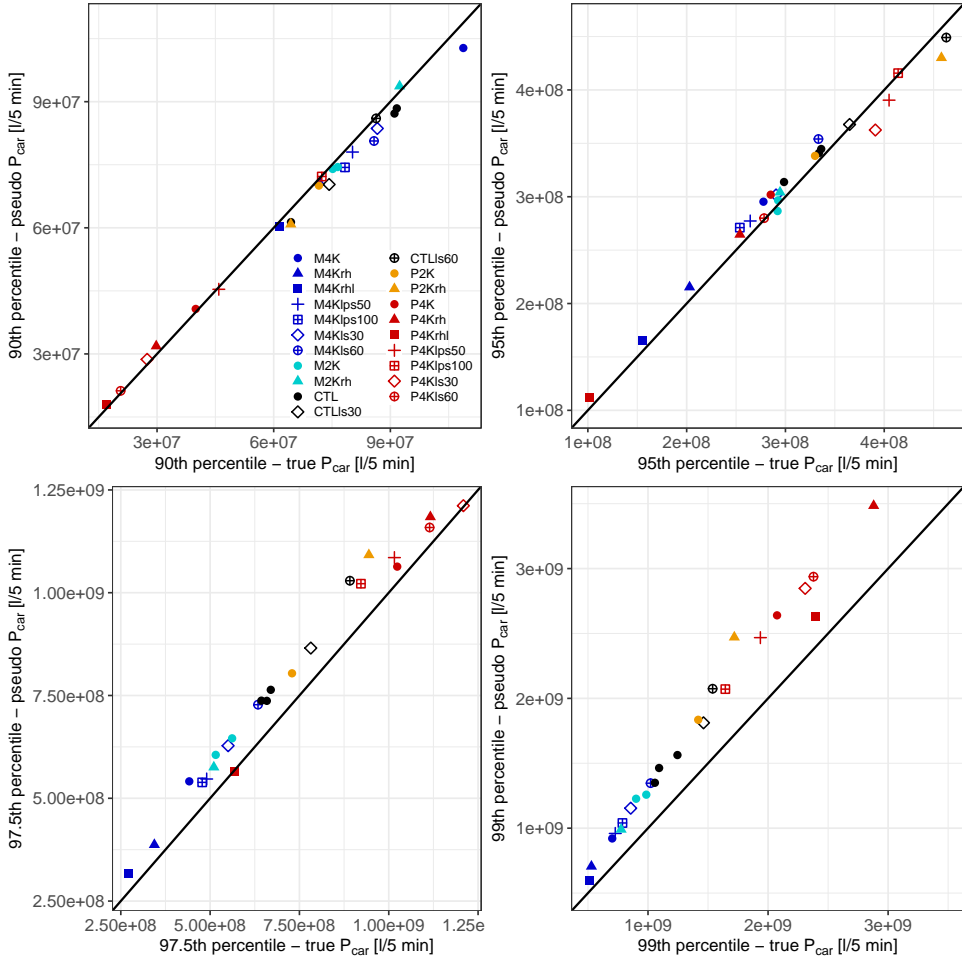
Figure S4.6: A comparison of the product of various percentiles of cell intensity and area (pseudo P_{car}) and the true value of the cell-aggregated rain rate (true P_{car}). Note that the order of the experiments changes from lower to higher percentiles. This reflects the pivot point (approx. at the 95th percentile) in Figure 4 in the main text.

5

CONCLUSIONS AND OUTLOOK

The main goal of this thesis was to gain a better understanding of convective precipitation extremes under changing atmospheric conditions. We did this under the umbrella of the three questions, posed in the introduction of this thesis;

1. *What is the relation between size and intensity of convective precipitation extremes in a warmer and moister atmosphere?*

2. *What is the role of cold pools for the size and intensity of convective events?*

3. *How are convective precipitation extremes affected by a broader set of climate perturbations?*

This chapter presents the conclusions with respect to these questions and a brief outlook.

5.1. CONCLUSIONS

1. What is the relation between size and intensity of convective precipitation extremes in a warmer and moister atmosphere?

Chapter 2 contains an analysis of spatial properties and intensities of small-scale convective precipitation events. This analysis is based on rain radar observations to which we applied a rain cell tracking algorithm to extract properties of events at their maximum intensity. Each event is then paired with the observed dew point temperature at the closest station. The results reveal a clear correlation between the size of rainfall events and their intensity. Higher intensity events are generally larger. This correlation is consistent over a wide range of dew point temperature. Besides, we find that event size rapidly increases at the highest dew point temperatures observed. The beginning of this acceleration is roughly at 15 °C.

Chapter 2 also shows that there is a clear size dependency of the scaling of precipitation extremes with dew point temperature. As long as all events are included in the analysis intensities of the most extreme events clearly exceed the CC-scaling rate of about

7 %°C^{-1}. The scaling rate increases to up to 13 %°C^{-1} if only larger events are included. Smaller events have much lower scaling rates or even follow the CC-scaling rate. Larger events are essential to sustain super CC-scaling above 15 °C.

The evidence for the bond between event size and intensity is further strengthened by the high-resolution simulations of heavy summertime precipitation in chapter 3. The outcomes of these idealized yet realistically forced simulations confirm the observation-based results that more intense events generally are larger in size. Moreover, size and intensity jointly increase with surface dew point temperature. Warmer and moister conditions also let precipitation events grow faster and, eventually, larger over time.

Finally, the spatial composites of extreme rain events in chapters 2 and 3 show that along with the size increase higher intensities can be found over a large part of the rain cell area. This indicates that the amplification of rainfall rates is not the result of a redistribution of moisture toward the center of convective events but rather a consequence of enhanced mesosale dynamics.

2. *What is the role of cold pools for the size and intensity of convective events?*

The LES simulations in chapters 3 and 4 use almost identical case setups and share a common set of perturbations with increasing temperature and moisture availability. In chapter 3, we find that increasing dew point temperature reshapes the size distribution of rainfall events. More specifically, the results show that the number of larger events increases at the cost of many smaller events. Warmer and moister conditions thus favor the development of fewer but larger rain events. Additionally, we find indications of a coarser but stronger net of positive low-level vertical velocity that is related to cold pool fronts. Or in other words, regions of low-level convergence are stronger but the distance between them increases. This suggests an intensification of near-surface dynamics through cold pools alongside with the development of larger rainfall events.

The subject is further investigated in chapter 4 by looking at statistical properties of cold pool activity. This is done by clustering field anomalies of equivalent potential temperature ($\Delta\theta_e$) to continuous, relatively cold and dry areas, a distinctive property of cold pools. Based on that, we find that cold pools, in warmer simulations, are not only larger in size but also exhibit a stronger $\Delta\theta_e$ anomaly which correlates well with increased rain cell size and intensity. Moreover, the areal growth rate of cold pools increases under these conditions. These findings draw a consistent picture since cold pools are density currents driven by gravity. This indicates that enhanced cold pool activity leads to stronger low-level dynamics.

Recent studies have highlighted that cold pool dynamics can modify the low-level moisture field through advection [Schlemmer and Hohenegger, 2014, 2016]. We tested how this process changes in our simulations by clustering near-surface specific humidity field anomalies (Δq_v) into continuous areas of elevated moisture, so called moist patches. The product of average Δq_v and the area of moist patches increases with dew point temperature and correlates well with increased cold pool activity. This leads to the conclusion that warmer and moister conditions cause larger and faster spreading cold pools which amplify the advection of moisture into confined regions. Finally, we close the circle with an analysis of the relation between moist patches and rain cell intensities. The results show that rain event intensity and the amount of moisture accumulated in

moist patches are strongly correlated.

In summary, we found convincing evidence that the size and intensity of rain events increase hand-in-hand with cold pool activity and the accumulation of moisture inside moist patches. Despite the fact that these correlations do not prove a causality, we propose that they form a feedback loop that can, at least partially, explain super CC-scaling behavior.

3. How are convective precipitation extremes affected by a broader set of climate perturbations?

In chapter 4, we simulate a number of LES experiments that mimic several aspects of the adjustments of the atmosphere to climatic warming. The response of the size and intensity of extreme precipitation events, cold pool activity and moist patches is analyzed subsequently.

Changes in relative humidity are applied in two different ways. First, uniformly with height (RH group) and, second, in the subcloud layer only (RHL group). The latter is found primarily in the context of extreme precipitation [Attema et al., 2014]. In both cases, we find similar impacts on the time of initiation and variability of rainfall rates. Precipitation starts later in warmer and relatively drier conditions than in colder simulations with higher relative humidity and intensities are stronger. Moreover, precipitation variability increases which indicates a fewer number of events. The size and intensity of extreme rainfall events show a much stronger response to decreased relative humidity with warming when compared to simulations with constant relative humidity. However, in the most extreme simulations event size further increases but intensities stall. Nevertheless, higher rainfall rates coincide with stronger cold pool activity and accumulation of moisture in moist patches. Two controlling factors can be identified here that drive cold pool activity, the precipitation rate and the saturation deficit of the air masses in which cold pools form. In conclusion, a warmer atmosphere with slightly decreased relative humidity can cause larger and more vigorous rain events than an even warmer setting under the assumption of constant relative humidity.

An imposed stabilization of the atmosphere with warming, following a moist adiabat (LAPSE group), leads to an overall weakening of the response of precipitation statistics. Besides that, the general relation between size and intensity of rainfall events with warming persists. However, in the same way as bulk statistics the response of size and intensity under these conditions is weaker than in the simulations with constant relative humidity. Cold pool activity and moist patches very much follow this tendency.

Finally, we performed experiments with enhanced large-scale convergence under warmer and moister conditions (LS group). Unlike in the other perturbation groups, size and intensity of rainfall events do not increase jointly in response to the changed large-scale conditions. Instead, a stronger large-scale moisture convergence only affects the size of events in that they grow in all cases. Cold pool activity and moist patches show no systematic behavior and the area integrated rainfall rate only increases due to the size growth.

In summary, the presented results draw a consistent picture of the inter-connection between the characteristics of rainfall events, cold pool activity and moist areas under various conditions. Whenever we find a jointly increasing rain cell size and intensity,

we observe stronger cold pool activity and a higher variability in the low-level moisture field. Small-scale cold pool induced dynamics, thus, play an important role for the intensification of convective precipitation extremes with warming.

5.2. Outlook

As it was mentioned in section 2.1 and more elaborately discussed in section 3.1 contradictory results on the size-intensity relationship of extreme precipitation events exist. Besides the outcomes, the mentioned studies differ in a variety of ways. Data sources range from model output [Prein et al., 2017] over rain radar data [Peleg et al., 2018] to station observations [Wasko et al., 2016]. Moreover, they use different identification methods for rain events. The methods to deduce changes in the size of rainfall events differ equally, for example, future climate scenarios or scaling with (dew point) temperature for present climate conditions.

While this thesis further enhances our understanding of the relation between the spatial extent and intensities of extreme convective events under different conditions the number of studies dedicated to this question remains low. On the observation side, future work must continue to exploit the potential of high-resolution gridded data. Relatively long time series of rain radar observations that cover large areas are becoming increasingly available. Examples are radar composites for the United States, provided by the National Oceanic and Atmospheric Administration (NOAA) or the pan-European radar product offered within the OPERA programme of EUMETNET. A standardized framework of data analysis and tracking methods, applied to these data sources, will enable a detailed investigation of size and intensity of extreme convective precipitation events, potentially alongside with other characteristics such as life cycle statistics. The fact that these data sets span a large variety of climates in midlatitudes will further improve our understanding of convective precipitation extremes.

The results in chapter 4 show that cold pool dynamics have a significant impact on the redistribution of near-surface moisture and that this correlates well with size and intensity of rainfall events. These findings were made possible by the use of high-resolution LES modeling. LES models provide the necessary spatio-temporal detail that is required by the small-scale nature of the involved processes. However, despite the realistically derived and forced case setup that was used in this thesis certain limitations remain. It is known that extreme convective events are accompanied by a significant large-scale convergence that depends on the magnitude of the event [Lenderink et al., 2017]. In our simulations the large-scale convergence is prescribed (due to the limitations of the employed LES model) and, thus, lacks the interaction with local convective activity. Including this feedback could improve the robustness of the results. Especially, since we found in chapter 4 that the large-scale convergence influences the size of rainfall events. Another limitation is the assumption of homogeneous surface conditions together with prescribed surface fluxes in the simulation domain. Even though the impact of surface fluxes on cold pool dynamics can be considered as minuscule [Fuglestvedt and Haerter, 2020; Schlemmer and Hohenegger, 2016], including them as an interactive component would increase the realism and strengthen the results. Lastly, although the simulation domain of our modeling experiments is rather large (approximately $200\,\mathrm{km} \times 200\,\mathrm{km}$),

it can not be ruled out that because of the horizontal double periodic boundaries deep convective events influence themselves across boundaries. Future LES studies should thus eliminate this possibility by introducing open horizontal boundaries with a realistic forcing. This could be done in a similar way as in regional climate models where a large-scale model provides input at the horizontal boundaries.

LES-based modeling studies of convective precipitation events should be continued, since it is a powerful tool to investigate the sensitivity of convective precipitation to changing conditions. In this regard, future work should address the question to which extent enhanced cold pool dynamics and low-level moisture variability contribute to higher precipitation amounts with warming. This could be done in combination with the method of tracing moisture sources. The precipitation signal can then be decomposed into the contributions from thermodynamics, local dynamics and large-scale moisture convergence.

The results of this thesis highlight the importance of small-scale dynamics for the development of intense convective precipitation events and their response to changing conditions. Representing these processes in climate simulations is, thus, crucial to obtain reliable results about future precipitation extremes. However, current global climate models run at much lower resolutions than necessary to resolve convection. Regional convection permitting climate models, on the other hand, are increasingly capable to explicitly resolve turbulence and allow large storms hence the term convection permitting. They have even reached a point that permits the development of large cold pools [Leutwyler et al., 2016]. Given the potential for a high impact of convective rainfall extremes on nature and societies our efforts should thus concentrate on pushing the boundaries of climate modeling to even higher resolutions with the goal to resolve the processes that are key to the dynamics of convective precipitation extremes. While it is clear that such an endeavor requires a large amount of computational power, data infrastructure and expertise, large projects, such as Destination Earth, an initiative of the European Commission, are ideal candidates to achieve this.

BIBLIOGRAPHY

M. R. Allen and W. J. Ingram. Constraints on future changes in climate and the hydrologic cycle. *Nature*, 419(6903):224–232, 2002. doi: 10.1038/nature01092.

J. Attema, J. Loriaux, and G. Lenderink. Extreme precipitation response to climate perturbations in an atmospheric mesoscale model. *Environmental Research Letters*, 9(1): 014003, 2014. doi: 10.1088/1748-9326/9/1/014003.

P. Berg, C. Moseley, and J. O. Haerter. Strong increase in convective precipitation in response to higher temperatures. *Nature Geoscience*, 6(3):181–185, 2013. doi: 10.1038/ngeo1731.

D. Bolton. The computation of equivalent potential temperature. *Monthly Weather Review*, 108(7):1046–1053, 1980. doi: 10.1175/1520-0493(1980)108<1046:tcoept>2.0.co; 2.

S. Bony, R. Colman, V. M. Kattsov, R. P. Allan, C. S. Bretherton, J.-L. Dufresne, A. Hall, S. Hallegatte, M. M. Holland, W. Ingram, D. A. Randall, B. J. Soden, G. Tselioudis, and M. J. Webb. How Well Do We Understand and Evaluate Climate Change Feedback Processes? *Journal of Climate*, 19(15):3445–3482, 2006. doi: 10.1175/jcli3819.1.

S. Brune, S. Buschow, and P. Friederichs. The local wavelet-based organization index – Quantification, localization and classification of convective organization from radar and satellite data. *Quarterly Journal of the Royal Meteorological Society*, 147(736): 1853–1872, 2021. doi: 10.1002/qj.3998.

Buienradar. "Buienradar terugkijken". Online; accessed 21 June, 2021. URL https://www.buienradar.nl/nederland/neerslag/buienradar-terugkijken.

S. J. Böing, H. J. J. Jonker, A. P. Siebesma, and W. W. Grabowski. Influence of the Subcloud Layer on the Development of a Deep Convective Ensemble. *Journal of the Atmospheric Sciences*, 69(9):2682–2698, 2012. doi: 10.1175/jas-d-11-0317.1.

D. Cubasch, U., D. Wuebbles, M. Chen, Facchini, D. Frame, N. Mahowald, and J.-G. Winther. *Climate Change 2013: The Physical Science Basis. Contribution of Working Group I to the Fifth Assessment Report of the Intergovernmental Panel on Climate Change*, chapter 1; Introduction. Cambridge University Press, 2012.

D. P. Dee, S. M. Uppala, A. J. Simmons, P. Berrisford, P. Poli, S. Kobayashi, U. Andrae, M. A. Balmaseda, G. Balsamo, P. Bauer, P. Bechtold, A. C. M. Beljaars, L. van de Berg, J. Bidlot, N. Bormann, C. Delsol, R. Dragani, M. Fuentes, A. J. Geer, L. Haimberger, S. B. Healy, H. Hersbach, E. V. Hólm, L. Isaksen, P. Kållberg, M. Köhler, M. Matricardi, A. P. McNally, B. M. Monge-Sanz, J.-J. Morcrette, B.-K. Park, C. Peubey, P. de Rosnay, C. Tavolato, J.-N.

Thépaut, and F. Vitart. The ERA-Interim reanalysis: configuration and performance of the data assimilation system. *Quarterly Journal of the Royal Meteorological Society*, 137(656):553–597, 2011. doi: 10.1002/qj.828.

J. M. Eden, S. F. Kew, O. Bellprat, G. Lenderink, I. Manola, H. Omrani, and G. J. van Oldenborgh. Extreme precipitation in the Netherlands: An event attribution case study. *Weather and Climate Extremes*, 21:90–101, 2018. doi: 10.1016/j.wace.2018.07.003.

J. Fan, B. Han, A. Varble, H. Morrison, K. North, P. Kollias, B. Chen, X. Dong, S. E. Giangrande, A. Khain, Y. Lin, E. Mansell, J. A. Milbrandt, R. Stenz, G. Thompson, and Y. Wang. Cloud-resolving model intercomparison of an MC3E squall line case: Part I—Convective updrafts. *Journal of Geophysical Research: Atmospheres*, 122(17):9351–9378, 2017. doi: 10.1002/2017jd026622.

Z. Feng, X. Dong, B. Xi, S. A. McFarlane, A. Kennedy, B. Lin, and P. Minnis. Life cycle of midlatitude deep convective systems in a Lagrangian framework. *Journal of Geophysical Research: Atmospheres*, 117(D23), 2012. doi: 10.1029/2012jd018362.

B. Fildier, H. Parishani, and W. D. Collins. Simultaneous characterization of mesoscale and convective-scale tropical rainfall extremes and their dynamical and thermodynamic modes of change. *Journal of Advances in Modeling Earth Systems*, 9(5):2103–2119, 2017. doi: 10.1002/2017ms001033.

E. M. Fischer and R. Knutti. Observed heavy precipitation increase confirms theory and early models. *Nature Climate Change*, 6(11):986–991, 2016. doi: 10.1038/nclimate3110.

H. F. Fuglestvedt and J. O. Haerter. Cold Pools as Conveyor Belts of Moisture. *Geophysical Research Letters*, 47(12):e2020GL087319, 2020. doi: 10.1029/2020gl087319.

W. W. Grabowski. Toward Cloud Resolving Modeling of Large-Scale Tropical Circulations: A Simple Cloud Microphysics Parameterization. *Journal of the Atmospheric Sciences*, 55(21):3283–3298, 1998. doi: 10.1175/1520-0469(1998)055<3283:tcrmol>2.0.co;2.

K. Guinard, A. Mailhot, and D. Caya. Projected changes in characteristics of precipitation spatial structures over North America. *International Journal of Climatology*, 35(4):596–612, 2014. doi: 10.1002/joc.4006.

J. O. Haerter and P. Berg. Unexpected rise in extreme precipitation caused by a shift in rain type? *Nature Geoscience*, 2(6):372–373, 2009. doi: 10.1038/ngeo523.

J. O. Haerter and L. Schlemmer. Intensified Cold Pool Dynamics Under Stronger Surface Heating. *Geophysical Research Letters*, 45(12):6299–6310, 2018. doi: 10.1029/2017gl076874.

J. O. Haerter, P. Berg, and C. Moseley. Precipitation onset as the temporal reference in convective self-organization. *Geophysical Research Letters*, 44(12):6450–6459, 2017. doi: 10.1002/2017gl073342.

J. O. Haerter, S. J. Böing, O. Henneberg, and S. B. Nissen. Circling in on Convective Organization. *Geophysical Research Letters*, 46(12):7024–7034, 2019. doi: 10.1029/2019gl082092.

D. Hartmann, A. K. Tank, M. Rusticucci, L. Alexander, S. Brönnimann, Y. Charabi, F. Dentener, E. Dlugokencky, D. Easterling, A. Kaplan, B. Soden, P. Thorne, M. Wild, and P. Zhai. *Climate Change 2013: The Physical Science Basis. Contribution of Working Group I to the Fifth AssessmentReport of the Intergovernmental Panel on Climate Change*, chapter 2; Observations: Atmosphere and Surface. Cambridge University Press, 2013.

T. Heus, C. C. van Heerwaarden, H. J. J. Jonker, A. P. Siebesma, S. Axelsen, K. van den Dries, O. Geoffroy, A. F. Moene, D. Pino, S. R. de Roode, and J. V.-G. de Arellano. Formulation of the Dutch Atmospheric Large-Eddy Simulation (DALES) and overview of its applications. *Geoscientific Model Development*, 3(2):415–444, 2010. doi: 10.5194/gmd-3-415-2010.

M. Hirt, G. C. Craig, S. A. K. Schäfer, J. Savre, and R. Heinze. Cold-pool-driven convective initiation: using causal graph analysis to determine what convection-permitting models are missing. *Quarterly Journal of the Royal Meteorological Society*, 146(730):2205–2227, 2020. doi: 10.1002/qj.3788.

P. Hoeppe. Trends in weather related disasters – Consequences for insurers and society. *Weather and Climate Extremes*, 11:70–79, 2016. doi: 10.1016/j.wace.2015.10.002.

M. Khairoutdinov and D. Randall. High-Resolution Simulation of Shallow-to-Deep Convection Transition over Land. *Journal of the Atmospheric Sciences*, 63(12):3421–3436, 2006. doi: 10.1175/jas3810.1.

V. V. Kharin, F. W. Zwiers, X. Zhang, and M. Wehner. Changes in temperature and precipitation extremes in the CMIP5 ensemble. *Climatic Change*, 119(2):345–357, 2013. doi: 10.1007/s10584-013-0705-8.

KNMI Data Platform. "Precipitation - duration, amount and intensity at a 10 minute interval", 2021. URL https://dataplatform.knmi.nl/dataset/neerslaggegevens-1-0.

W. Langhans, K. Yeo, and D. M. Romps. Lagrangian Investigation of the Precipitation Efficiency of Convective Clouds. *Journal of the Atmospheric Sciences*, 72(3):1045–1062, 2015. doi: 10.1175/jas-d-14-0159.1.

H. Le Treut, R. Somerville, U. Cubasch, Y. Ding, C. Mauritzen, A. Mokssit, T. Peterson, and M. Prather. *Climate Change 2007: The Physical Science Basis. Contribution of Working Group I to the Fourth Assessment Reportof the Intergovernmental Panel on Climate Change*, chapter 1; Historical Overview of Climate Change Science. Cambridge University Press, 2007.

M. Leal, C. Ramos, and S. Pereira. Different types of flooding lead to different human and material damages: the case of the Lisbon Metropolitan Area. *Natural Hazards*, 91(2):735–758, 2018. doi: 10.1007/s11069-017-3153-3.

M. Leal, I. Boavida-Portugal, M. Fragoso, and C. Ramos. How much does an extreme rainfall event cost? Material damage and relationships between insurance, rainfall, land cover and urban flooding. *Hydrological Sciences Journal*, 64(6):673–689, 2019. doi: 10.1080/02626667.2019.1595625.

G. Lenderink and E. van Meijgaard. Increase in hourly precipitation extremes beyond expectations from temperature changes. *Nature Geoscience*, 1(8):511–514, 2008. doi: 10.1038/ngeo262.

G. Lenderink and E. van Meijgaard. Linking increases in hourly precipitation extremes to atmospheric temperature and moisture changes. *Environmental Research Letters*, 5(2):025208, 2010. doi: 10.1088/1748-9326/5/2/025208.

G. Lenderink, H. Y. Mok, T. C. Lee, and G. J. van Oldenborgh. Scaling and trends of hourly precipitation extremes in two different climate zones – Hong Kong and the Netherlands. *Hydrology and Earth System Sciences*, 15(9):3033–3041, 2011. doi: 10.5194/hessd-8-4701-2011.

G. Lenderink, R. Barbero, J. M. Loriaux, and H. J. Fowler. Super-Clausius–Clapeyron Scaling of Extreme Hourly Convective Precipitation and Its Relation to Large-Scale Atmospheric Conditions. *Journal of Climate*, 30(15):6037–6052, 2017. doi: 10.1175/jcli-d-16-0808.1.

G. Lenderink, R. Barbero, S. Westra, and H. J. Fowler. Reply to comments on "Temperature-extreme precipitation scaling: a two-way causality?". *International Journal of Climatology*, 38(12):4664–4666, 2018. doi: 10.1002/joc.5799.

D. Leutwyler, O. Fuhrer, X. Lapillonne, D. Lüthi, and C. Schär. Towards European-scale convection-resolving climate simulations with GPUs: a study with COSMO 4.19. *Geoscientific Model Development*, 9(9):3393–3412, 2016. doi: 10.5194/gmd-9-3393-2016.

J. Li, C. Wasko, F. Johnson, J. P. Evans, and A. Sharma. Can regional climate modeling capture the observed changes in spatial organization of extreme storms at higher temperatures? *Geophysical Research Letters*, 45(9):4475–4484, 2018. doi: 10.1029/2018gl077716.

Z. Li and P. A. O'Gorman. Response of Vertical Velocities in Extratropical Precipitation Extremes to Climate Change. *Journal of Climate*, 33(16):7125–7139, 2020. doi: 10.1175/jcli-d-19-0766.1.

K. Lochbihler, G. Lenderink, and A. P. Siebesma. The spatial extent of rainfall events and its relation to precipitation scaling. *Geophysical Research Letters*, 44(16):8629–8636, 2017. doi: 10.1002/2017gl074857.

K. Lochbihler, G. Lenderink, and A. P. Siebesma. Response of Extreme Precipitating Cell Structures to Atmospheric Warming. *Journal of Geophysical Research: Atmospheres*, 124(13):6904–6918, 2019. doi: 10.1029/2018jd029954.

J. M. Loriaux, G. Lenderink, S. R. D. Roode, and A. P. Siebesma. Understanding Convective Extreme Precipitation Scaling Using Observations and an Entraining Plume Model. *Journal of the Atmospheric Sciences*, 70(11):3641–3655, 2013. doi: 10.1175/jas-d-12-0317.1.

J. M. Loriaux, G. Lenderink, and A. P. Siebesma. Large-Scale Controls on Extreme Precipitation. *Journal of Climate*, 30(3):955–968, 2017. doi: 10.1175/jcli-d-16-0381.1.

N. J. Lutsko and T. W. Cronin. Increase in Precipitation Efficiency With Surface Warming in Radiative-Convective Equilibrium. *Journal of Advances in Modeling Earth Systems*, 10(11):2992–3010, 2018. doi: 10.1029/2018ms001482.

E. v. Meijgaard, L. H. v. Ulft, G. Lenderink, S. R. d. Roode, E. L. Wipfler, R. Boers, and R. M. A. v. Timmermans. Refinement and application of a regional atmospheric model for climate scenario calculations of Western Europe. Technical report, Royal Netherlands Meteorological Institute, Wageningen, 2012. URL http://edepot.wur.nl/312258.

V. Mishra, J. M. Wallace, and D. P. Lettenmaier. Relationship between hourly extreme precipitation and local air temperature in the United States. *Geophysical Research Letters*, 39(16), 2012. doi: 10.1029/2012gl052790.

P. Molnar, S. Fatichi, L. Gaál, J. Szolgay, and P. Burlando. Storm type effects on super Clausius–Clapeyron scaling of intense rainstorm properties with air temperature. *Hydrology and Earth System Sciences*, 19(4):1753–1766, 2015. doi: 10.5194/hess-19-1753-2015.

C. Moseley, P. Berg, and J. O. Haerter. Probing the precipitation life cycle by iterative rain cell tracking. *Journal of Geophysical Research: Atmospheres*, 118(24):13,361–13,370, 2013. doi: 10.1002/2013jd020868.

C. Moseley, C. Hohenegger, P. Berg, and J. O. Haerter. Intensification of convective extremes driven by cloud–cloud interaction. *Nature Geosci.*, 9(10):748–752, 2016. doi: 10.1038/ngeo2789.

C. Muller and Y. Takayabu. Response of precipitation extremes to warming: what have we learned from theory and idealized cloud-resolving simulations, and what remains to be learned? *Environmental Research Letters*, 15(3):035001, 2020. doi: 10.1088/1748-9326/ab7130.

C. J. Muller, P. A. O'Gorman, and L. E. Back. Intensification of Precipitation Extremes with Warming in a Cloud-Resolving Model. *Journal of Climate*, 24(11):2784–2800, 2011. doi: 10.1175/2011jcli3876.1.

J. D. Neelin, O. Peters, and K. Hales. The Transition to Strong Convection. *Journal of the Atmospheric Sciences*, 66(8):2367–2384, 2009. doi: 10.1175/2009jas2962.1.

J. Nie, A. H. Sobel, D. A. Shaevitz, and S. Wang. Dynamic amplification of extreme precipitation sensitivity. *Proceedings of the National Academy of Sciences*, 115(38):9467–9472, 2018. doi: 10.1073/pnas.1800357115.

P. A. O'Gorman and C. J. Muller. How closely do changes in surface and column water vapor follow Clausius–Clapeyron scaling in climate change simulations? *Environmental Research Letters*, 5(2):025207, 2010. doi: 10.1088/1748-9326/5/2/025207.

A. M. Oppenheimer, C. Diop, J. Hess, R. Lempert, J. Li, R. Muir-Wood, and S. Myeong. *Managing the Risks of Extreme Events and Disasters to Advance Climate Change Adaptation*, chapter 1; Climate change: new dimensions in disaster risk, exposure, vulnerability, and resilience. Cambridge University Press, 2012.

A. Overeem, T. A. Buishand, and I. Holleman. Extreme rainfall analysis and estimation of depth-duration-frequency curves using weather radar. *Water Resources Research*, 45 (10), 2009a. doi: 10.1029/2009wr007869.

A. Overeem, I. Holleman, and A. Buishand. Derivation of a 10-Year Radar-Based Climatology of Rainfall. *Journal of Applied Meteorology and Climatology*, 48(7):1448–1463, 2009b. doi: 10.1175/2009jamc1954.1.

P. Pall, M. R. Allen, and D. A. Stone. Testing the Clausius–Clapeyron constraint on changes in extreme precipitation under CO2 warming. *Climate Dynamics*, 28(4):351–363, 2007. doi: 10.1007/s00382-006-0180-2.

N. Peleg, F. Marra, S. Fatichi, P. Molnar, E. Morin, A. Sharma, and P. Burlando. Intensification of Convective Rain Cells at Warmer Temperatures Observed from High-Resolution Weather Radar Data. *Journal of Hydrometeorology*, 19(4):715–726, 2018. doi: 10.1175/jhm-d-17-0158.1.

A. G. Pendergrass, K. A. Reed, and B. Medeiros. The link between extreme precipitation and convective organization in a warming climate: Global radiative-convective equilibrium simulations. *Geophysical Research Letters*, 43(21):11,445–11,452, 2016. doi: 10.1002/2016gl071285.

S. Pfahl, P. A. O'Gorman, and E. M. Fischer. Understanding the regional pattern of projected future changes in extreme precipitation. *Nature Climate Change*, 7(6):423–427, 2017. doi: 10.1038/nclimate3287.

A. F. Prein, C. Liu, K. Ikeda, S. B. Trier, R. M. Rasmussen, G. J. Holland, and M. P. Clark. Increased rainfall volume from future convective storms in the US. *Nature Climate Change*, 7(12):880–884, 2017. doi: 10.1038/s41558-017-0007-7.

D. M. Romps. Response of Tropical Precipitation to Global Warming. *Journal of the Atmospheric Sciences*, 68(1):123–138, 2011. doi: 10.1175/2010jas3542.1.

L. Schlemmer and C. Hohenegger. The Formation of Wider and Deeper Clouds as a Result of Cold-Pool Dynamics. *Journal of the Atmospheric Sciences*, 71(8):2842–2858, 2014. doi: 10.1175/jas-d-13-0170.1.

L. Schlemmer and C. Hohenegger. Modifications of the atmospheric moisture field as a result of cold-pool dynamics. *Quarterly Journal of the Royal Meteorological Society*, 142(694):30–42, 2016. doi: 10.1002/qj.2625.

C. Schär, N. Ban, E. M. Fischer, J. Rajczak, J. Schmidli, C. Frei, F. Giorgi, T. R. Karl, E. J. Kendon, A. M. G. K. Tank, P. A. O'Gorman, J. Sillmann, X. Zhang, and F. W. Zwiers. Percentile indices for assessing changes in heavy precipitation events. *Climatic Change*, 137(1):201–216, 2016. doi: 10.1007/s10584-016-1669-2.

A. Seifert and T. Heus. Large-eddy simulation of organized precipitating trade wind cumulus clouds. *Atmospheric Chemistry and Physics*, 13(11):5631–5645, 2013. doi: 10.5194/acp-13-5631-2013.

M. S. Singh and P. A. O'Gorman. Influence of microphysics on the scaling of precipitation extremes with temperature. *Geophysical Research Letters*, 41(16):6037–6044, 2014. doi: 10.1002/2014gl061222.

A. Singleton and R. Toumi. Super-Clausius-Clapeyron scaling of rainfall in a model squall line. *Quarterly Journal of the Royal Meteorological Society*, 139(671):334–339, 2013. doi: 10.1002/qj.1919.

C. Tebaldi, K. Hayhoe, J. M. Arblaster, and G. A. Meehl. Going to the Extremes. *Climatic Change*, 79(3):185–211, 2006. doi: 10.1007/s10584-006-9051-4.

S. F. B. Tett, J. F. B. Mitchell, D. E. Parker, and M. R. Allen. Human Influence on the Atmospheric Vertical Temperature Structure: Detection and Observations. *Science*, 274 (5290):1170–1173, 1996. doi: 10.1126/science.274.5290.1170.

A. M. Tompkins. Organization of Tropical Convection in Low Vertical Wind Shears: The Role of Cold Pools. *Journal of the Atmospheric Sciences*, 58(13):1650–1672, 2001. doi: 10.1175/1520-0469(2001)058<1650:ootcil>2.0.co;2.

G. Torri, Z. Kuang, and Y. Tian. Mechanisms for convection triggering by cold pools. *Geophysical Research Letters*, 42(6):1943–1950, 2015. doi: 10.1002/2015gl063227.

K. E. Trenberth, A. Dai, R. M. Rasmussen, and D. B. Parsons. The Changing Character of Precipitation. *Bulletin of the American Meteorological Society*, 84(9):1205–1218, 2003. doi: 10.1175/bams-84-9-1205.

C. Wasko and A. Sharma. Steeper temporal distribution of rain intensity at higher temperatures within Australian storms. *Nature Geoscience*, 8(7):527–529, 2015. doi: 10.1038/ngeo2456.

C. Wasko, A. Sharma, and F. Johnson. Does storm duration modulate the extreme precipitation-temperature scaling relationship? *Geophysical Research Letters*, 42(20): 8783–8790, 2015. doi: 10.1002/2015gl066274.

C. Wasko, A. Sharma, and S. Westra. Reduced spatial extent of extreme storms at higher temperatures. *Geophysical Research Letters*, 43(8):4026–4032, 2016. doi: 10.1002/ 2016gl068509.

C. Wasko, W. T. Lu, and R. Mehrotra. Relationship of extreme precipitation, dry-bulb temperature, and dew point temperature across Australia. *Environmental Research Letters*, 13(7):074031, 2018. doi: 10.1088/1748-9326/aad135.

S. Westra, H. J. Fowler, J. P. Evans, L. V. Alexander, P. Berg, F. Johnson, E. J. Kendon, G. Lenderink, and N. M. Roberts. Future changes to the intensity and frequency of short-duration extreme rainfall. *Reviews of Geophysics*, 52(3):522–555, 2014. doi: 10.1002/2014rg000464.

ABOUT THE AUTHOR

August 6, 1986	Born in Kempten im Allgäu, Germany
1997–2007	Grammar School Gymnasium Immenstadt im Allgäu, Germany
2007–2008	Alternative service Association for nature conservation of Bavaria
2008–2012	Bachelor degree in Geography University of Augsburg, Germany
2012–2015	Master degree in Climate and Environment Sciences University of Augsburg, Germany
2016–2021	PhD postion as part of the project "Space2rain", Royal Netherlands Meteorological Institute (KNMI) and Delft University of Technology

LIST OF PUBLICATIONS

- Lochbihler, K., Lenderink, G., and Siebesma, A. P., *The spatial extent of rainfall events and its relation to precipitation scaling*, 2017, Geophys. Res. Lett., doi:10.1002/2017GL074857

- Lochbihler, K., Lenderink, G., and Siebesma, A. P., *Response of extreme precipitating cell structures to atmospheric warming*, 2019, Journal of Geophysical Research: Atmospheres, doi:10.1029/2018JD029954

- Lochbihler, K., Lenderink, G., and Siebesma, A. P., *Cold pool dynamics shape the response of extreme rainfall events to climate change*, 2021, Journal of Advances in Modeling Earth Systems, doi:10.1029/2020MS002306

ACKNOWLEDGEMENTS

Here, I want to thank all the people that made this dissertation possible and stood by me on this journey. First and foremost there are my two promotors, Pier Siebesma and Geert Lenderink. Geert, I can not emphasize enough how much you made me feel welcome in my new job at KNMI. I learned so much about being a researcher from you. Over the years, your office door was always open for me no matter if I came for a spontaneous discussion about work or just a chat. The same goes for you, Pier. Your way of never losing sight of the long-term perspective and the continuous promotion of my work taught me important lessons and lead me to interesting conferences. Both of you established contacts and opportunities, such as my short sabbatical in Copenhagen. You were always open to my ideas, encouraged me, and helped me in developing my own research line. I remember the many meetings that I left with the feeling of refreshed motivation and this spark of discovering something new. I think that every future PhD student of yours can be happy to have you as supervisors.

I also want to thank all other former and current members of the department Weather and Climate Models at KNMI. I felt very welcome in this familial environment with all the nice and friendly people. I really enjoyed working there. And, thank you for all the lunches, the chats in the coffee corner, and the occasional heated discussions with drinks after the monthly colloquium. Finally, I want to thank Jessica Loriaux in particular who provided a solid basis for my work and gave me an excellent kick start into my own PhD journey.

For my time at the Niels Bohr Institute in Copenhagen, I want to thank Jan Haerter and his team for all the inspiring discussions and hospitality. It was a pleasure.

Then there is the "Augschburger Fraktion". Euch aus Augsburg, meine lieben Freunde, möchte ich an dieser Stelle auch ganz herzlich danken. Für all die Besuche hier in Utrecht, dass ich in Augsburg immer eine Bleibe hatte, und, dass der Kontakt und die Freundschaft über die Zeit und Distanz Bestand hatte. Gerade auch zuletzt, während des Coronalockdowns haben all die virtuellen Spieleabende enorm geholfen. Danke, Flo, Julia, Cornelius, Lisa, Chris, Alex, Leonie, etc. Bei Chris möchte ich mich zusätzlich auch für das Korrekturlesen bedanken.

The list of close friends would not be complete without the following three people: Vinzenz, Dario and Patricio. Vinzenz and Dario, our long-lasting friendships were and are an enormous support, not only during my PhD time. Thank you Patricio for all the jam sessions and good conversations.

I thank all my family members who continuously supported me in all thinkable ways. Allen voran möchte ich meinen Eltern danken, für alles. Ihr standet immer hinter mir und ich konnte mich immer auf euch verlassen. Ich möchte auch meiner Schwester samt Ehemann dafür danken. Im Besonderen geht mein Dank auch an meinen Bruder mit Familie, nicht zuletzt auch wegen unserer Gespräche im Lockdown.

My final words of thanks go to Maria del mar. In all those years you were by my side with an enormous amount of support, encouragement and endurance. Especially the last phase of my PhD journey, I don't know how it would have been possible without you. Thank you.